UNIVERSITAT POLITÈCNICA DE CATALUNYA BARCELONATECH

Hydrodynamics and geochemistry at multiple scales: characterizing preferential flow-paths and wormholes in evaporitic sediments

Michela Trabucchi

UNIVERSITAT POLITÈCNICA DE CATALUNYA

DOCTORAL THESIS

Hydrodynamics and Geochemistry at Multiple Scales: Characterizing Preferential Flow-Paths and Wormholes in Evaporitic Sediments

Author:
Michela TRABUCCHI

Supervisors:
Prof. Daniel FERNÀNDEZ GARCIA
Prof. Jesús CARRERA

A thesis submitted in fulfillment of the requirements
for the degree of Doctor of Philosophy
in the
Department of Civil and Environmental Engineering

April, 2021

This thesis has been founded by the AGAUR (Agància de Gestió d'Ajuts Universitaris i de Recerca, Generalitat de Catalunya) through the FI fellowship 2016FI-B-00840 and by the Sociedad Química y Minera de Chile (SQM) S.A. through the project "Proyección de la evolución SOP – Salar de Atacama. Fase II: ensayos de campo y laboratorio" (SA 9500001785).

Michela Trabucchi

Hydrodynamics and Geochemistry at Multiple Scales: Characterizing Preferential Flow-Paths and Wormholes in Evaporitic Sediments

Ph.D Thesis, April, 2021
External reviewers: Daniele Pedretti and Linda Luquot
Supervisors: Daniel Fernàndez Garcia and Jesús Carrera

Universitat Politècnica de Catalunya
Groundwater Hydrology Group (UPC-CSIC)
Department of Civil and Environmental Engineering
Carrer Jordi Girona 1-3, D-2, 004
08034 Barcelona, Spain

Cover Illustration

"*It is not what you look at that matters, it is what you see.*"
Front cover: Flowers or Wormholes? Picture of the dissolution structure characterized by dominant wormholes, Chapter 5.
Back cover: Mountains or Halite? X-ray micro-tomography of a halite rock sample, 3D view.

Acknowledgements

The only rule of a journey is not to conclude it as you left. Come back different. And above all, the change is triggered by the people you meet on your journey, those who enjoy you for short or long distances, and those who were there since before, animating you to embark on a new journey and supporting you from afar. All these people deserve a big thank.

First of all, I would like to express my deep gratitude to my supervisors, Daniel Fernàndez Garcia and Jesús Carrera, a "great team". You welcomed me into this great scientific family and accompanied me, through thick and thin, up to the end of this journey. I would like to thank Dani for guiding and supporting me all these years, dispensing not only large doses of knowledge, but also advice and reassurances in moments of hesitation. And between advice and advice, you crushed me (us) at ping pong and paddle. I thank you for that as well. But get ready, I'll be back for the rematch. I would like to thank Jesús for sharing its enormous knowledge and for the several constructive discussions. Thanks as well for sharing pearls of wisdom that now I have learned, there is no way to respect!

During this journey I have had the pleasure of collaborating with great people outside the research group as well. A sincere thanks goes to the SQM team for the collaborative work done from afar. Special thanks go to Corrado Tore, Alvaro Henríquez, Julio Vallejos, Berta Morales, Beatriz Sierra and Andres Fock. The many meetings and exchanges of views that we have taken have certainly enriched this journey both on a personal and scientific way. I would also like to thank Carlota Viñas, Francesco Riva and Meritxell Tañà who have helped me to tackle different stages of the journey. Each of you has taught me something.

Obviously the journey would not have been the same without the support of the "gang of people" who, like me, at a given moment of their life decided to undertake this path. A big thank goes to Uri, Joui, Carme, Nuri,

Albert, Gumbi, Dani, Mireia, Yufi, Alec, Lazaro, Guilli, Arni, Bieito, Folch and Paula. With you I have shared infinite (and indispensable) breakfasts, excessive doses of caffeine, few(?) doses of alcohol and many, many chat. All this seasoned with struggles at sea (paddle-surf), ping-pong disputes and padel matches (the bet is still to be paid!). With no doubt, all this enriched the trip and made it memorable. Even though the journey is about to end, I hope to meet you all on the next one, as old friends. Another big thank goes to Vera, Malek, Rodrigo, Guillem and Guido that have definitely cheered the last year. Even though these crazy times didn't allow us to share many things, we have a long to-do list that is waiting for better times.

Un inmenso gracias va a la Rubia, Val, León, Nuria, Nabil, Raúl, Ingrid, Victor (y Kiwi), Lara e Ibai, un gran equipo (o mejor dicho, familia) con el que viajar, un poco loco (¿quién no lo es?) y nada convencional! Gracias por la despreocupación y la alegría que siempre lográis transmitir cuando estamos junt@s. Y gracias por las sesiones de "terápia", las de silencio, así como las de juego, las de padel, las escursiones y el baile! En este ultimo, sigo pensando que tenemos un futuro!

Grazie ai Cianfer (Cianferoni e cianferini), alla Ila, la Ceci, la Jenny, Gaia, la Zuffa, Fra, la Moka, Jessy. Siete un po' sparpagliati in giro per l'Italia: sui monti, in cittá, tra i campi di ggiú. Due messaggi ogni tanto, una chiamata inattesa, diecimila intenti per sentirci (e vederci). Ecco, a voi un grazie speciale, perché anche se con la comunicazione vado un po' a scoppio, vi sento sempre vicini.

E poi ci siete voi, la mia famiglia. Un grazie immenso va a mia mamma, che riesce sempre a fare in modo che non mi senta mai troppo lontana da casa, anche se i kilometri sono tanti. Grazie a Liuk, Megghi, Dani e Franci, bastano poche parole ogni tanto, un'escursione qua e la, per sentirsi vicini e continuare a crescere insieme. Grazie in particolare ai miei fratelli, che non perdono occasione per prendermi in giro nonostante la lontananza, e cosí si che uno si sente a casa davvero!
Sapere che voi e la mamma ci siete, sempre e comunque, mi ha dato serenitá

e forza per affrontare questo dottorato, fare scelte importanti e sapere che al tornare a casa troveró sempre tante porte aperte (e il frigorifero pieno!).

Y por ultimo, no creo que hayan suficientes palabras para dar las gracias a Bruno. Entraste en mi vida poco a poco, al principio de este viaje. Me enseñaste a relativizar los problemas, a mirarlos desde otro punto de vista. Me ayudaste a creer más en mi misma y a la vez, a ser más empatica con los demás. Me ayudaste a entender la importancia de la actitud, y que un lapiz entre los dientes siempre ayuda! Me enseñaste a disfrutar mucho más del dia a dia, y como consecuencia, a disfrutar mucho más también de este viaje que estoy a punto de acabar. Has sido el mejor compañero que podía esperar. Contigo la mochila pesa muy poco y la risa es asegurada, así que seguimos!

P.s. Even today I ask myself how I managed to begin the PhD journey expressing my intentions by e-mail...luck clearly matters!

P.s. I would like to mention the neighbours of Hostafrancs. Despite having tried several times, I have not managed to get anyone steal my motorbike. Thank you all, I really appreciate it. You are somehow the evidence that there are much more good people than bad ones around. If this is not the case, luck clearly matters, again.

L = (K + S) A

Life, **K**nowledge, **S**kills, **A**ttitude

Victor Küppers

To my family,
an inexhaustible source of resilience

Abstract

The characterization of evaporitic aquifers for a better understanding of hydrodynamics and geochemical processes is of great importance, especially in environments where both the sustainability of unique ecosystems and the economic interests depend on aquifer features. This is the case of the Salar de Atacama (SdA) evaporitic nucleus, the "driving force" of this thesis, which prompt us to pursue two main objectives. First, characterizing the hydraulic behavior of the SdA nucleus, with special attention for the identification of highly connected structures (preferential flow-paths). Second, enriching the knowledge on preferential flow-paths development caused by dissolution processes (i.e. wormholes dynamics) and the corresponding changes in flow and transport behaviour.

For aquifer characterization, pumping tests are usually performed to gain conceptual understanding about the system through diagnostic plots and to estimate hydraulic properties. Among them, recovery tests consist of measuring head response in observation and/or pumping wells after pumping termination. They are especially useful when the pumping rate cannot be accurately controlled. Agarwal proposed a method, which has become standard in the oil industry, to obtain both early and late time reservoir responses to pumping from recovery data. However, the validity of the method has only been tested to a limited extent. In the second chapter of this thesis we analyze Agarwal's method to understand its limitations and to overcome them. Our results show that Agarwal's method provides excellent recovery plots (i.e., the drawdown curve that would be obtained during pumping) and parameter estimates for nearly all aquifer conditions, provided that a constant pumping rate is used and the log-derivative at the end of pumping is constant, which is too limiting for groundwater hydrology practice, where observation wells are usually monitored. Thus, we generalize Agarwal's method by (1) deriving an improved equivalent time for time-dependent pumping rate, and (2) proposing to recover drawdown curves by extrapolating the pumping phase

drawdowns. These yield excellent diagnostic plots, thus facilitating the conceptual model analysis, for a broad range of conditions.
However, hydraulic test interpretation based on drawdown curve data analysis is difficult to carry out when dealing with large aquifer systems with complex flow dynamics driven for instance by large pumping fields. In this case, the characterization is usually achieved through groundwater modeling. Thus, from hydraulic testing we keep the concept that the drawdown response to a hydraulic stress contains crucial information to characterize an aquifer, and we project it in groundwater modeling. Modeling drawdowns would be far easier than modeling heads because they are subject to homogeneous (zero) internal sink/sources, and boundary and initial conditions. The problem lies on the fact that drawdowns are not measured directly, but derived from measurements of head fluctuations. Resulting drawdowns may suffer persistent inaccuracies in complex systems with uncertain long-acting external stresses, so that they are affected not only by errors in head measurements, but also in estimates of the natural head evolution (i.e., heads that would have occurred if the test had not been performed). This hinders the use of drawdowns in groundwater models, and forces modellers to employ absolute heads and soft information. In this context, in the third chapter we present a method to filter systematic errors in drawdown data during the automatic calibration of a groundwater model. To do this, we introduce a bias correction term in a composite inverse problem that combines a natural head model with a drawdown model. Since these two models share the same parameters, a two-stage iterative optimization algorithm is developed to jointly estimate the bias, natural trends and parameters. The method is illustrated by a synthetic example in a heterogeneous aquifer. The example shows that the method converges to the best conditional estimate even when absolute head data is strongly biased. In the same example, we demonstrate that the use of biased absolute head data in the traditional inverse problem can also provide good fittings but, in this case, the bias leads to an incorrect estimation of the transmissivity field.
In the fourth chapter, we apply the filtering-corrective method, coupled with

the stochastic inversion, to the SdA nucleus to characterize the spatial distribution of the hydraulic conductivity at a large scale, with special attention to the identification of connectivity structures (highly conductive channels) that control groundwater flow and contaminant transport. In evaporitic aquifer systems, these preferential channels can consist of karst conduits, developed at different scales, as well as fault zones. In this context, we investigate if it is possible to use (tomographic) stochastic inversion (regularized pilot point method) in order to characterize the presence of connectivity structures in the SdA evaporitic aquifer (great extension, about 1500 km^2) from head response measured at numerous observation points during a year long sequence of three hydraulic tests. Results show that, even though the solution is non unique, the main preferential flow zones are identified. Numerous inversions yield similar fits to observed drawdowns with maximum errors of few centimeters. Preferential flow is identified not only by elongated high permeability regions, but also by a marked scale effect (model transmissivities are some 30 times larger than their local tests counterparts). The main high conductivity zones are consistent with independent information based on geophysics, isotopes, mixing ratios, piezometric data, and the expected dissolution processes.

Finally, in order to better understand the dynamics involved in the development of these preferential flow-paths and their effects on flow and transport behavior, we carry out a laboratory dissolution experiment under controlled conditions. We move to an intermediate-scale analysis since organized connectivity structures (wormholes) may develop at different spatial and temporal scales. We know from previous studies the optimal conditions under which these structures may form, but their spatio-temporal evolution, as well as the redistribution of the flow among wormholes and changes in transport processes are largely unknown. Thus, we perform a dissolution experiment in a synthetic evaporitic aquifer, jointly with several tracer tests, to study the evolution of a dissolution pattern characterized by dominant wormholes. We

analyze the evolution of wormhole dynamics, with special attention to wormholes growth, changes in hydraulic properties, wormhole geometry, and competition for the flow. We observe the redistribution of the flow with the development of the wormholes, as well as some evidence of the triggering and amplifying factors that are involved in the self-organization mechanism that lead to dissolution structures. Furthermore, by interpreting the tracer test breakthrough curves we are able to quantify the effect that these structures have on the hydraulic and transport behavior. For that, we apply the multi-advection dispersion model, considering two modelling approaches: by fitting the measured breakthrough curves with effective transport parameters and by predicting the breakthrough curve evolution through a discrete wormhole modeling approach, applied knowing the geometry of the system and transport parameters of the undissolved matrix. Both approaches are capable of reproducing the experimental data, highlighting the ability to characterize the system. Results also demonstrate the high predictive power of the discrete wormhole model.

Riassunto

La caratterizzazione degli acquiferi evaporitici, atta a comprendere meglio i processi idrodinamici e geochimici, è di grande importanza, soprattutto in ambienti in cui sia la sostenibilità di ecosistemi unici sia gli interessi economici dipendono dalle caratteristiche dell'acquifero. È il caso del nucleo evaporitico del Salar de Atacama (SdA), il "motore" di questa tesi, che ci spinge a perseguire due obiettivi principali. In primo luogo, caratterizzare il comportamento idraulico del nucleo del SdA, con particolare attenzione all'identificazione di strutture altamente connesse (percorsi di flusso preferenziali). In secondo luogo, arricchire la conoscenza sullo sviluppo di zone di flusso preferenziale dovuto ai processi di dissoluzione (in altre parole, le dinamiche dei *wormholes*) e sui relativi cambiamenti nel comportamento di flusso e trasporto.
Per caratterizzare una falda acquifera solitamente vengono eseguite prove di pompaggio, con lo scopo di comprendere il modello concettuale del sistema, attraverso grafici diagnostici, e stimarne le proprietà idrauliche. Tra le varie prove, le prove di recupero consistono nel misurare le variazioni del livello piezometrico nei pozzi di pompaggio e/o monitoraggio una volta completata la prova di pompaggio. Questi test sono particolarmente utili quando la portata non può essere controllata con precisione. Agarwal ha proposto un metodo, diventato standard nell'industria petrolifera, per ottenere la risposta dell'acquifero al pompaggio a partire dai dati di recupero. Tuttavia, il metodo è stato testato e verificato in misura limitata. Nel secondo capitolo di questa tesi analizziamo il metodo di Agarwal per comprenderne i limiti e superarli. I risultati ottenuti mostrano che il metodo di Agarwal fornisce eccellenti grafici di recupero (ovvero la curva di abbassamento che si otterrebbe durante il pompaggio) e buone stime dei parametri idraulici per quasi tutte le condizioni dell'acquifero, a condizione che venga utilizzata una portata costante e che la derivata logaritmica alla fine del periodo di pompaggio sia costante. Queste condizioni sono troppo limitanti per l'applicazione nell'idrologia delle acque

sotterranee, dove spesso vengono monitorati i pozzi di osservazione. Si generalizza quindi il metodo di Agarwal (1) derivando un tempo equivalente per portate che variano nel tempo e (2) proponendo di ottenere le curve di abbassamento dal recupero, estrapolando l'abbassamento della fase di pompaggio. In questo modo si ottengono ottimi grafici diagnostici che facilitano l'analisi del modello concettuale e consentono di applicare il metodo per un'ampia gamma di condizioni.
Tuttavia, è difficile eseguire l'interpretazione dei test idraulici, basata sull'analisi dei dati di abbassamento, per caratterizzare grandi sistemi acquiferi con dinamiche di flusso complesse (ad esempio, nel caso in cui siano presenti grandi campi di pozzi in pompaggio). In questo caso, la caratterizzazione viene generalmente ottenuta attraverso la modellazione delle acque sotterranee. Pertanto, dal primo studio estraiamo il concetto secondo cui l'abbassamento causato dallo stress idraulico fornisce informazioni cruciali per caratterizzare un acquifero, e lo proiettiamo nel campo della modellazione delle acque sotterranee. Infatti, considerare l'abbassamento in fase di modellazione sarebbe molto più semplice rispetto all'utilizzo del livello piezometrico, in quanto le condizioni al contorno e iniziali da considerare sono omogenee (zero). Il problema sta nel fatto che gli abbassamenti non vengono misurati direttamente, ma si derivano dalle misure della variazione del livello della falda. Gli abbassamenti che ne derivano possono subire imprecisioni persistenti in sistemi complessi con perturbazioni esterne prolungate e incerte. In altre parole, la stima degli abbassamenti viene influenzata non solo da errori nelle misure della piezometria, ma anche dalle stime dell'evoluzione naturale della falda acquifera (cioè il livello che ci sarebbe stato se il test di pompaggio non fosse stato effettuato) . Ciò rende difficile utilizzare gli abbassamenti nei modelli di flusso e costringe i modellatori a utilizzare i livelli piezometrici e informazioni difficili da quantificare. Nel terzo capitolo del presente studio presentiamo un metodo per filtrare gli errori sistematici nei dati di abbassamento (stimati) durante la calibrazione automatica di un modello di flusso. Per fare ciò, introduciamo un termine di correzione della distorsione (bias) in un problema inverso composto che combina un modello dei livelli naturali con un

modello degli abbassamenti. Dato che questi due modelli condividono gli stessi parametri, viene sviluppato un algoritmo iterativo di ottimizzazione in due fasi per stimare congiuntamente il bias, le tendenze naturali e i parametri idraulici. Il metodo viene presentato attarverso un esempio sintetico in un acquifero eterogeneo. L'esempio mostra che il metodo converge alla migliore stima condizionale anche quando i dati dei livelli piezometrici sono fortemente distorti. Inoltre, nello stesso esempio, mostriamo che l'utilizzo di dati di piezometria distorti nell'applicazione del problema inverso tradizionale può fornire buoni fittings, ma in questo caso il bias porta a una stima errata del campo di trasmissività.

Nel quarto capitolo applichiamo il metodo presentato nel capitolo precedente, insieme all'inversione stocastica, nel nucleo del SdA. Si vuole caratterizzare la distribuzione spaziale della conducibilità idraulica su larga scala, con particolare attenzione per l'individuazione di strutture di connettività (canali altamente conduttivi) che controllano il flusso delle acque sotterranee e il trasporto degli inquinanti. Negli acquiferi evaporitici, questi canali preferenziali possono essere costituiti da condotti carsici, sviluppati a diverse scale, nonché da zone di faglia. In questo contesto si è indagato se sia possibile utilizzare l'inversione stocastica per caratterizzare la presenza di strutture di connettività nell'acquifero evaporitico del SdA (un area ampia, circa 1500 km^2) utilizzando i livelli piezometrici misurati in numerosi punti di osservazione durante una sequenza di tre prove idrauliche. I risultati mostrano che, sebbene la soluzione non sia univoca, vengono individuate le principali zone di flusso preferenziale. Gli abbassamenti calcolati a partire da diverse simulazioni risultano essere simili agli abbassamenti osservati, con errori massimi di pochi centimetri. Il flusso preferenziale viene individuato non solo a partire da regioni allungate di alta permeabilità, ma anche da un marcato effetto scala (le trasmissività del modello sono circa 30 volte maggiori di quelle stimate attraverso prove di pompaggio corte). Le principali zone di alta conducibilità sono coerenti con informazioni indipendenti basate su geofisica, isotopi, proporzioni di miscelazione, dati piezometrici e processi di dissoluzione previsti. Infine, per comprendere meglio le dinamiche di sviluppo di questi percorsi di

flusso preferenziali e i loro effetti sul comportamento di flusso e trasporto, eseguiamoo un esperimento di dissoluzione in condizioni controllate. Passiamo a un'analisi su scala intermedia poiché le strutture di connettività organizzate (*wormholes*) possono svilupparsi su scale spaziali e temporali diverse. Grazie a studi precedenti, conosciamo le condizioni ottimali in cui queste strutture possono formarsi, ma la loro evoluzione spazio-temporale, così come la ridistribuzione del flusso tra i canali e le variazioni nei processi di trasporto, sono in gran parte sconosciute. Pertanto, eseguiamo un esperimento di dissoluzione in un acquifero evaporitico sintetico, insieme a diverse prove di tracciante, per studiare l'evoluzione di una struttura di dissoluzione caratterizzata da *wormholes* dominanti. Analizziamo l'evoluzione della dinamica dei *wormholes*, con particolare attenzione per la loro crescita, i cambiamenti nelle proprietà idrauliche del sistema, la loro geometria e la competizione per il flusso. Osserviamo come il flusso viene ridistribuito con lo sviluppo dei *wormholes*, così come alcune evidenze dei fattori scatenanti e amplificatori che intervengono nel meccanismo di auto-organizzazione che porta a queste strutture di dissoluzione. Inoltre, interpretando le curve di arrivo delle prove di tracciante, possiamo quantificare l'effetto che queste strutture hanno sul comportamento idraulico e di trasporto. Per questo, applichiamo il modello di avvezione multipla e dispersione, considerando due diversi approcci: adattando le curve di arrivo misurate con i parametri di trasporto effettivi del sistema e prevedendo l'evoluzione della curva di arrivo attraverso un modello discreto dei *wormholes*, che viene applicato conoscendo la geometria del sistema e i parametri di trasporto della matrice indisciolta. Entrambi gli approcci sono in grado di riprodurre i dati sperimentali, evidenziando la capacità di caratterizzare il sistema. I risultati dimostrano anche l'elevato potere predittivo del modello discreto dei *wormholes*.

Resum

La caracterització dels aqüífers evaporítics per comprendre millor els processos hidrodinàmics i geoquímics és de gran importància, especialment en entorns on tant la sostenibilitat d'ecosistemes únics com els interessos econòmics depenen de les característiques de l'aqüífer. És el cas del nucli evaporític del Salar d'Atacama (SdA), "motor" d'aquesta tesi, que ens impulsa a perseguir dos objectius principals. Primer, caracteritzar el comportament hidràulic del nucli del SdA, amb especial atenció a la identificació d'estructures altament connectades (camins de flux preferent). En segon lloc, enriquir el coneixement sobre el desenvolupament de zones de flux preferent causades pels processos de dissolució (és a dir, la dinàmica dels forats de cuc, comunament anomenats *wormholes*) i els canvis corresponents en el comportament del flux i del transport.

Per caracteritzar un aqüífer, se solen realitzar proves de bombament que permeten comprendre el model conceptual del sistema, a través de diagrames de diagnòstic, i estimar les propietats hidràuliques. Entre les diverses proves, les de recuperació consisteixen en mesurar les variacions del nivell piezomètric en pous de bombament i/o de monitorització un cop finalitzada la prova de bombament. Aquestes proves són especialment útils quan el cabal no es pot controlar amb precisió. Agarwal va proposar un mètode, que s'ha convertit en estàndard en la indústria petroliera, per obtenir la resposta de l'aqüífer al bombament a partir de les dades de recuperació. No obstant això, el mètode ha estat provat i verificat de forma limitada. En el segon capítol d'aquesta tesi analitzem el mètode d'Agarwal per comprendre les seves limitacions i superar-les. Els nostres resultats mostren que el mètode d'Agarwal proporciona excel·lents gràfiques de recuperació (és a dir, la corba de descens que s'obtindria durant el bombament) i bones estimacions dels paràmetres hidràulics per a gairebé totes les condicions de l'aqüífer, sempre que s'utilitzi un cabal constant i que la derivada logarítmica a la fi del bombament sigui constant. Aquestes condicions són massa limitants per a la seva aplicació en

la hidrologia d'aigües subterrànies, on se solen monitoritzar diversos pous d'observació. Per tant, generalitzem el mètode d'Agarwal (1) derivant un temps equivalent per a cabals que varien en el temps i (2) proposant obtenir les corbes de descens durant la recuperació extrapolant els descensos de la fase de bombament. D'aquesta manera obtenim excel·lents gràfics de diagnòstic que faciliten l'anàlisi del model conceptual i permeten aplicar el mètode per a una àmplia gamma de condicions.

No obstant això, la interpretació de les provas hidràuliques basades en l'anàlisi de dades de descens és difícil de realitzar per caracteritzar grans sistemes aqüífers amb una dinàmica de flux complexa, impulsada, per exemple, per grans camps de bombament. En aquest cas, la caracterització generalment s'aconsegueix a través de models d'aigües subterrànies. Per tant, partint de la base que els descensos deguts al estrès hidràulic contenen informació crucial per caracteritzar un aqüífer, projectem el concepte en la modelació d'aigües subterrànies. Considerar el descens en la modelació seria molt més fàcil que fer servir el nivell piezomètric, perquè els descensos estan subjectes a condicions de contorn i inicials homogènies (zero). El problema rau en el fet que els descensos no es mesuren directament, sinó que es deriven a partir dels mesuraments de variació del nivell. Els descensos resultants poden patir inexactituds persistents en sistemes complexos amb pertorbacions externes incertes i prolongades. D'aquesta manera, els descensos estimats es veuen afectats no només per errors en els mesuraments del nivell, sinó també per les estimacions de l'evolució natural del mateix (és a dir, el nivell que hi hauria si la prova de bombament no s'hagués realitzat) . Això dificulta l'ús dels descensos en els models de flux i obliga els modeladors a emprar els nivells piezomètrics i informació suau. En aquest context, en el tercer capítol presentem un mètode per filtrar errors sistemàtics en les dades de descens durant el calibratge automàtic d'un model de flux. Per fer això, introduïm un terme de correcció del biaix en un problema invers compost que combina un model de nivell natural amb un model de descens. Atès que aquests dos models comparteixen els mateixos paràmetres, es desenvolupa un algoritme iteratiu d'optimització de dues fases per estimar conjuntament el biaix, les tendències

naturals i els paràmetres. El mètode s'il·lustra amb un exemple sintètic en un aqüífer heterogeni. L'exemple mostra que el mètode convergeix a la millor estimació condicional fins i tot quan les dades de nivell estan fortament esbiaixades. En el mateix exemple, vam demostrar que l'ús de dades de nivell esbiaixades en el problema invers tradicional també pot proporcionar bons ajustos però, en aquest cas, el biaix condueix a una estimació incorrecta del camp de transmissivitat.

En el quart capítol apliquem el mètode presentat en el capítol anterior, acoblat a la inversió estocàstica, al nucli del SdA. Volem caracteritzar la distribució espacial de la conductivitat hidràulica a gran escala, amb especial atenció per a la identificació d'estructures de connectivitat (canals altament conductius) que controlen el flux d'aigua subterrània i el transport de contaminants. En els aqüífers evaporítics, aquests canals preferents poden consistir en conductes càrstics, desenvolupats a diferents escales, així com en zones de falla. En aquest context, vam investigar si és possible utilitzar la inversió estocàstica per caracteritzar la presència d'estructures de connectivitat a l'aqüífer evaporític del SdA (amb una gran extensió, al voltant de 1500 km^2) usant els nivells mesurats en nombrosos punts d'observació durant una seqüència de tres proves hidràuliques. Els resultats mostren que, tot i que la solució no és única, s'identifiquen les principals zones de flux preferent. Nombroses inversions produeixen ajustos similars als descensos observats, amb errors màxims de pocs centímetres. El flux preferent s'identifica no només per regions allargades d'alta permeabilitat, sinó també per un marcat efecte d'escala (les transmissivitats del model són unes 30 vegades més grans que les estimades a través d'assajos de bombament curts). Les principals zones d'alta conductivitat són consistents amb informació independent basada en geofísica, isòtops, proporcions de mescla, dades piezomètriques i els processos de dissolució esperats.

Finalment, per comprendre millor la dinàmica de desenvolupament d'aquests camins de flux preferent i els seus efectes sobre el comportament de flux i transport, duem a terme un experiment de dissolució en condicions controlades. Passem a una anàlisi d'escala intermèdia ja que les estructures de

connectivitat organitzades (*wormholes*) poden desenvolupar-se en diferents escales espacials i temporals. Gràcies a estudis previs coneixem les condicions òptimes en què es poden formar aquestes estructures, però la seva evolució espai-temporal, així com la redistribució del flux entre canals i els canvis en els processos de transport, són en gran part desconeguts. Així, vam realitzar un experiment de dissolució en un aqüífer evaporític sintètic, juntament amb diverses proves de traçador, per estudiar l'evolució d'un patró de dissolució caracteritzat per *wormholes* dominants. Analitzem l'evolució de la dinàmica dels *wormholes*, amb especial atenció per al creixement dels mateixos, els canvis en les propietats hidràuliques del medi, la geometria dels *wormholes* i la competició pel flux. Observem com es redistribueix el flux amb el desenvolupament dels *wormholes*, així com algunes evidències dels factors desencadenants i amplificadors que intervenen en el mecanisme d'autoorganització que condueix a aquestes estructures de dissolució. A més, a l'interpretar les corbes d'arribada de les proves de traçador, podem quantificar l'efecte que aquestes estructures tenen sobre el comportament hidràulic i de transport. Per això, apliquem el model d'advecció múltiple i dispersió, considerant dos enfocaments diferents: ajustant les corbes d'arribada mesurades amb paràmetres de transport efectius i predient l'evolució de la corba d'arribada a través d'un model discret de *wormholes*, que s'aplica coneixent la geometria del sistema i els paràmetres de transport de la matriu no dissolta. Tots dos enfocaments són capaços de reproduir les dades experimentals, destacant la capacitat de caracteritzar el sistema. Els resultats també demostren l'alt poder predictiu del model discret de *wormholes*.

Resumen

La caracterización de los acuíferos evaporíticos para comprender mejor los procesos hidrodinámicos y geoquímicos es de gran importancia, especialmente en entornos donde tanto la sostenibilidad de ecosistemas únicos como los intereses económicos dependen de las características del acuífero. Este es el caso del núcleo evaporítico del Salar de Atacama (SdA), "motor" de esta tesis, que nos impulsa a perseguir dos objetivos principales. Primero, caracterizar el comportamiento hidráulico del núcleo del SdA, poniendo especial atención en la identificación de estructuras altamente conectadas (caminos de flujo preferente). En segundo lugar, contribuir al conocimiento sobre el desarrollo de zonas de flujo preferente causadas por procesos de disolución (es decir, la dinámica de los agujeros de gusano, comúnmente llamados *wormholes*) y los correspondientes cambios en el comportamiento del flujo y del transporte.

Para caracterizar un acuífero, se suelen realizar pruebas de bombeo que permiten comprender el modelo conceptual del sistema a través de diagramas de diagnóstico, y estimar las propiedades hidráulicas. Entre las diversas pruebas, las de recuperación consisten en medir las variaciones del nivel piezométrico en pozos de bombeo y/o de monitoreo una vez finalizada la prueba de bombeo. Estas pruebas son especialmente útiles cuando el caudal no se puede controlar con precisión. Agarwal propuso un método, que se ha convertido en estándar en la industria petrolera, para obtener la respuesta del acuífero al bombeo a partir de los datos de recuperación. Sin embargo, el método ha sido probado y verificado de forma limitada. En el segundo capítulo de esta tesis analizamos el método de Agarwal para comprender sus limitaciones y superarlas. Nuestros resultados muestran que el método de Agarwal proporciona excelentes gráficas de recuperación (es decir, la curva de descenso que se obtendría durante el bombeo) y buenas estimaciones de los parámetros hidráulicos para

casi todas las condiciones del acuífero, siempre que se utilice un caudal constante y que la derivada logarítmica al final del bombeo sea constante. Estas condiciones son demasiado limitantes para su aplicación en hidrología de aguas subterráneas, donde se suelen monitorear varios pozos de observación. Por lo tanto, generalizamos el método de Agarwal (1) derivando un tiempo equivalente para caudales que varían en el tiempo y (2) proponiendo obtener las curvas de descenso durante la recuperación extrapolando los descensos de la fase de bombeo. De esta forma obtenemos excelentes gráficos de diagnóstico que facilitan el análisis del modelo conceptual y permiten aplicar el método para una amplia gama de condiciones.

Sin embargo, la interpretación de las prueba hidráulicas basadas en el análisis de datos de descenso es difícil de realizar para caracterizar grandes sistemas acuíferos con una dinámica de flujo compleja impulsada, por ejemplo, por grandes campos de bombeo. En este caso, la caracterización generalmente se logra a través de modelos de aguas subterráneas. Por lo tanto, nos quedamos con el concepto de que los descensos debidos a uno stress hidráulico contienen información crucial para caracterizar un acuífero, y proyectamos el concepto en la modelación de aguas subterráneas. Considerar el descenso en la modelación sería mucho más fácil que usar el nivel piezométrico, puesto que los descensos están sujetos a condiciones de contorno e iniciales homogéneas (cero). El problema radica en el hecho de que los descensos no se miden directamente, sino que se deducen de las mediciones de variación del nivel. Los descensos resultantes pueden sufrir inexactitudes persistentes en sistemas complejos con perturbaciones externas, inciertas y prolongadas. De esta manera, los descensos estimados se ven afectados no solo por errores en las mediciones del nivel, sino que también por las estimaciones de la evolución natural del mismo (es decir, el nivel que habría si la prueba de bombeo no se hubiera realizado). Esto dificulta el uso de los descensos en los modelos de flujo y obliga a los modeladores a emplear niveles piezométricos e información cualitativa. En este contexto, en el tercer capítulo presentamos un método para filtrar errores sistemáticos en los datos de descenso durante la calibración automática de un modelo de flujo. Para hacer esto, introducimos un término

de corrección del sesgo en un problema inverso compuesto que combina un modelo de nivel natural con un modelo de descenso. Dado que estos dos modelos comparten los mismos parámetros, se desarrolla un algoritmo iterativo de optimización de dos fases para estimar conjuntamente el sesgo, las tendencias naturales y los parámetros. El método se ilustra con un ejemplo sintético en un acuífero heterogéneo. El ejemplo muestra que el método converge a la mejor estimación condicional incluso cuando los datos de nivel están fuertemente sesgados. En el mismo ejemplo, demostramos que el uso de datos de nivel sesgados en el problema inverso tradicional también puede proporcionar buenos ajustes pero, en este caso, el sesgo conduce a una estimación incorrecta del campo de transmisividad.

En el cuarto capítulo aplicamos el método presentado en el capítulo anterior, acoplado a la inversión estocástica, al núcleo del SdA. En este capítulo queremos caracterizar la distribución espacial de la conductividad hidráulica a gran escala, con especial atención para la identificación de estructuras de conectividad (canales altamente conductivos) que controlan el flujo de agua subterránea y el transporte de contaminantes. En los acuíferos evaporíticos, estos canales preferentes pueden consistir en conductos kársticos, desarrollados a diferentes escalas, así como en zonas de falla. En este contexto, investigamos si es posible utilizar la inversión estocástica para caracterizar la presencia de estructuras de conectividad en el acuífero evaporítico del SdA (gran extensión, alrededor de 1500 km^2) usando los niveles medidos en numerosos puntos de observación durante una secuencia de tres pruebas hidráulicas. Los resultados muestran que, aunque la solución no es única, se identifican las principales zonas de flujo preferente. Numerosas inversiones producen ajustes similares a los descensos observados, con errores máximos de pocos centímetros. El flujo preferente se identifica no solo por regiones alargadas de alta permeabilidad, sino también por un marcado efecto escala (las transmisividades del modelo son unas 30 veces más grandes que las estimadas a través de ensayos de bombeo cortos). Las principales zonas de alta conductividad son consistentes con información independiente basada en geofísica,

isótopos, proporciones de mezcla, datos piezométricos y los procesos de disolución esperados.
Finalmente, para comprender mejor la dinámica de desarrollo de estos caminos de flujo preferente y sus efectos sobre el comportamiento del flujo y transporte, llevamos a cabo un experimento de disolución en condiciones controladas. Pasamos a un análisis de escala intermedia ya que las estructuras de conectividad organizadas (*wormholes*) pueden desarrollarse en diferentes escalas espaciales y temporales. Gracias a estudios previos conocemos las condiciones óptimas en las que se pueden formar estas estructuras, pero su evolución espacio-temporal, así como la redistribución del flujo entre canales y los cambios en los procesos de transporte son en gran parte desconocidos. Así, realizamos un experimento de disolución en un acuífero evaporítico sintético, junto con varias pruebas de trazador, para estudiar la evolución de un patrón de disolución caracterizado por *wormholes* dominantes. Analizamos la evolución de la dinámica de los *wormholes*, con especial atención para el crecimiento de los mismos, los cambios en las propiedades hidráulicas del medio, la geometría de los *wormholes* y la competición por el flujo. Observamos cómo se redistribuye el flujo con el desarrollo de los *wormholes*, así como algunas evidencias de los factores desencadenantes y amplificadores que intervienen en el mecanismo de autoorganización que conduce a estas estructuras de disolución. Además, al interpretar las curvas de llegada de las pruebas de trazador, podemos cuantificar el efecto que estas estructuras tienen sobre el comportamiento hidráulico y de transporte. Para eso, aplicamos el modelo de advección múltiple y dispersión, considerando dos diferentes enfoques: ajustando las curvas de llegada medidas con parámetros de transporte efectivos y prediciendo la evolución de la curva de llegada a través de un modelo discreto de *wormholes*, que se aplica conociendo la geometría del sistema y los parámetros de transporte de la matriz no disuelta. Ambos enfoques son capaces de reproducir los datos experimentales, destacando la capacidad de caracterizar el sistema. Los resultados también demuestran el alto poder predictivo del modelo discreto de *wormholes*.

Contents

Acknowledgements **iii**

Abstract **ix**

List of Figures **xxix**

List of Tables **xxxiii**

List of Abbreviations **xxxv**

1 Introduction **1**

1.1 "The driving force": the Salar de Atacama 2

1.2 Dealing with "the problem": objectives of the thesis 3

1.3 "The plan": thesis outline 4

2 Generalizing Agarwal's method for the interpretation of recovery tests under non-ideal conditions **7**

2.1 Introduction 8

2.2 Methods 11

2.2.1 Agarwal's method 11

2.2.2 Justification and limitations of Agarwal's and Theis' recovery methods 13

2.2.3 Proposed method 16

2.2.4 Variable pumping rate 18

2.3 Performance of recovery test interpretation methods 21

2.3.1 Ideal conditions: importance of the duration of pumping 21

2.3.2 Non-ideal conditions: effects of boundaries and flow dimension . . . 25
2.3.3 Non-ideal conditions: variable pumping rate . . . 27
2.4 Application to real-world data sets . . . 29
2.4.1 Example A: Long pumping test and fast aquifer response 29
2.4.2 Example B: Short pumping test and high delay in aquifer response . . . 30
2.5 Discussion and Conclusions . . . 33

3 Automatic calibration of groundwater models with bias correction and data filtering: Working with drawdown data 37
3.1 Introduction . . . 38
3.2 Background: Formal definition of drawdown . . . 41
3.3 Problem statement and methodology . . . 43
3.3.1 Bias correction . . . 43
3.3.2 Calibration . . . 45
3.4 Application . . . 50
3.4.1 Synthetic scenario . . . 51
3.4.2 The Filtering-Corrective Method . . . 53
3.4.3 Traditional calibration with head data . . . 55
3.5 Results and Discussion . . . 56
3.5.1 Overall performance . . . 56
3.5.2 Natural heads, drawdowns, and bias correction . . . 59
3.5.3 Discussion . . . 62
3.6 Conclusions . . . 63

4 The worth of stochastic inversion for identifying connectivity by means of a long-lasting large-scale hydraulic test: the Salar de Atacama case study 67
4.1 Introduction . . . 68
4.2 Site description . . . 71
4.3 Methodology . . . 76
4.3.1 Large-scale long-term cross-hole hydraulic tests . . . 76

4.3.2 Drawdown estimation and calibration through stochastic inversion . . . 78
Natural head model . . . 81
Drawdown model . . . 83
Parametrization and geostatistical models . . . 84
Calibration using drawdown data . . . 87
The corrective-filtering method . . . 89
4.4 Model results . . . 89
4.4.1 Calibration and identification of flow connectivity structures . . . 89
4.4.2 Comparison with independent data . . . 94
4.4.3 Scale effect of the hydraulic conductivity . . . 98
4.5 Conclusions . . . 99

5 Evaluation of wormhole formation dynamics in an intermediate-scale dissolution experiment: Hydraulic and transport effects 103
5.1 Introduction . . . 104
5.2 Materials and Methods . . . 108
5.2.1 Experimental Setup . . . 108
5.2.2 Estimation of initial hydraulic properties . . . 111
5.2.3 Dissolution Experiment . . . 112
5.2.4 Tracer Test Experiments . . . 113
5.2.5 Mathematical Models . . . 114
Wormhole Competition Model . . . 114
The Multi-Advection Dispersion Model . . . 116
5.2.6 Modeling Approach . . . 118
5.2.7 Image processing . . . 120
5.3 Results and discussion . . . 122
5.3.1 Wormholes Growth Evolution . . . 122
5.3.2 Changes in Hydraulic Properties . . . 126
5.3.3 Wormhole Competition . . . 128
5.3.4 Wormhole capture area . . . 130
5.3.5 Tracer Test Breakthrough Curves . . . 133

Effective Solute Transport Modeling 134
Physical Interpretation of Effective Parameters 138
Discrete Wormhole Transport Modeling 139
5.3.6 Joint discussion on experimental results 141
5.4 Conclusions 142

6 Conclusions **147**
6.1 Overall conclusions 148

A Porosity Changes from Total Mass Measurements **151**

B Publications **153**

List of Figures

2.1 Drawdown and drawdown residual as a result of variable pumping rate. . . . 9
2.2 Pumping and recovery test. . . . 12
2.3 Drawdown terms used for the estimation of both Agarwal (s_A) and the proposed drawdown (s_M). . . . 17
2.4 Comparing Agarwal's and the proposed method for recovery test interpretation under ideal conditions. . . . 22
2.5 Relative errors of drawdowns and log-derivatives resulting from both Agarwal's (Line) and the proposed method (Dash Dot) under ideal conditions. . . . 24
2.6 Comparing Agarwal's and the proposed method for recovery test interpretation under non-ideal conditions. . . . 26
2.7 Comparing Agarwal's and the proposed method for recovery test interpretation under ideal conditions and variable pumping rate. . . . 28
2.8 Applying Agarwal's and the proposed method to real data-sets. 31

3.1 Estimating drawdowns using a bias corrective term. . . . 44
3.2 Schematic description of the proposed method. . . . 49
3.3 Synthetic example of drawdown estimation. . . . 50
3.4 Synthetic aquifer system domain. . . . 51
3.5 Anthropic and natural factors causing head changes in the aquifer. 52
3.6 Sequence of estimated hydraulic parameters (T and S) and drawdown fields along the iterative process. . . . 57

3.7 Comparison of calibration results applying traditional inversion with noisy and biased measurements and exact measurements, as well applying the proposed method. 58
3.8 Drawdowns and natural heads calculated along the iterative process. 60
3.9 Evolution of the absolute difference between imposed error and estimated bias correction for each observation well. 61

4.1 Main features of the Salar de Atacama. 72
4.2 Long-term cross-hole hydraulic test. 77
4.3 Recorded head data and factors that influenced flow dynamics during the hydraulic test period. 79
4.4 Model set up and available hydraulic conductivity data. 82
4.5 Model parametrization. 85
4.6 Experimental and estimated variogram. 86
4.7 Calibration results are presented in terms of calculated and measured relative heads vs. time. 92
4.8 Normalized estimates of hydraulic conductivity fields. 94
4.9 Comparison of estimated hydraulic conductivity fields with independent data. 97
4.10 Scale effect of the hydraulic conductivity. 98

5.1 Top view of the experimental tank 109
5.2 Diagram of the experimental set-up 110
5.3 Schematic representation of a porous medium characterized by wormholes and sketch of two possible transport modelling approaches. 117
5.4 Image analysis to estimate wormhole length. 121
5.5 Evolution of the dissolution pattern over time. 122
5.6 Dissolution structures at the end of the dissolution experiment. 124
5.7 Wormhole growth rate: length evolution is plotted for each wormhole developed in the aquifer. 125

5.8 Temporal evolution of aquifer hydraulic properties estimated from experimental data. 127
5.9 Analysis of the dissolution pattern: wormholes density. 128
5.10 Estimating capture areas through image analysis. 131
5.11 Comparison between estimated capture areas. 132
5.12 Experimental tracer breakthrough curves obtained during the initial and final tracer tests. 134
5.13 Best fit of the effective transport model resulting from the calibration of the initial tracer test experiment. 135
5.14 Normalized breakthrough curve concentrations resulting from the calibration of the final tracer test. 136
5.15 Normalized breakthrough curve concentrations resulting from two blind predictions of the final tracer test. 140

List of Tables

2.1 Hydraulic properties estimates applying the method to real-world data sets. 32

4.1 Parameters of geostatistical models set to apply the inverse problem with pilot points. 86
4.2 Results of the stochastic inversion for six different test problems. 91

5.1 Characteristics of brine solutions 109
5.2 Properties of the synthesized aquifer 111
5.3 Experimental conditions 112
5.4 Length and capture area estimated for each identified wormhole. 130
5.5 Comparison between estimated capture areas. 132
5.6 Results of model calibration of both prior- (T_0) and post-dissolution (T_5) tracer test interpretation. 137
5.7 Contribution β_i of individual pathways to the composite BTC of tracer test T_5. 139

List of Abbreviations

BC	**B**oundary **C**ondition
BTC	**B**reak **T**rhough **C**urve
CE	**C**onditional **E**stimation
CS	**C**onditional **S**imulation
DP	**D**ifferential **P**ressure transducer
EC	**E**lectrical **C**onductivity
SF	**S**alar **F**ault
OW	**O**bservation **W**ell
PP	**P**ilot **P**oint
PT	**P**iezome**T**er
PW	**P**umping **W**ell
RGB	**R**ed **G**reen **B**lue
SI	**S**aturation **I**ndex
SdA	**S**alar **d**e **A**atacama
SQM	**S**ociedad **Q**uímica y **M**inera

Chapter 1

Introduction

1.1 "The driving force": the Salar de Atacama

The Salar de Atacama is a huge endhoreic evaporitic aquifer located in one of the most arid desert of the world. It is the third largest salt-flat after Uyuni (Bolivia) and Salinas Grande (Argentina), and it is characterized by exceptional environmental and economic features that make it unique.

On the one hand, the genesis of the Salar and hyper-arid conditions favor uncommon sub-aerial ecosystems, which must be protected. Beautiful landscapes and a sequence of lagoons that act as centre for Andean Flamingo breeding (Ortiz et al., 2014) confer to the SdA a high environmental value. Thus, the Salar is exploited by local populations for ecotourism activities (Liu and Agusdinata, 2020). On the other hand, most of its economic resources lie beneath the salt-flat surface, within the evaporitic aquifer, filled with brine highly-concentrated in valuable elements as Potassium and Lithium (mobile resources) (Kesler et al., 2012; Vikström et al., 2013). While the former is mainly used as fertilizer, the latter is mostly directed to Ceramics (32%) and Batteries market (35%) (Swain, 2017). In recent years, its production is experimenting a huge increase, given the increasing demand for clean technologies. These economic interests lead to the exploitation of the SdA nucleus by pumping the aquifer brine, which is subsequently evaporated and processed to obtain the minerals of interest (Pueyo et al., 2017).

In this context, it is of paramount importance to characterize the entire SdA nucleus from a hydrogeological viewpoint, understanding flow and transport behavior for i) comprehending the interaction between the nucleus and its surroundings, ii) sustaining the fragile equilibrium between ecosystems and economic activities, and iii) improving the efficiency of mining operations. In the last decades the reservoir has been characterized from a geological, hydrogeological and geochemical perspective to understand the dynamics of the system (Kampf et al., 2005; Jordan et al., 2007; Boutt et al., 2016; Munk et al., 2018; Marazuela et al., 2018, 2019). But given its complexity, deeper studies are required, including a characterization at large-scale, aimed at understanding flow and transport behaviour and connectivity structures of

the nucleus. The purpose is not easy to achieve, because of several aspects, including i) the large dimension of the system, ii) the complexity of flow dynamics, and iii) the possible geochemical instabilities that could re-shape the aquifer architecture. With this work we embrace this complexity and we try to understand how to deal with its various aspects.

1.2 Dealing with "the problem": objectives of the thesis

We face the problem from two main points of view. On the one hand, we consider physical processes in terms of hydraulic behavior within the aquifer, i.e. the hydrodynamics of the system. As widely known, an aquifer system responds to several hydraulic stresses, natural and anthropic, depending on its hydraulic properties and connectivity. The latter, in turn, is closely related to the architecture of the aquifer.

Within this framework, part of the thesis is aimed at understanding and characterizing the hydraulic features of the aquifer at large scale, i.e. covering the whole Halite nucleus (ca. 1600 km^2). Special attention is given to connectivity structures. Considering the karst nature of the system, these structures may control large-scale hydraulic conductivity in the SdA nucleus. In other words, the first objective is that of "taking a picture" of the current aquifer system architecture at a scale of tens of kilometers.

However, since the SdA nucleus is a karst environment, we must also consider how the synergy between hydrodynamics and geochemistry may have led, or may lead, to past and future evolution of the aquifer. Two main geochemical processes could be involved in karst aquifers: mineral precipitation and dissolution. Both processes may occur in the SdA nucleus, even assuming that the brine filling the aquifer is in equilibrium with halite. Precipitation would possibly occur either from thermodynamic changes or from mixing of saturated brines of different concentrations. On the other hand, dissolution may occur in areas where under-saturated brine reaches the nucleus (if any) or, once again, from thermodynamic changes within the aquifer.

In this work we focus the attention on dissolution processes, which can lead to major changes in the hydraulic properties of the system and can greatly affect the degree of connection within the nucleus, and between the nucleus and its surroundings. These would lead to important changes in flow and transport behavior of the aquifer system. Thus, part of the thesis is aimed at enriching the knowledge on multiple aspects of the evolution of dissolution structures characterized by preferential flow-paths (i.e. wormholes dynamics), analysing the effects on hydraulic and transport behavior.

1.3 "The plan": thesis outline

Following what previously enunciated, the efforts are initially focused on the characterization of the SdA nucleus. Hydraulic testing is initially selected as the main approach to gain a conceptual understanding of the system and to estimate hydraulic properties. The idea is to interpret the response of the aquifer analyzing drawdown recovery, usually subject to less external perturbations than the drawdown in itself. In this context,

- in Chapter 2 we analyze Agarwal's method, originally developed for the interpretation of recovery tests under ideal conditions. We first verify it under ideal and non-ideal conditions. Next, we present an alternative method to overcome its limitations. Finally, we propose an improved equivalent time to consider variable pumping rate in the interpretation of recovery data.

However, when we start processing measured hydraulic test data in SdA, we realize that the first methodology chosen for the interpretation is not the most suitable. The complexity of the system, production dynamics and the numerous precipitation events inevitably require a different and more complex approach for interpreting the aquifer response to external stresses. At the same time, we want to continue working with drawdowns, which contain the most valuable qualitative and quantitative information about the hydraulic properties of the aquifer and connectivity. In this framework,

- in Chapter 3 we present a new filtering-corrective method aimed at calibrating groundwater models employing drawdown data. The proposed method is aimed at 1) filter systematic errors that could arise from the modelling process, 2) de-trend head measurements, and 3) estimate hydraulic properties of the aquifer through inverse stochastic modeling. We test the new methodology applying it to a synthetic aquifer.

Once developed and verified the new methodology, we employ it for the characterization of the Salar de Atacama nucleus, focusing the attention on identifying possible connectivity structures. In this context,

- Chapter 4 is devoted to the long-lasting hydraulic test performed at SdA. During one year we measured data to apply the inverse stochastic approach, jointly with the filtering-corrective method (presented in Chapter 3), for characterizing the spatial variability of transmissivity and possible flow-path structures. We finally tested the consistence of the results by comparison with independent data (mixing ratio, isotopic data, geophysical data, piezometric levels).

Once the hydraulic features of the SdA are identified on a large scale, we move on to an intermediate-scale controlled environment to study part of the processes that can influence (or have influenced) the evolution of the evaporitic aquifer. In this context,

- in Chapter 5 we present a laboratory dissolution experiment and a sequence of tracer tests. We investigate the 1) wormholes evolution, 2) the mechanism of competition for the flow involved in their dynamics, and 3) the changes in flow and transport behavior. Moreover, we seek for conceptual transport models capable of explaining the concentration breakthrough curves. We consider two possible modelling approaches, based on an effective multi-advective dispersion model and a discrete wormhole model.

Finally, in Chapter 6 we present the main conclusions.

Chapter 2

Generalizing Agarwal's method for the interpretation of recovery tests under non-ideal conditions

This chapter is an edited version of: Trabucchi, M., Carrera, J., & Fernàndez-Garcia, D. (2018). Generalizing Agarwal's method for the interpretation of recovery tests under non-ideal conditions. *Water Resources Research*, 54, 6393–6407. https://doi.org/10.1029/2018WR022684 (Appendix B)

2.1 Introduction

Hydraulic testing is the most widely used technique for aquifer systems characterization and the only one providing direct estimates of aquifer parameters through the interpretation of the aquifer response to pumping or other hydraulic perturbations. Well testing results are a function of the range and the quality of the drawdown and rate data available, and of the approach used for their interpretation (Gringarten et al., 2008). Pumping test interpretation emerged largely from the Theis (1935) analytical solution for the drawdown caused in an ideal homogeneous, infinite and confined aquifer, by pumping at a constant rate Q from a fully penetrating well. A feature of this solution is that, when sufficient time has elapsed since the beginning of pumping, the drawdown increases linearly with the logarithm of time. This feature prompted Cooper Jr and Jacob (1946) (CJ in the following) to develop the straight–line method for applying Theis' method through a manageable logarithmic approximation of the analytical solution, which works very well also for a broad range of conditions, including heterogeneous formations (Halford et al., 2006; Meier et al., 1998). Re-reading the paper of Theis (1935) is joyful, because he himself identified the numerous limitations of his solution (we suspect that his USGS colleagues and reviewers must have helped). In reality, aquifers are rarely homogeneous or fully confined and they have boundaries. Storage release is not instantaneous, but delayed with respect to head variations. Wells do not fully penetrate the aquifer and may have significant storage. Over the years, hydrologists and oil engineers developed numerous analytical solutions to overcome these limitations (see, e.g., Kruseman and de Ridder (1990)). While the main purpose of these methods was to estimate transmissivity T and storage coefficient S, they realized that drawdown curves contain a wealth of information about the well and the aquifer beyond the actual value of hydraulic parameters. Unfortunately, the large number of solutions and the subtle variations among them made it difficult

to identify which one is best. Prompted by the need to emphasize conceptual model identification, Bourdet et al. (1983, 1989) proposed using diagnostic plots (simultaneous plot of drawdowns and log-derivatives) to highlight subtle variations in the aquifer response to pumping (Renard et al., 2009). Diagnostic plots are useful, because they complement other information (local geology, geophysics, well logs, etc.) in identifying non-ideal conditions during the pumping test. Given the qualitative nature of the conceptual model selection, it is nice to be able to examine diagnostic plots that can be compared to those of standard models or simply be used to assess how the resistance to flow evolves away from the pumping well.

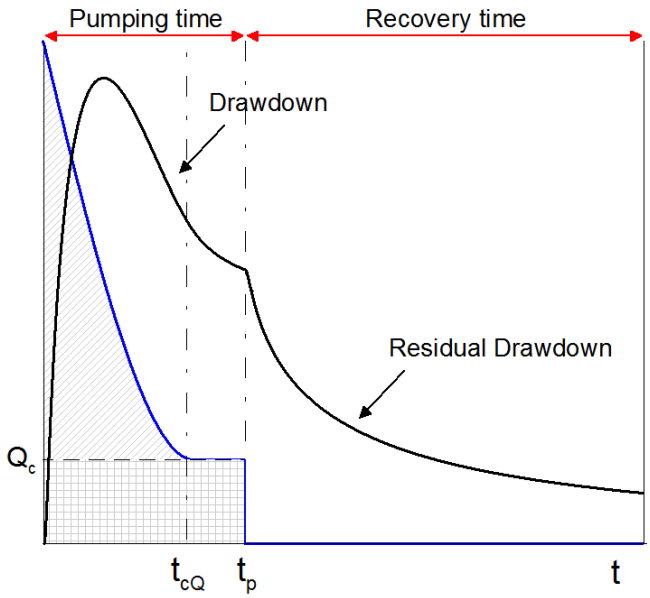

Figure 2.1: Drawdown and drawdown residual as a consequence of a pumping test carried out applying a variable pumping rate. The pumping rate decrease with the time, becoming constant for a while after pumping shut down.

But precisely because of their high sensitivity, log-derivatives require exquisite test performance. While methods can be used to obtain smooth log-derivatives (Ramos et al., 2017), they require a constant pumping rate, which is difficult

to guarantee. Pumping rate can change for numerous reasons. For one thing, well owners do not care for transmissivity but for well production, which can be improved through development and ascertained through step pumping. Even when a pumping test is performed, maintaining a constant pumping rate during the whole test may be difficult. Pump efficiency may cause the pumping rate to decrease over time (Figure 2.1), variations of well efficiency often cause the pumping rate to increase over time, and electrical problems can cause short black outs (zero flow rate). A constant rate may prove impossible in low permeability formations, when the well often goes dry, or when pumping by air lift. Things may get even worse when trying to interpret the hydraulic response to fracking. What can be done in all these cases is to monitor pumping rate and drawdowns recovery. Recovery data (i.e., residual drawdowns measured after pumping has stopped) are much less noisy than pumping data because they are subject to less external perturbations during data acquisition (Figure 2.1). Specifically, pumping rate variability does not affect the aquifer response directly but only indirectly. However, residual drawdowns are affected by environmental fluctuations (e.g., seasonal changes in recharge, tidal effects, uncontrolled nearby pumping, stage changes in close rivers, etc.), which usually dominate the late time recovery and must be filtered out prior to interpretation (see, e.g., Halford et al. (2012)). The traditional method for recovery interpretation was also proposed by Theis (1935). The method is quite robust in estimating effective transmissivity values over a region that grows with the duration of pumping (Willmann et al., 2007; Copty et al., 2011), but lacks information about the storage coefficient. Numerous methods have been introduced to overcome this limitation (Agarwal et al., 1980; Ashjari, 2013; Ballukraya and Sharma, 1991; Banton and Bangoy, 1996; Chenaf and Chapuis, 2002; Çimen, 2015; Zheng et al., 2005), which suggests that recovery data contain information similar to that of the pumping phase of the test. Most of these methods are straight-line-methods based on CJ's approximation that allow evaluating hydraulic parameters, but do not yield any information about the conceptual model. Yet, Agarwal et al. (1980) introduced a method, based on CJ's approximation, to reproduce the response of

a pumping test using recovery test data. In other words, his method permits plotting recovery data as if they resulted from a constant pumping rate, facilitating not only the estimation of hydraulic parameters, but also conceptual model assessment. Given its simplicity, Agarwal's method should be considered as a very effective method for well test data interpretation. In fact, it has become the method of choice in the oil industry. Agarwal et al. (1980) showed that his method reproduced the type curves of Earlougher Jr et al. (1974) and Gringarten et al. (1979) that account for skin effect and wellbore storage. He also tested the validity for the case of a well intersected by a vertical fracture. However, the method lacks theoretical support for conditions other than those of CJ. The objective of this work is to 1) analyze the conditions under which Agarwal's method is valid, to 2) generalize it for variable pumping rate and to 3) propose alternative methods for recovery data interpretation.

2.2 Methods

We first describe Agarwal's method. We then analyze the validity of the method, which naturally leads to a new approach that overcomes the limitations. Finally, we propose a method for variable pumping rate conditions.

2.2.1 Agarwal's method

Agarwal initially developed his method for recovery test interpretation with the implicit assumption of an ideally large, homogeneous and confined aquifer, subject to a constant pumping rate from a fully penetrating well for a sufficiently long time. Under these conditions, flow towards the well is radial, and the CJ equation yields a good approximation for late time drawdowns, i.e., $s(t) = Q \setminus (4\pi T) ln(2.25Tt \setminus (r^2 S))$, where Q is pumping rate and r is distance to the center of the pumping well or effective radius of the well when computing drawdowns at the pumping well itself.

Based on the superposition principle, this author defined what we now call Agarwal drawdown as (Figure 2.2):

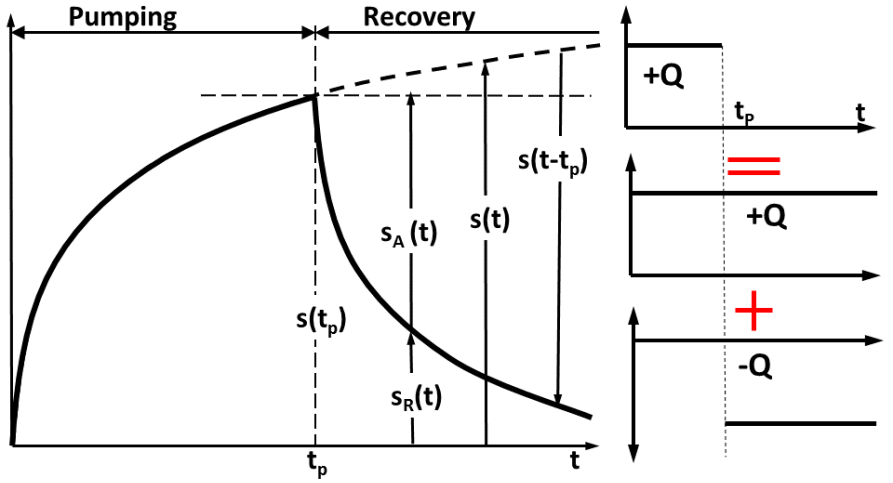

Figure 2.2: Pumping and recovery test. The left graph displays the residual drawdown, s_R, used in Theis recovery method and Agarwal's drawdown s_A. Both can be computed by superposition (right) of a continuous pumping $(+Q)$ and an injection $(-Q)$ that start at the time t_p when pumping stopped in reality.

$$s_A(t) = s(t_p) - s_R(t) = s(t_p) - (s(t) - s(t - t_p)) \qquad t > t_p, \tag{2.1}$$

where t is the time elapsed since the beginning of pumping, t_p is the time at the end of pumping, and $s_R(t)$ is the (Theis) residual drawdown. The latter "will be the same as if discharge of the well had continued but a recharge well with the same flow had been introduced at the same point at the instant discharge stopped" (Theis, 1935).

That is, superposition implies that $s_R(t) = s(t) - s(t - t_p)$. Agarwal then used the CJ's approximation to the three drawdowns appearing in equation (3.9), which yields:

$$s_A(t) = \frac{Q}{4\pi T}\left[ln\left(\frac{2.25Tt_p}{r^2S}\right) - ln\left(\frac{2.25Tt}{r^2S}\right) + ln\left(\frac{2.25T(t-t_p)}{r^2S}\right)\right] \\ = \frac{Q}{4\pi T} ln\left(\frac{2.25T}{r^2S} t_A\right) \tag{2.2}$$

The resulting equation has exactly the same form as that of CJ for a pumping test, but using t_A, implicitly defined as $t_A = t_p(t - t_p) \setminus t$, instead of t. Therefore, Agarwal proposed, without further justification, treating s_A versus t_A as the drawdown curve caused by pumping Q. This is quite surprising because the CJ's approximation does not hold for small recovery times $(t - t_p)$, and, yet, the method works fine.

Four nice features of this approximation are worth pointing. First, t_A is comparable to $(t - t_p)$ when t_p and t are comparable (i.e., when t_p is large). Second, when t tends to infinity, t_A tends to t_p, i.e., Agarwal's method will not yield a (pumping) drawdown curve longer than the pumping period. Third, s_A can be obtained directly from measured variables (drawdown at the end of pumping and residual drawdown). Fourth, as we shall see, the method works quite well. All of them explain the success of the method in the oil industry, where application is immediate, as the test simply consists of monitoring the pressure build-up after well shut-in. Still, general applications demand justification and, possibly, seeking alternative approximations.

2.2.2 Justification and limitations of Agarwal's and Theis' recovery methods

This section analyzes the assumption of long time constant pumping rate needed by Agarwal's method to adopt the CJ's approximation. This limitation can be mathematically analyzed by approximating the Agarwal's drawdown solution with an infinite series. Let us recall first that, in reality, the CJ's

approximation represents the leading term, for large times, of the full Theis solution, which we rewrite in dimensionless variables as:

$$s_D(t_D) = -\gamma + ln(4t_D) + \frac{1}{4t_D} - \frac{1}{2 \cdot 2! \cdot (4t_D)^2} + \frac{1}{3 \cdot 3! \cdot (4t_D)^3} - ... + \frac{(-1)^n}{n \cdot n! \cdot (4t_D)^n} + ..., \tag{2.3}$$

where γ is the Euler constant (γ = 0.57721...), s_D is dimensionless drawdown ($s_D = 4\pi Ts \setminus Q$) and t_D is dimensionless time ($t_D = t \setminus t_c = Tt \setminus Sr^2$). We have chosen to keep the term $4t_D$ without further simplifications in Equation (2.3) to facilitate comparison with the expression in terms of $u(1 \setminus 4t_D)$ typically used in well hydraulics. Substituting Equation (2.3) in the dimensionless form of equation (3.9), i.e., after multiplying (3.9) times $4\pi T \setminus Q$, we obtain (after some elementary but tedious algebra):

$$s_{AD} = -\gamma + ln(4t_{AD}) + \left(\frac{1}{4t_{AD}} - \frac{1}{4t_D}\right) - \frac{1}{2 \cdot 2!}\left(\frac{1}{(4t_{AD})^2} - \frac{t_{pD}^2 - t_D t_{pD} - 2t_D^2}{4^2 t_D^2 t_{pD}(t_D - t_{pD})}\right) + ..., \tag{2.4}$$

where $t_{pD} = t_p \setminus t_c$ and $t_{AD} = t_A \setminus t_c$. Comparing equations (2.3) and (2.4), it becomes obvious that they are identical, up to second order, except for the term $1 \setminus 4t_D$ in (2.4), which becomes negligible when t_D is large. The first order term is also the one controlling the error in the CJ's approximation of the Theis' solution (Equation 2.3), which suggests that Agarwal's method is valid under the same conditions that CJ's approximation would be valid at the end of the pumping phase. Note, however, that the second order term

can be large for small $(t_D - t_{pD})$ and declines only as $1 \setminus (t_D - t_{pD})$ when t_D increases (i.e., the error may persist for a sizeable time for small dimensionless times). These conditions, i.e., large t_{pD} and $(t_D - t_{pD})$, are easy to meet at the pumping well where the characteristic time is small, but not necessarily at the observation well (e.g., for an aquifer with $T = 100\ m^2 \setminus d$, $S = 0.1$, and well radius $r = 0.1\ m$, $t_c = 10^{-5}\ d \cong 1\ s$, but $t_c = 0.9\ d$, at an observation located at $r = 30\ m$). This explains the success of the method in the oil industry, where reservoir tests are routinely performed in production wells, but suggests that it may fail at observation wells.

It is interesting to perform the same analysis for Theis (1935) recovery method, which consists of plotting residual drawdown (ideally, $s_R\ (t) = s(t) - s(t - t_p)$) versus $t_R = t \setminus (t - t_p)$:

$$s_{RD} = ln(t_R) - \frac{t_{pD}}{4t_D(t_D - t_{pD})} + ..., \tag{2.5}$$

where $s_{RD} = 4\pi T s_R \setminus Q$. Note that the error is large for small $(t_D - t_{pD})$. Therefore, it is not, and was never meant to be, appropriate for early time recovery. But the error declines fast as both absolute time since the beginning of pumping, t_D, and recovery time, $t_D - t_{pD}$, increase. In fact, it becomes smaller than Agarwal method for very long recovery $(t_D \gg t_{pD)}$. Moreover, it does not require t_{pD} to be large. In fact, it can be used to interpret slug tests. This fast decline explains the success of Theis recovery method, but also highlights that it is important to keep measuring recovery for a long time. In practice, measuring recovery for a long time after the stop of pumping (and for a comparable time prior to the beginning) is of practical importance to detect head fluctuations caused by factors other than pumping, which is especially important in observation wells. A last comment, the error displayed in equation (2.5) can be eliminated (thus leaving only higher order terms) if CJ's approximation is extended to include the $1 \setminus 4t_D$ term in equation (2.3), which leads to an extended and more accurate interpretation method (Çimen, 2015).

2.2.3 Proposed method

The above analysis suggests an alternative method for interpreting recovery data that overcomes Agarwal's requirement of long pumping time and facilitates the use of early time data from which quantitative, but above all qualitative information can be gained. In fact, as many factors affect short-time data, a great deal of useful information can be obtained, helping in the selection of the most appropriate theoretical aquifer model (Gringarten et al., 1979; Ramey Jr et al., 1970). The fact that the essential assumption behind the Agarwal's method is that the logarithmic approximation is valid (together with practical experience) suggests using CJ's approximation, or any other that the modeler deems appropriate to transform the recovery test drawdown information into that of a pumping test:

$$s_M(t - t_p) = s_{ap}(t) - s_R(t) \qquad t > t_p, \tag{2.6}$$

where $s_{ap}(t)$ is an approximation of $s(t)$ that depends on the modeler's assumption about the behavior of the system. The two most immediate options are (1) $s_{ap}(t) = s(t_p) + m \cdot ln(t_i \setminus t_p)$, if the modeler assumes that flow is radial (dimension n=2) and that a constant slope has been reached; or (2) $s_{ap}(t) = s(t_p) + (2m \setminus (2-n)) \left((t \setminus t_p)^{(1-n\setminus 2)} - 1 \right)$, if the modeler assumes a power-law behavior of the log-derivative (i.e., that flow occurs with a dimension n other than 2). In either case, m is the log-derivative at the end of the pumping phase, or the slope of the drawdown data, divided by 2.3, if they are plotted versus log_{10}t (traditional CJ semi-log plot).

The new approximation (Eq. 6) differs from that of Agarwal (Eq. 1) as the delay in the aquifer response after pumping shut down is taken into consideration. In fact, instead of a constant value $s(t_p)$, an extrapolated function $s_{ap}(t)$ has been considered to evaluate the pumping test drawdown that would have occurred at $t > t_p$ if a longer pumping test had been carried out (Figure 2.3). As the defined function is a straight line with slope m, the new approximation

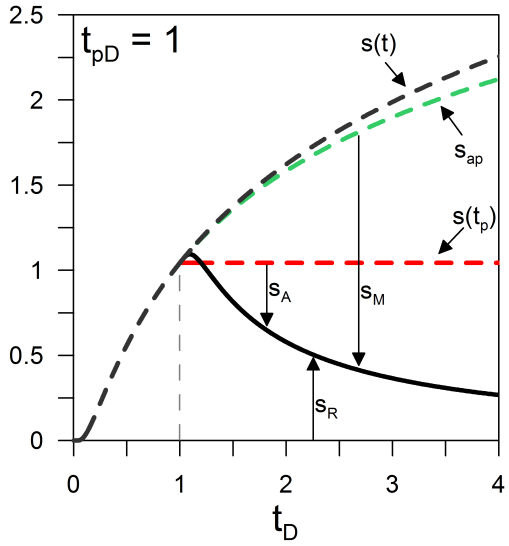

Figure 2.3: Graph showing the different drawdown terms used for the estimation of both Agarwal (s_A) and the proposed drawdown (s_M). It is important to underline the aquifer delay in responding to the pumping shut in (residual drawdown s_R at early recovery times).

$s_{ap}(t)$ tends to CJ's one if quasi steady radial regime has been reached. Otherwise, in transient regime, a straight line with a lower slope will be generated. The latter condition is easy to meet in observation wells where the characteristic time is greater compared to that of the pumping well. Consequently, the aquifer response shows a delay (drawdown may increase for some time after pumping shut in) that can be seen as if the pumping time period would last longer than that in the pumping well. As Agarwal's method was originally developed to analyze data recorded in the pumping well itself (as usually done in the oil and gas industry), the aquifer system behavior for transient time is not taken into account and insufficient pumping time periods lead to negative Agarwal's drawdown.

Applying the proposed method, it is important to underline that 1) we use recovery time $(t - t_p)$ to plot residual drawdown, that means plot data on the same time scale of that of producing time; 2) the evaluation of s_M can be

easily performed using the last pumping time data and recovery data series; 3) as we shall see, the method works quite well, allowing to obtain early-time data curves from recovery data even when the dimensionless duration of pumping is short; but (4) late time values of $s_M(t)$ are virtually identical to $s_{ap}(t)$ because $s_R(t)$ tends to zero (recall Figure 2.2). Because of this last remark, $s_M(t)$ should not be used for recovery times longer than that at which $s_R(t)$ tends to zero.

2.2.4 Variable pumping rate

We generalize here Agarwal, Theis and other methods to acknowledge time-dependent pumping rate during the interpretation of recovery data. Time variability of pumping rate has been addressed by numerous authors, including Agarwal et al. (1980). The goal has been typically to interpret pumping test data and the method consists of using either superposition (Birsoy and Summers, 1980; van der Kamp, 1989; Neville and van der Kamp, 2012) or deconvolution (von Schroeter et al., 2002). Given the difficulties of the latter, and the specificities of recovery test analysis, we adopt an approach similar to that of Birsoy and Summers (1980), but taking advantage of the fact that the last portion of the pumping phase is often performed at a constant rate. Therefore, we assume that the pumping rate fluctuates only up to time t_{cQ} (Figure 2.1). Thereafter, the pumping rate is constant (Q_c). We decompose the pumping rate as the sum of Q_c, which lasts over the whole pumping interval, and a variable pumping rate $Q'(t)$:

$$Q(t) = Q_c + Q'(t), \tag{2.7}$$

where we assume that Q' becomes zero after time t_{cQ}. Using superposition again, we write the total drawdown as $s(t) = s_c(t) + s'(t)$, where $s_c(t)$ and $s'(t)$ are the drawdowns caused by Q_c and $Q'(t)$, respectively. Assuming that $t \gg t_c$, so that steady radial regime has been established near the pumping well, $s'(t)$ can be calculated as the sum of the residual drawdowns produced

by infinitesimal (or discrete, in the case of step tests) pumping rate steps, dQ', from the beginning of the step (at time τ) until the end (at time t_{cQ}):

$$s'(t) = \int_0^{t_{cQ}} \frac{1}{4\pi T} \frac{dQ'}{d\tau} ln\left(\frac{t-\tau}{t-t_c}\right) d\tau = \frac{Q_c}{4\pi T} ln(E_I), \tag{2.8}$$

$$s(t) = \frac{Q_c}{4\pi T} ln\left(\frac{2.25TtE_I(t)}{r^2S}\right), \tag{2.9}$$

where E_I is implicitly defined in (8a) as:

$$E_I(t) = exp\left[\int_0^{t_{cQ}} \frac{1}{Q_c} \frac{dQ'}{d\tau} ln\left(\frac{t-\tau}{t-t_{cQ}}\right) d\tau\right] \tag{2.10}$$

We illustrate the use of Equation (2.10) by application to a step drawdown test with $Q(t) = Q_i, t_i \leq t < t_{(i+1)}, i = 1, N$, where N is the number of steps, and $t_N = t_{cQ}$ (pumping rate is Q_c during the last step), then $dQ' \setminus d\tau = \sum_{i=1}^{N}(Q_i - Q_{i-1})\delta(t_i - \tau)$, with $Q_0 = Q_N = Q_c$ (Figure 2.2). With these definitions,

$$E_I(t) = \prod_{i=1}^{N-1} \left(\frac{t-t_i}{t-t_{cQ}}\right)^{\frac{\Delta Q_i}{Q_c}}, \tag{2.11}$$

where $\Delta Q_i = Q_i - Q_{i-1}$. This equation is similar to those of Birsoy and Summers (1980) and Agarwal et al. (1980), except that they add each step independently. In the case of Birsoy and Summers (1980), their choice made sense because they were seeking an approximation of drawdown during pumping, but it is somewhat less accurate if Q' is indeed small and zero after t_{cQ}.

Mishra et al. (2013) argued that step approximations may not be appropriate for smoothly varying flow rates and proposed a Laplace transform solution for time-wise linear flow rate. Equation 2.10 can also be easily integrated in this case. Assume that the pumping rate varies linearly between point measurements, $Q(t_i) = Q_i$, $i = 1, N$, with possible jumps at $t_1[\Delta Q_1 =$

$Q_1 - Q_c]$ and $t_N = t_{cQ}[\Delta Q_{N+1} = Q_c - Q_N]$, when E_I becomes (again easy but tedious integration)

$$E_I(t) = \left(\frac{t-t_1}{t-t_{cQ}}\right)^{\Delta Q_1/Q_c} \left(\frac{t-t_N}{t-t_{cQ}}\right)^{\Delta Q_{N+1}/Q_c} \prod_{i=2}^{N} \left(\frac{t-t_{i-1}}{e(t-t_{cQ})}\right)^{\Delta Q_i)/Q_c} \left(\frac{t-t_{i-1}}{t-t_i}\right)^{m_i(t-t_i)/Q_c}, \tag{2.12}$$

where $e = 2.718$ is the Euler's number. Using either equation (2.11) or (2.12) in (3.17) leads to an "equivalent time", $tE_I(t)$, for all approximations of drawdowns caused by pumping (but not by recovery). Therefore, using (3.16) for $s(t)$ and $s(t_p)$ in equation (3.9) yields

$$s_{Ac}(t) = s(t_p) - s_R(t) = \frac{Q_c}{4\pi T} \cdot ln\left[\frac{2.25T}{r^2S}\frac{t_p(t-t_p)E_I(t_p)}{tE_I(t)}\right] \tag{2.13}$$

which suggests a modified Agarwal time:

$$\hat{t}_A = \frac{t_p(t-t_p)E_I(t_p)}{tE_I(t)} \tag{2.14}$$

With the new corrected time $\hat{t}_A$, it becomes feasible to interpret recovery test data, as the mark left by the past pumping history over the recovery signal has been taken into consideration. Obviously, this equivalent time should be used also to correct Theis recovery time (t_R) or, for the proposed alternative (Section 2.2.3), the recovery time $(t_r = t - t_p)$. The modified times would result in

$$\hat{t}_R = \frac{tE_I(t_p)}{t-t_p} \qquad and \qquad \hat{t}_r = \frac{(t-t_p)E_I(t_p)}{E_I(t)} \tag{2.15}$$

It is important to underline that the application of the proposed method (s_M) jointly with an equivalent time $(\hat{t}_r)$ would allow interpreting hydraulic tests characterized by a short pumping period and variable pumping rate. This algorithm has been implemented in a spreadsheet available from the GHS-UPC software web page at https://h2ogeo.upc.edu/en/investigation-hydrogeology/software.

2.3 Performance of recovery test interpretation methods

2.3.1 Ideal conditions: importance of the duration of pumping

As discussed in Section 2.2.2, Agarwal's method requires that the pumping period has been long enough to reach linear behavior in semi logarithmic scale. Thus, we test here how the pumping time t_{pD} can affect the interpretation of recovery data for both Agarwal's and the proposed method (Figure 2.4). To this end, we compare the ideal pumping solution (Theis) with the corresponding diagnostic plot determined by (1) the Agarwal's drawdown curve, i.e., the plot of s_A versus t_A obtained from the recovery test data, and (2) the method proposed in section 2.2.3. The aim is to evaluate the effect of pumping and recovery duration on the recovery test interpretation, performed with both Agarwal's and the new proposed method, thus analyzing the validity of both.

The pumping durations t_p are chosen in terms of the characteristic time t_c of the observation well because pumping tests are usually designed bearing in mind that a sizable response should start at 0.1 t_c (i.e., pumping time $t_{pD} = 0.1$, recall that $t_c = r^2 S \setminus T$) and CJ's slope starts developing at $t_c(t_{pD} = 1)$. In well hydraulics, $u = 1 \setminus 4t_D$ is oftne used instead of t_D, and the validity of CJ's approximation is usually restricted to $u < 0.03$ (i.e., $t_{pD} > 8$). Therefore, we have chosen three different pumping times ($t_{pD} = 0.5, 1, 10$). The recovery time $t_{rD} = t_D - t_{pD}$ has been fixed to be four times the pumping time period $t_{rD} = 4t_{pD}$.

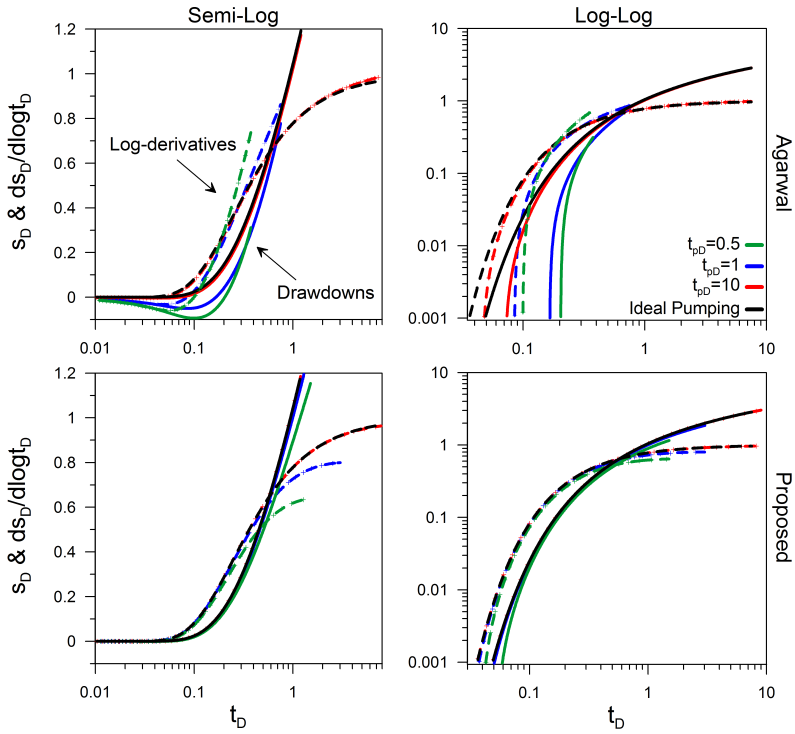

Figure 2.4: Diagnostic plots representing recovery test interpretation in an ideal Theis aquifer for three different pumping durations using Agarwal's recovery method (above) and the proposed method (below). The ideal pumping test solution (Theis) is shown as reference.

Figure 2.4 displays two different patterns in the application of Agarwal's method. First, the longer the producing period, the better the whole curves fit Theis' solution, approaching a perfect match when $t_{pD} = 10$. In fact, late time drawdowns do not reach a quasi-steady-state behavior (constant log-derivative), unless a long producing period is applied. Second, the match of Agarwal curves to the ideal pumping solution improves with recovery time. Agarwal solution is poor for early times. In fact, when pumping is short, Agarwal yields negative drawdowns and negative log-derivatives at early times. Both observations are consistent with the discussion of Section 2.2.2.

The proposed method also improves with the producing period duration.

However, the types of errors are complementary to those of Agarwal. On the one hand, the fit to the ideal Theis solution worsens for long recovery times, reaching a fictitious quasi-steady state behavior, which reflects the log-derivative at the end of the pumping period, which is different from the real one of the aquifer system. On the other hand, early times data perfectly match the ideal solution.

The accuracy of these methods can be further analyzed by estimating the absolute relative error of both the drawdown and its log-derivative, defined as

$$\epsilon_s = \left| \frac{s_{pump}(t) - s_{rec}(t_{corr})}{s_{pump}(t)} \right| \quad \epsilon_m = \left| \frac{m_{pump}(t) - m_{rec}(t_{corr})}{m_{pump}(t)} \right|, \tag{2.16}$$

$$0 < t = t_{corr} < t_p,$$

where s_{pump} and m_{pump} are respectively the theoretical drawdown curve and its log-derivative associated with the Theis' solution, s_{rec} and m_{rec} are the corresponding corrected recovery values used in the interpretation, i.e. $s_{rec} = s_A$ for the Agarwal's method and $s_{rec} = s_M$ for the proposed interpretation method, and t_{corr} is the corrected time determined as t_A and t_r depending on the interpretation method. It is important to underline that, assuming proportionality between estimated transmissivity and drawdown log-derivative values (long pumping times), the relative error ϵ_m expresses that the estimated transmissivity value T_{est} differs from the exact value T by a factor given by $T_{est} = T(1 - \epsilon_m)^{-1}$.

The absolute value of the relative errors is shown in Figure 2.5, which displays in a log-log plot their recovery time evolution for three pumping durations. Figure 2.5 makes it clear that (1) the longer the producing time, the smaller the errors associated with both methods; (2) the errors of Agarwal's method for the drawdown and its log-derivative decay with recovery time

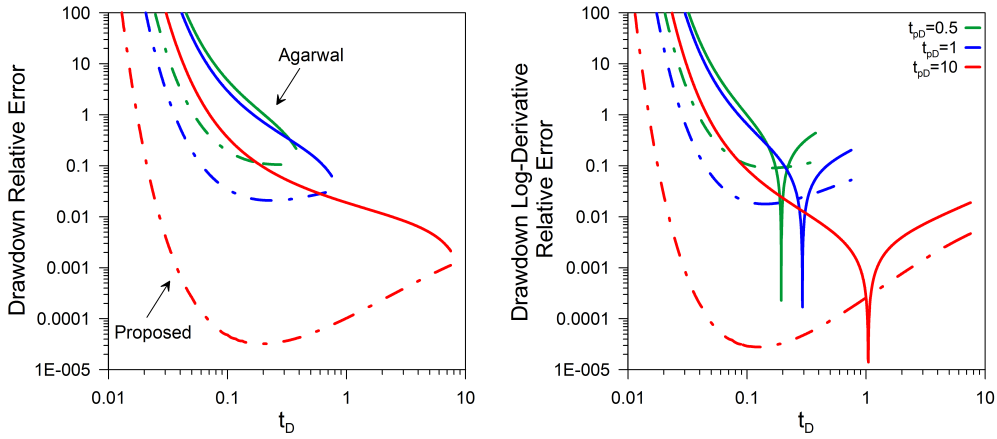

Figure 2.5: Relative errors of drawdowns and log-derivatives resulting from both Agarwal's (Line) and the proposed method (Dash Dot) under ideal conditions for three different pumping durations. Note that the errors of the proposed method are below those of Agarwal for any given pumping duration and that both methods improve with increasing pumping duration.

(which is consistent with equation 2.4), although errors in log-derivative tend to increase at late time; (3) the errors of the proposed method are smaller than those of Agarwal's method at any given time t_D. This effect is dramatically important when t_r is small, at early recovery times. Here, more than one order of magnitude difference is noted; (4) the errors of the proposed method rapidly decay initially (up to $t_D \sim 0.1 - 0.2$), but tend to increase slightly thereafter.

We finally acknowledge that the advantages given by the proposed method must be taken with care as the accuracy of the proposed method relies on how $s_{ap}(t)$ is selected in equation (2.6). In this context, we content that this conceptual decision will be only important at late times but not at early times where the performance of the method is best.

At this stage, it is worth mentioning here that the errors presented in Figure 2.5 are always positive, i.e., Agarwal's method underestimates the drawdown and its log-derivative, except for late recovery times (after the singularity where error values approach zero). In this region, the relative error of the drawdown log-derivative given by Agarwal's method becomes negative. Importantly, the interpretation of the late-time recovery data with Agarwal's method will underestimate the transmissivity of an aquifer.

2.3.2 Non-ideal conditions: effects of boundaries and flow dimension

Aside from long pumping times, others assumptions were required for the development of Agarwal's method, as the aquifer is assumed to be large, homogeneous, confined and characterized by radial flow. Thus, we analyze here the effect of departures from these assumptions: (1) presence of a no-flow boundary given by an impermeable barrier defined by $r'^2/r^2 = 100$, where r' is the radial distance from the image well (image well theory) to the observation well, (2) a constant head boundary (constant head defined by the same characteristic time as for the no-flow boundary condition), (3) a leaky aquifer characterized by the dimensionless number $B_D = B \setminus r$, where B is the leakage factor, and r is the distance from the pumping well to the observation well, and (4) a drainage line (flow dimension of one to test the impact of varying the flow dimension).

We compare the analytical solutions to these problems with the corresponding diagnostic plots determined by the Agarwal's drawdown curve (Figure 2.6, top rows) and those determined by the application of the proposed method (Figure 2.6, bottom rows). Still, the aim is to investigate the validity of the methods under non-ideal conditions. Three different simulations have been carried out for each scenario with pumping times $t_{pD} = 1, 10, 100$. The recovery time has been fixed to $t_{rD} = 4t_{pD}$. It is important to underline that, compared to the previous analysis, we have now adopted longer pumping times t_{pD} to ensure that boundary effects can be observed.

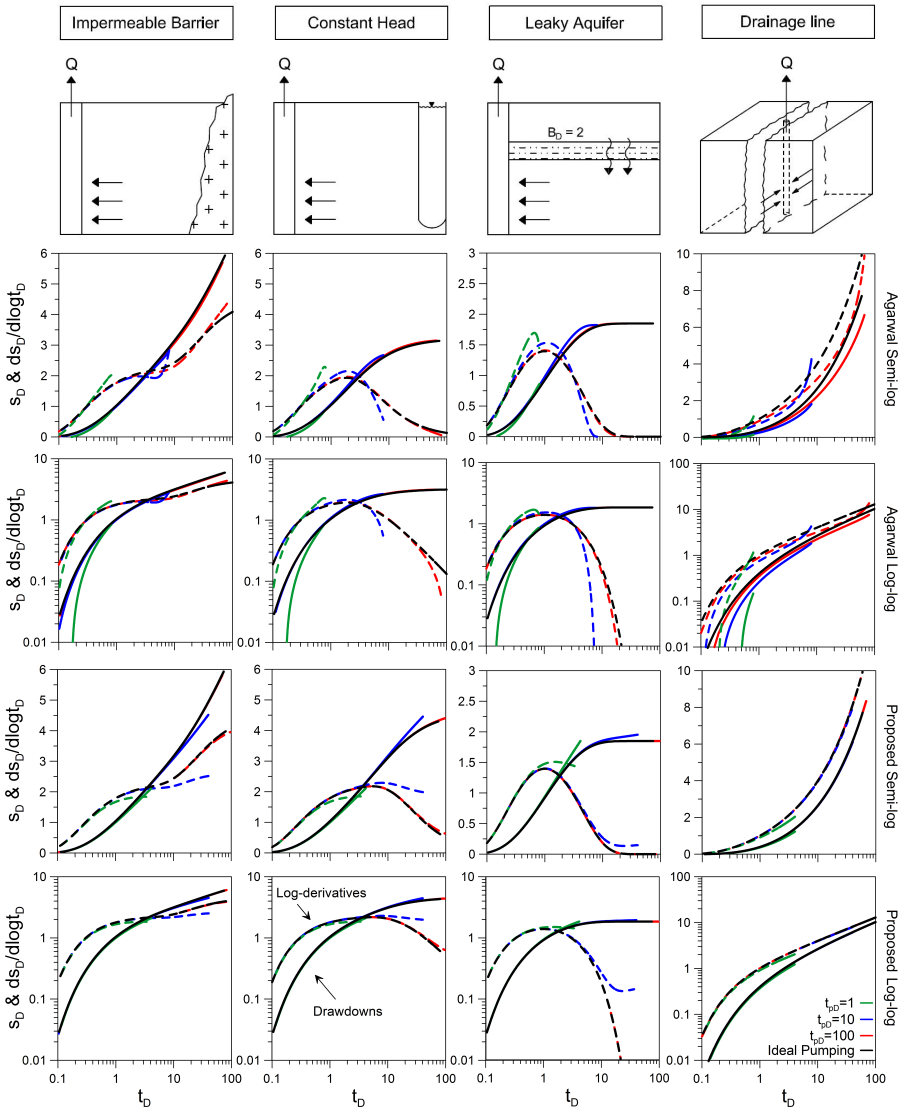

Figure 2.6: Diagnostic plots representing recovery test interpretation under non-ideal conditions. Three different pumping times have been analyzed applying both Agarwal (top two rows) and the proposed method (bottom two rows). The analytical solution for pumping is shown as a reference.

As can be seen in the graphs, the performance of Agarwal's method for the one dimensional flow is different than for other boundary effects. In fact,

in the latter case it is possible to find the same pattern as that found for ideal conditions: the longer the producing period, the better the whole curves fit the analytical solution. In particular, early times present important mismatches for short producing periods and late times (late recovery times) do not clearly reproduce the ideal pumping curve.

However, in the one dimensional flow system solution, the curves fail to match the analytical solution for either short or long producing periods. The proposed method works very well in matching the analytical solution for early times, even considering short producing periods. However, its performance for late recovery time data, depends on the duration of pumping. Finally, the recovery test interpretation carried out for one dimensional flow perfectly resembles the analytical solution.

2.3.3 Non-ideal conditions: variable pumping rate

Until now, the validity of recovery test methods has been analyzed for constant pumping rate. However, as discussed in the introduction, this condition is often difficult to meet (in fact, it is this difficulty what motivates our emphasis in recovery analysis in the first place). We discuss here the effect of time-dependent pumping rate (see Figure 2.1) for ideal (Theis) aquifer conditions.

We have chosen a cubic law variable flow rate term Q' (recall equation 3.15), written as:

$$Q'(t) = Q'_{max} - Q'_{max}\left[\frac{3}{2}\left(\frac{t}{t_{cQ}}\right) - \frac{1}{2}\left(\frac{t}{t_{cQ}}\right)^3\right], \qquad 0 < t \leq t_{cQ}, \tag{2.17}$$

$$Q'(t) = 0, \qquad t_{cQ} < t \leq t_p, \tag{2.18}$$

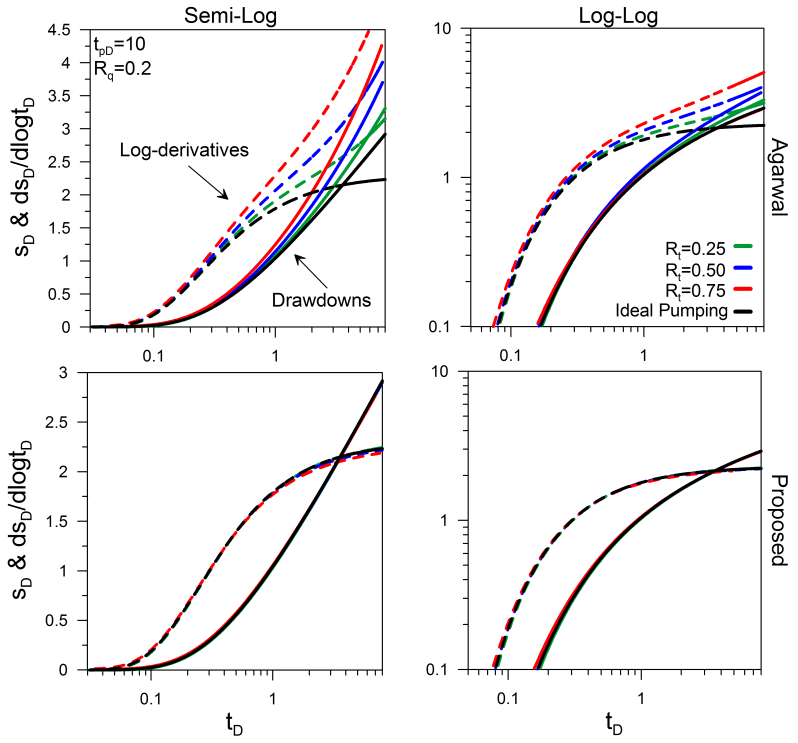

Figure 2.7: Diagnostic plots obtained from recovery data after pumping an ideal Theis aquifer at a variable rate (total pumping duration, $t_{pD} = 10$, and ratio between constant and maximum pumping rate deviation, $R_q = 0.2$). Three different values of R_t (ratio of variable rate to total pumping time) have been analyzed. The plots have been obtained both assuming constant pumping rate (above) and acknowledging its variability by means of equation 3.16 (below).

where Q'_{max} is the maximum value of $Q'(t)$, which occurs at $t = 0$, t_{cQ} is the time at which $Q'(t)$ becomes equal to zero and depends on the parameter R_t as $t_{cQ} = R_t t_p$. In addition, the constant pumping rate Q_c is proportional to Q'_{max} by a constant $R_q = Q_c \setminus Q'_{max}$. Fixing the pumping time $t_p = 10t_c$ and the recovery time $t_r = 4t_p$, multiple simulations have been run, considering different couples of R_t,R_q values. In this case, the aim is that of testing Agarwal's method, using both Agarwal's time (Section 2.2.1) and the modified one (Section 2.2.4).

In order to compare different solutions, the drawdown produced by an equivalent pumping rate (constant rate, pumping the same water volume pumped during the hydraulic test in the same time period) has been calculated. Hereafter, it is referred to as the ideal pumping solution.

As in the previous two sections, diagnostic plots are compared in terms of dimensionless variables. For the comparison, we keep constant the dimensionless duration, t_{pD}, and the magnitude of the pumping rate variability, R_q, while changing the period over which pumping rate is variable, as measured by R_t. As shown in Figure 2.7, the longer the duration of pumping rate variation (high R_t), the worse Agarwal's solution reproduces that of an ideal pumping drawdown. The interpretation of the same hydraulic test through the adoption of the equivalent time (Eq. 13) leads to a correct reproduction of the ideal solution. In short, if the pumping rate is variable, the variability must be acknowledged for the interpretation of recovery data.

2.4 Application to real-world data sets

The proposed method is used to interpret two cross-hole hydraulic tests performed at the Grimsel underground laboratory in Switzerland (FEBEX tunnel). The site description as well as the hydraulic test performance and interpretation have been presented by Martinez-Landa and Carrera (2005, 2006). We have chosen these tests to illustrate the performance, strengths and weaknesses of the methods.

2.4.1 Example A: Long pumping test and fast aquifer response

This test corresponds to the water injection at point I2-1 and head measurements obtained at point F22-3, described by Martinez-Landa and Carrera (2006). The observation point is located 2.86 m away from the injection point and recorded drawdowns are produced by a constant pumping rate of 418.2 m3/d for a pumping period $t_p = 4.63$ days and a recovery period $t_r = 0.6t_p$. The

quasi-steady state has been reached during pumping, which can be seen qualitatively in figure 2.8, and confirmed quantitatively by the characteristic time of the observation point ($t_c = 0.22$ days, obtained from the transmissivity and storativity resulting from interpretation of the drawdown curve, or a dimensionless pumping time $t_{pD} = 21.47$). Under these conditions, both Agarwal and the proposed method (Section 2.2.3) should work given our previous discussion.

Figure 2.8A shows the resulting diagnostic plots, while the estimated hydraulic properties obtained during the recovery and the pumping period are reported in Table 1 (Example A). The diagnostic plot shows three data sets: the drawdown produced during the actual pumping and the recovery data plotted as drawdown estimated by both Agarwal and the proposed method. As expected, both methods lead to good results: the curves present an almost perfect match with the actually measured drawdown data. Consequently, the same conceptual model can be inferred. Moreover, similar results have been achieved in terms of estimated hydraulic properties, as both transmissivity and storage coefficient values present quite insignificant differences compared to those obtained with the drawdown data.

2.4.2 Example B: Short pumping test and high delay in aquifer response

In this second example, we interpret the cross-hole test resulting from injecting water at Fbx2-04 and observing head levels at point F13-2 (Martinez-Landa and Carrera, 2005). The observation point is located 10.72 m away from the injection point and recorded drawdowns are produced by a constant flow rate of 496.8 m^3/d. As can be seen in figure 2.8, the quasi steady-state has not been reached, due to a unexpected shut down of the pump that resulted in a pumping time t_p = 0.4 days and a long recovery time t_r = 3.7 t_p (data presented by Martinez-Landa and Carrera correspond to the full test). Remarkably, the residual drawdown clearly shows a high delay of the aquifer response as drawdown keeps increasing for a while after pumping shut down.

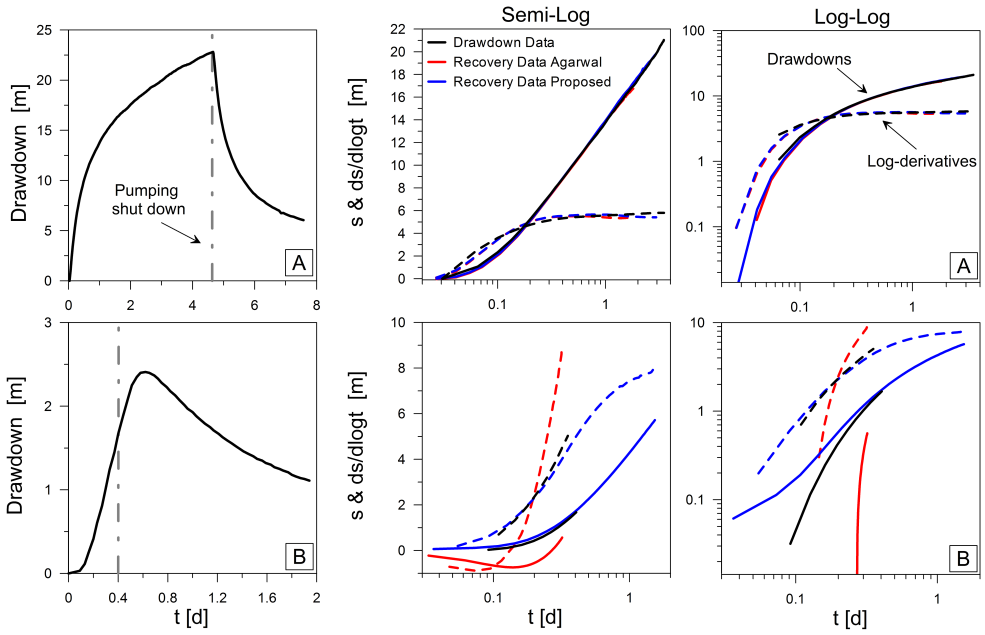

Figure 2.8: On the left side, the drawdown data related to two different hydraulic test performances (Example A, above and example B, below) have been plotted. On the right side, the diagnostic plots of the drawdown curves (Black line), as well as of data resulting from the application of both Agarwal (Red line) and the proposed method (Blue line) have been presented.

Both behaviors should be expected because of the long characteristic time of the observation point t_c = 3.03 days (value obtained from the interpretation of the drawdown curve proceeding from a long pumping period). It results in a dimensionless pumping time t_{pD} = 0.13, far from t_{pD}= 1 needed to get the whole transient response and clearly far from reaching quasi-state conditions.

Given the circumstances, Agarwal and the proposed method (Section 2.2.3) lead to different results. As expected, Agarwal performs very poorly. In fact, the recovery is so slow that the residual drawdown was larger than the drawdown at the end of pumping for a long time, so that Agarwal drawdowns remained negative for a good portion of the recovery. Application of the proposed method led to a constant late time slope that was larger than

Table 2.1: Hydraulic properties estimates applying the method to real-world data sets.

Test	Drawdown log derivative (m)	Transmissivity (m^2/day)	Jacob time (day)	Storage coeff. (-)
Example A				
Drawdown data	5.808	$6.632 \cdot 10^{-5}$	0.096	$1.745 \cdot 10^{-6}$
Agarwal	5.410	$7.120 \cdot 10^{-5}$	0.079	$1.540 \cdot 10^{-6}$
Proposed	5.277	$7.299 \cdot 10^{-5}$	0.067	$1.356 \cdot 10^{-6}$
Example B				
Drawdown data	5.033	$9.091 \cdot 10^{-5}$	1.348	$2.401 \cdot 10^{-6}$
Agarwal	3.780	$1.210 \cdot 10^{-4}$	0.267	$6.332 \cdot 10^{-7}$
Proposed	3.214	$1.650 \cdot 10^{-4}$	0.265	$7.381 \cdot 10^{-7}$

Note. The estimated hydraulic parameters applying both Agarwal and the proposed method are presented and compared with those one estimated using drawdown data obtained from long pumping tests. Example A refers to the hydraulic test with long pumping period while example B refers to the one with short pumping period.

the one at the end of pumping. While this is not surprising, given the short duration of pumping, it shows that recovery data contains information representative of a period that may be longer than that of pumping. Therefore, we followed an iterative process: the slope m, used to estimate $s_{ap}(t)$, has been iteratively replaced by the slope calculated using the last values of s_M. Throughout the iterations, the m value tends to a constant that has been used for the last estimation of s_M.

Figure 2.8B shows the resulting diagnostic plots. The corresponding estimated hydraulic properties are reported in table 1 (Example B), together with those estimated from the drawdown data that refers to a long pumping test performed after the unintentional switching off. It is clear that Agarwal's data do not reproduce the actual drawdown data. Instead, the proposed method results in a positive drawdown that matches quite well drawdown data. The log-derivative is positive and fits well the actual pumping test log-derivative at early times, but diverge at late times, until reaching a fictitious quasi-steady state regime, which turns out to be close to the one obtained from the long test described by Martinez-Landa and Carrera (2005). That means that we can

adequately reproduce the aquifer response and therefore infer a proper conceptual model. In terms of hydraulic properties estimation, the difference is not as relevant as the information that one can obtained from the diagnostic plot.

2.5 Discussion and Conclusions

We have analyzed Agarwal's method validity under ideal and non-ideal conditions, generalizing it for time-dependent pumping rate and proposing an alternative method for recovery test interpretation to be applied especially under non-ideal conditions. Our results can be summarized as it follows:

1. Residual drawdowns contain as much information as pumping test data, which is qualitative and quantitatively valuable. Moreover, they are much less influenced by pumping perturbations, resulting in a much gentler and complete time series to be interpreted. Therefore, the analysis of recovery data must be considered as a great choice for the characterization of aquifer systems through hydraulic testing. The only drawback of recovery data is their sensitivity to environmental head fluctuations (especially at observation points, where the head signal induced by pumping may be small, and at late times, when environmental fluctuations may be larger than the residual drawdown). Therefore, emphasis must be placed during test design which should consider a long observation period both prior and, especially, after the pumping period to facilitate filtering of environmental head fluctuations to obtain residual drawdowns.

2. The Agarwal's method should be considered as a very effective method for recovery data interpretation because it is simple and may yield drawdown curves virtually identical to those obtained during pumping with constant rate, thus facilitating the use of diagnostic plots for quantitative and qualitative analysis. This is true under ideal conditions of radial flow (including boundary effects), provided that the dimensionless

pumping time is long enough to develop the fully radial regime as ascertained by a constant CJ (semi-log plot) slope (log-derivative).

3. The Agarwal method fails to reproduce the pumping drawdown curves in an appropriate way when the duration of pumping is so short that the constant slope has not started to develop (i.e., when the dimensionless time $Tt \setminus Sr^2$, is less than 1). In practice, this restricts the applicability of the method to the pumping well, for which it was originally developed, unless the duration of pumping is very long or the aquifer is confined.

4. The Agarwal method may also fail for non-radial flow (i.e., when the late time slope is non-constant). We tested the method for a flow dimension of one, and the method did not work even for long producing periods.

5. We proposed an alternative method (equation 2.6) to overcome Agarwal's limitations that works very well both under ideal and non-ideal conditions, especially during early time recovery. The main limitation of the proposed method, when compared to Agarwal's, is that its duration is artificially unlimited (Agarwal time will never be longer than the pumping time). This implies that our late time drawdowns may suggest a quasi-steady-state regime that is fictitious, as it reflects the assumption made in approximating drawdowns during recovery. Surprisingly, the method performed quite well during application to a real case where the dimensionless pumping duration had been very short, which suggests that the proposed method may be valid for recovery times beyond the pumping duration.

6. The previous discussion suggests that a possibility would be to blend both methods (i.e., use the proposed method for early time recovery and Agarwal's for late time). This possibility has not been fully explored for two reasons. First, the proposed method tends to work better than Agarwal for the short dimensionless pumping duration typical of observation wells, which are frequent in hydrology (as opposed to petroleum

engineering) and where we discourage the use of Agarwal method. Second, the primary use of the methods we are discussing here is for drawing diagnostic plots, which help in defining the conceptual model. Once this has been identified, quantitative interpretation can be best achieved through numerical modeling of the full test (pumping and recovery), while acknowledging the variability of pumping rates, so that whether radial flow regime has been reached becomes irrelevant.

7. We proposed an alternative "equivalent time" to treat recovery data from variable pumping rate (both step-wise and piece-wise linear) that allows accounting for the influence of pumping rate variability during recovery data interpretation using our proposed method or Agarwal's. The test example (Figure 2.7) makes it clear that acknowledging for the time variability of pumping rate is critical. Therefore, pumping rate must be monitored carefully. This is also important for Theis' recovery method, which remains the method of choice for the estimation of transmissivity from late time data.

Chapter 3

Automatic calibration of groundwater models with bias correction and data filtering: Working with drawdown data

This chapter is an edited version of: Trabucchi, M., Fernàndez-Garcia, D., & Carrera, J. (2021). Automatic calibration of groundwater models with bias correction and data filtering: Working with drawdown data. *Water Resources Research*, 57, e2020WR028097. https://doi.org/10.1029/2020WR028097 (Appendix B)

3.1 Introduction

Hydraulic tests are typically used to characterize aquifers by analysing the aquifer response to a known imposed stress. The term test is used here in a broad sense, including any perturbation to the normal functioning of the aquifer, such as pumping tests, stream-stage tests, or in general known water production periods. In any of these cases, the aquifer response to pumping or other hydraulic perturbations contains valuable information about the conceptual model and hydraulic properties (e.g., Freeze and Cherry, 1979; Domenico et al., 1998; Renard, 2006; Gringarten et al., 2008; Trabucchi et al., 2018). The response must be not only properly measured, but also processed and interpreted to extract such information. The procedure usually involves fitting water level changes or drawdown to a mathematical model.

The definition of drawdown is well-known, simple and intuitive, but we want to briefly recall it to argue why modeling drawdowns, rather than heads, in the context of transient model calibration may be the best choice for aquifer test interpretation. Drawdown is defined as the difference between two heads: $s = h_n - h$, where h is the actually observed head resulting from the hydraulic test, and h_n is the natural head evolution (i.e., the head that would have been measured if the hydraulic test had not been performed). As a result, as we will show later, drawdown models enjoy homogeneous initial and boundary conditions (i.e., boundary and initial drawdowns are zero and boundary and internal sink/source terms are zero). This is advantageous because it avoids the problem of defining initial and boundary conditions during groundwater modeling (Renard, 2006). Only the stress that causes the drawdown, which should be well known, needs to be specified. At the same time, it allows one to avoid working with absolute heads, which are characterized by weak dependence on hydraulic properties and represent the solution to a differential equation with complex boundary and initial conditions (Renard, 2006). The downside of working with drawdowns lies on the fact that they do not inform directly about the functioning of the aquifer (i.e., where water comes from or where does it flow to), but only about changes induced

by their driving stress. These changes are most informative about transmissivity and storativity in the aquifer, whereas the overall aquifer functioning is controlled by recharge and boundary fluxes and heads, which control natural heads.

However, hydrogeologist often lack direct access to accurate drawdown data. Errors in head measurements and the inherent uncertainty associated with the natural head evolution of the system prevents an adequate estimation of drawdowns. Typical errors in head measurements (h) are those that propagate from inaccurate information on elevation data (datum), sampling procedure or measurement tools (Post and von Asmuth, 2013). These errors generally vary in space and can substantially affect the precision and interpretation of drawdown data and hydraulic gradients (Silliman and Mantz, 2000; Devlin and McElwee, 2007; Rau et al., 2019), increasing the uncertainty in hydraulic properties and the estimation of hydrogeological processes (Sweet et al., 1990). Since these errors are usually hard to recognize, making corrections is always a difficult task (Post and von Asmuth, 2013).

Actually, one of the reasons for working with drawdowns is that constant-in-time head errors are filtered away. The problem arises because error may also be transient. Transient errors may result from unknown external stresses, which typically affect natural heads (h_n), leading to hard-to-predict trends. Taking into account these external effects always deserves special attention during the analysis of hydraulic test data since the determination of the aquifer parameters should be based only on drawdown data derived from the hydraulic test. Actually, it is in this context of aquifer-test analysis that the concept of decomposing water levels into natural heads caused by external forces and drawdowns was initially developed. For short hydraulic tests and relatively large drawdowns, these transient external forces are usually negligible and h_n can be considered constant (typically equal to the initial head). But a de-trending time series analysis is usually required for long-term responses, or even for short term pumping tests when the magnitude of drawdown is comparable to natural head fluctuations (e.g., at distant observation wells),

(Halford, 2006; Maliva, 2016).

Fluctuations affecting h_n can be classified as monotonic (e.g., long term trend), rhythmic (e.g., earth and sea tides), non-rhythmic (e.g., response to far away pumping), and singular (e.g., recharge event) (Kruseman and de Ridder, 1990; Halford, 2006). Several filtering methods have been developed to remove rhythmic fluctuations from hydraulic head data (Halford, 2006; Halford et al., 2012; Garcia et al., 2013; Zhang et al., 2014; Calvache et al., 2016, among others). However, there are still not well-developed and consolidated methodologies to treat other fluctuations. In simple systems, h_n is typically estimated by fitting the head data measured prior to the hydraulic test to a linear or exponential function of time (Ferris et al., 1962; Maliva, 2016). Other methods estimate the temporal evolution of h_n by correlating h_n with the water level measured at a distant piezometer, by means of regression, provided that sufficient long pre- and post-test data is available (Kruseman and de Ridder, 1990), kriging (Gómez-Hernánez et al., 1997a; Alcolea et al., 2007) or neural networks (Coppola Jr. et al., 2005).

A more complete analysis can be carried out for de-trending purposes following **?**. In this case, the natural head solution is calculated as a linear combination of several time series (e.g., barometric pressure, tidal potential, recharge, external pumping), which are selected by a trial and error procedure aimed at minimizing the differences between h and h_n measured prior to the hydraulic test itself. Nevertheless, these de-trending approaches are quite laborious in complex systems and do not allow estimating natural heads for long time periods. In this case, one is usually forced to characterize the aquifer by developing a numerical groundwater model with head measurements h as observation data in the calibration procedure. This approach avoids most of the filtering problems but not those derived from systematic head measurement errors. Moreover, it requires to have an already good conceptual model of the system with detailed knowledge of the past aquifer stresses.

In this context, we propose a method for data filtering and aquifer characterization capable to: (i) filter the natural trend of hydraulic heads caused by

external stresses that can otherwise mask the aquifer test response and complicate modeling efforts (estimate head changes or drawdown); (ii) correct errors derived from field measurements as well as model discrepancies or inadequacies; and (iii) automatically estimate hydraulic parameters through the solution of the inverse problem with drawdown response data. We apply all these concept for transient model calibration. The chapter is organized as it follows. In section 3.3, we present the problem and the methodology. Then, we apply the method to a heterogeneous synthetic aquifer and analyze the results in sections 3.4 and 3.5, where we also discuss some important aspects by comparing the method with traditional approaches. Finally, we highlight the most relevant conclusions in section 5.4.

3.2 Background: Formal definition of drawdown

As mentioned in the introduction, we define drawdown as the difference between "natural heads", h_n (i.e., those that would have occurred if no pumping test had been performed) and actual heads, h (i.e., those that have actually occurred in response to the pumping test and all other driving forces). Natural heads obey the flow equation,

$$S\frac{\partial h_n}{\partial t} = \nabla \cdot (\mathbf{T}\nabla h_n) + w, \qquad \forall t > t_0 \quad \mathbf{x} \in \Omega, \tag{3.1}$$

subject to initial and boundary conditions

$$h_n = h_0, \quad t = t_0 \qquad \forall \mathbf{x} \in \Omega, \tag{3.2}$$

$$\mathbf{T}\nabla h_n \mathbf{n} = \alpha(h_e - h_n) + q_e, \qquad \forall t > t_0 \quad \mathbf{x} \in \Gamma, \tag{3.3}$$

where Ω is the flow domain and Γ its boundary, $\mathbf{n}$ is the unit normal vector, T is transmissivity, S is storage coefficient, w is the internal sink-source term (e.g., recharge), h_0 is the initial head, and h_e and q_e are the "external" heads

and fluxes at the boundaries, respectively. The latter (h_e and q_e), as well as the sink/source term w can vary over time. α controls the type of boundary condition (α equals zero at prescribed flow portions of Γ, α equals ∞ at prescribed head portions, and, else, α is the leakage factor at mixed boundary condition portions of Γ).

Actual heads after pumping start, h, obey the same equation, except for the sink term due to pumping, that is

$$S\frac{\partial h}{\partial t} = \nabla \cdot (\mathbf{T}\nabla h) + w - \delta(\mathbf{x}_P)Q, \tag{3.4}$$

where Q is the pumping rate at $\mathbf{x}_P$ and δ is Dirac's delta. We assume that the test starts at t_i ($t_i > t_0$), so that Q is zero before t_i. This equation is subject to the same initial (3.2) and boundary (3.3) conditions as equation 3.1.

We define drawdown as

$$s = h_n - h, \tag{3.5}$$

The equation governing s is obtained by simply subtracting equation 3.4 from 3.1, which yields

$$S\frac{\partial s}{\partial t} = \nabla \cdot (T\nabla s) + \delta(\mathbf{x}_P)Q, \tag{3.6}$$

The initial and boundary conditions are obtained as (3.2) and (3.3) minus their h counterparts, which we have not rewritten because they were identical. Therefore, the initial and boundary conditions of s are simply written as,

$$s = 0, \quad t = t_i, \tag{3.7}$$

$$\mathbf{T}\nabla s\mathbf{n} = -\alpha s. \tag{3.8}$$

Note that this definition requires the equation to be linear and time dependence of boundary conditions and internal sink-sources to be known. The advantage of defining drawdowns according to (3.5) is that all flow terms and external heads have vanished in equations 3.6-3.8. That is, the drawdown model is identical to that of natural heads, but setting to zero all source terms, and boundary heads and fluxes. Only the type of boundary conditions, as specified by α, and the hydraulic test driving force (Q in 3.6) need to be kept. Note, also, that this definition allows one to relax the traditional requirements of pumping tests. That is, the aquifer does not need to be of infinite extent or be at steady-state conditions, etc. Obviously, the only problem is that this definition is based on an un-observable quantity, h_n. The problem is addressed in section 3.3 below.

3.3 Problem statement and methodology

3.3.1 Bias correction

Let us consider the interpretation of a hydraulic test, the head response of which is affected by strong external effects that prevent a clear estimation of the change in hydraulic head produced only by the aquifer test. The aquifer test starts at time $t = t_i$. Hydraulic head evolution is recorded at several observation points before and during the test. We wish to filter head data to obtain drawdowns, i.e., the aquifer response to the aquifer test at the observation points, and use the resulting filtered data to calibrate a groundwater model. In the following, we will show that these two processes (filtering and calibration) are not independent from one another and should therefore be treated jointly.

Let us start by defining the time series of drawdown data from equation 3.5 as the change in groundwater head with respect to natural head conditions determined by the head solution resulting from all system stresses taking place in the aquifer rather than the hydraulic test itself,

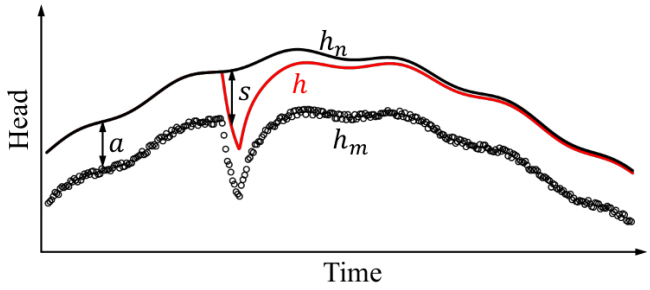

Figure 3.1: Drawdown (s) is the difference between natural heads (h_n, black line, would have been observed without pumping) and the actual heads (h, red line). The evolution of natural heads may have to be modelled for proper calculation of drawdowns. Modeling may be hindered by bias (a) affecting measurements (h_m, circles).

$$\mathbf{s} = \mathbf{h}_n - \mathbf{h}_m, \tag{3.9}$$

where $\mathbf{h}_m$ is the time series of head measurements at observation points, and $\mathbf{h}_n$ is the time series of natural head solutions at observation points.

The proposed method is based on assuming that the best approach for estimating $\mathbf{h}_n$ is a groundwater model itself, since it incorporates the underlying physics in the problem. However, this poses important challenges since both $\mathbf{s}$ and $\mathbf{h}_n$ depend on the unknown model, which is not exempt from uncertainties. As a result, flow models often exhibit systematic errors in the temporal evolution of heads simulated at specific points. These systematic discrepancies can be mainly attributed to two sources of errors: model bias and errors in field measurements. Model bias at observation points stems from structural and parametric uncertainties. That is, uncertainties associated with the underlying physics of the problem, which are not properly represented in the conceptual model (e.g., unknown recent past stresses, initial and boundary conditions and so on), and uncertainties associated with the spatial distribution of aquifer parameters such as the transmissivity, which is known to vary orders of magnitude even in moderately homogeneous systems. At the same

time, errors in head measurements (e.g., elevation data) can also generate systematic discrepancies between flow models and observations. The accuracy of the spatial position information can emphasize these errors, from which we could obtain, for example, wrong flow directions (or gradient), possibly inconsistent with the boundary conditions set in the model.

To overcome these difficulties, we propose to estimate drawdowns using a bias correction term (Figure 3.1) defined by an unknown vector $\mathbf{a}$ of biases at every observation point,

$$\mathbf{s}_e = \mathbf{h}_n - \mathbf{h}_m + \mathbf{a}, \tag{3.10}$$

The inverse problem is then posed as an optimization procedure aimed at finding not only the parameters, but also the correction terms that provide a good model fit. Carrera and Neuman (1986) and Hill (1992) already recognized the need of minimizing the biases between observed and simulated time series. Still, automatic calibration procedures nowadays consider parameter calibration only, without the incorporation/quantification of bias correction.

3.3.2 Calibration

In this section, we formalize the inclusion of the bias correction term in the automatic calibration process. Calibration of groundwater models through optimization methods typically minimize an objective function that contains a formal goodness of fit criterion, often the weighted sum of square head errors, and a regularization term that accounts for prior parameter information (e.g. Carrera and Neuman, 1986). In this case, considering that drawdown is estimated by equation (3.10) , the model with bias correction is $\mathbf{h}(\mathbf{p}) + \mathbf{a}$ and the objective function can be written as,

$$F(\mathbf{p}, \mathbf{a}) = F_h(\mathbf{p}, \mathbf{a}) + \lambda F_p(\mathbf{p}), \tag{3.11}$$

where

$$F_h(\mathbf{p}, \mathbf{a}) = (\mathbf{h}(\mathbf{p}) - \mathbf{h}_m + \mathbf{a})^t \mathbf{V}_h^{-1} (\mathbf{h}(\mathbf{p}) - \mathbf{h}_m + \mathbf{a}), \tag{3.12}$$

$$F_p(\mathbf{p}) = (\mathbf{p} - \mathbf{p}_m)^t \mathbf{V}_p^{-1} (\mathbf{p} - \mathbf{p}_m). \tag{3.13}$$

Here, $\mathbf{p}$ is the vector of model parameters, λ is the plausibility factor, $\mathbf{h}(\mathbf{p})$ is the groundwater model solution evaluated at the observation points at multiple observation times, $\mathbf{p}_m$ is the vector of prior information about the parameters, and $\mathbf{V}_h$ and $\mathbf{V}_p$ the corresponding covariance functions of errors in heads and parameters, respectively. From this, the calibration-optimization procedure can be formulated as a minimization problem, i.e., finding the set of parameters and bias correction terms that minimize the objective function,

$$(\hat{\mathbf{p}}, \hat{\mathbf{a}}) = \arg\min_{(\mathbf{p},\mathbf{a})} F(\mathbf{p}, \mathbf{a}). \tag{3.14}$$

We note that the bias correction prevents systematic errors to control the objective function, which may preclude a good estimation of parameters and/or a good model fit.

Following the idea that drawdown response contains information about parameters within the aquifer that is more valuable and with less measurement errors than absolute heads, we propose a new objective function with two terms. The contribution associated with the discrepancy between simulated and observed natural heads before the start of the hydraulic test F_{h_n}, and the contribution of drawdown errors during the hydraulic test itself F_s (including the recovery stage).

$$F(\mathbf{p}, \mathbf{a}) = F_{h_n}(\mathbf{p}, \mathbf{a}) + F_s(\mathbf{p}, \mathbf{a}) + \lambda F_p(\mathbf{p}), \tag{3.15}$$

where

$$F_{h_n}(\mathbf{p},\mathbf{a}) = (\mathbf{h}_n(\mathbf{p}) - \mathbf{h}_m + \mathbf{a})^t \mathbf{V}_h^{-1} (\mathbf{h}_n(\mathbf{p}) - \mathbf{h}_m + \mathbf{a}), \qquad t < t_i, \tag{3.16}$$

$$F_s(\mathbf{p},\mathbf{a}) = (\mathbf{s}(\mathbf{p}) - \mathbf{s}_e)^t \mathbf{V}_s^{-1} (\mathbf{s}(\mathbf{p}) - \mathbf{s}_e), \qquad t \geq t_i, \tag{3.17}$$

Introducing (3.10) into (3.17) we have

$$F_s(\mathbf{p},\mathbf{a}) = (\mathbf{s}(\mathbf{p}) - \mathbf{h}_n(\mathbf{p}) + \mathbf{h}_m - \mathbf{a})^t \mathbf{V}_s^{-1} (\mathbf{s}(\mathbf{p}) - \mathbf{h}_n(\mathbf{p}) + \mathbf{h}_m - \mathbf{a}), \qquad t \geq t_i, \tag{3.18}$$

This formulation deserves several considerations. First, the evaluation of the objective function $F(\mathbf{p},\mathbf{a})$ requires two different flow models. One standard model to simulate the natural evolution of the system $\mathbf{h}_n(\mathbf{p})$ (without the hydraulic test), and another to simulate the drawdown response $\mathbf{s}(\mathbf{p})$ to the hydraulic test. These two models share the same parameters and therefore the problem cannot be in general decomposed into two separate entities, which is the normal practice nowadays. Second, written this way, the covariance matrix of drawdown errors can express that drawdown data or changes in heads can be measured more accurately than absolute heads, if necessary. Third, the method is only applicable to linear problems. One option for non-linear problems (e.g., if T is a function of h) is to linearize the equation by treating the properties as time dependent (e.g., substituting $T(h)$ by $T(h^{k-1})$, where h^{k-1} is the head in the previous inversion iteration, which requires storing all heads from the previous iteration).

The strategy used to solve the optimization problem given by (3.14) is that of an iterative two-stage optimization process. It consists in taking the system to a first mid-step position during which the bias correction is determined by assuming that the parameters are known. Then, we use the estimated bias correction to take the system to its final stage by minimizing

drawdown errors through parameters estimation. These two stages are repeated until convergence. Formally, the procedure can be written as

$$\mathbf{a}^{k+1/2} = \arg\min_{(\mathbf{a})} F_{h_n}(\mathbf{p}^k, \mathbf{a}^k) \qquad t < t_i, \tag{3.19}$$

$$\mathbf{p}^{k+1} = \arg\min_{(\mathbf{p})} F_s(\mathbf{p}^k, \mathbf{a}^{k+1/2}) + \lambda F_p(\mathbf{p}^k) \qquad t > t_i, \tag{3.20}$$

where k denotes the iteration index.

Before initializing the process, we assume that we have collected all available information to develop an initial conceptual model of the system. We assume as well that we have performed a hydraulic test and collected field data before and during the test (e.g. head measurements and stresses data, such as pumping rates or weather data). With these assumptions, the algorithm consists in the following steps, also illustrated in figure 3.2 and 3.3:

1. Initialize the process at $k = 0$, defining $\mathbf{p}^0$,
2. Solve the natural head model to get $\mathbf{h}_n^k = \mathbf{h}_n(\mathbf{p}^k)$,
3. Estimate the bias corrective factor $\mathbf{a}^{k+1/2}$ minimizing $F_{h_n}(\mathbf{p}^k, \mathbf{a}^k)$ at each observation point and for $t < t_i$,
4. Compute drawdowns as $\mathbf{s}_e^k = \mathbf{h}_n^k - \mathbf{h}_m + \mathbf{a}^{k+1/2}$
5. Develop the drawdown model and calibrate $\mathbf{p}^{k+1}$ with computed drawdowns $\mathbf{s}_e^k$, by minimizing $F_s(\mathbf{p}^k, \mathbf{a}^{k+1/2}) + \lambda F_p(\mathbf{p}^k)$ at each observation point and for $t > t_i$,
6. Convergence check: if $\|\mathbf{p}^{k+1} - \mathbf{p}^k\| < \varepsilon_p$ and $\|\mathbf{s}^{k+1} - \mathbf{s}^k\| < \varepsilon_s$, where ε_p and ε_s are the convergence tolerances of parameters and drawdowns respectively, the iterative process end; else go to step 2.

The first optimization can be seen as curve-fitting the head data $\mathbf{h}_m$ observed at a given point prior to the hydraulic test with a known natural head

solution $\mathbf{h}_n$ by minimizing the vertical displacement between $\mathbf{h}_m$ and $\mathbf{h}_n$ (the bias correction, considered as a constant over time). Estimating the bias as constant, we are assuming that the trend (but not necessary the absolute value) of head measurements and that of calculated natural heads is correct. We are neglecting errors due to possible head measurement drifts and those derived from not knowing some natural head drift. The resulting bias correction factor $\mathbf{a}$ is then used, jointly with the natural head solution and head measurements, to estimate the drawdown $\mathbf{s}_e$ during the hydraulic test period. The

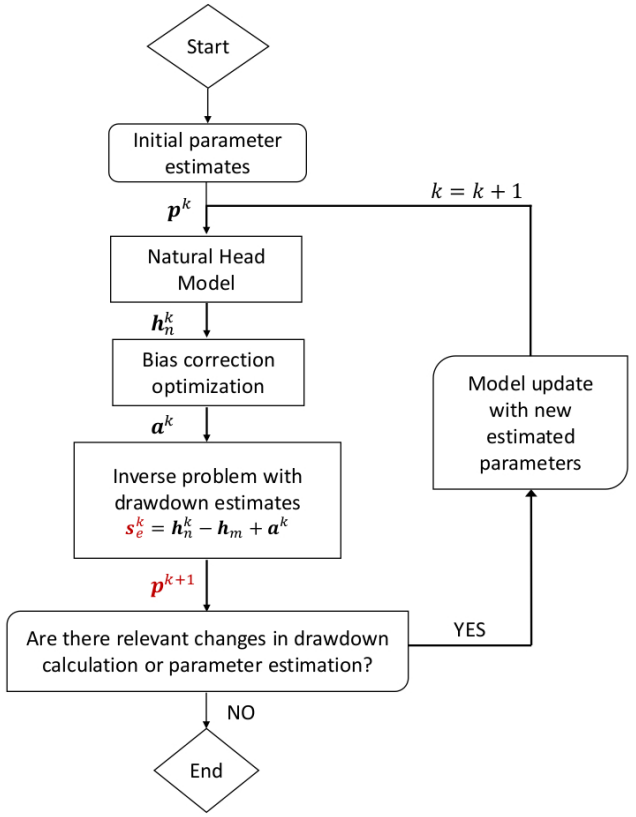

Figure 3.2: Schematic description of the proposed method. The final outputs from the iterative process are highlighted in dark red: de-trended and corrected drawdown $\mathbf{s}_e$ and aquifer parameters $\mathbf{p}$.

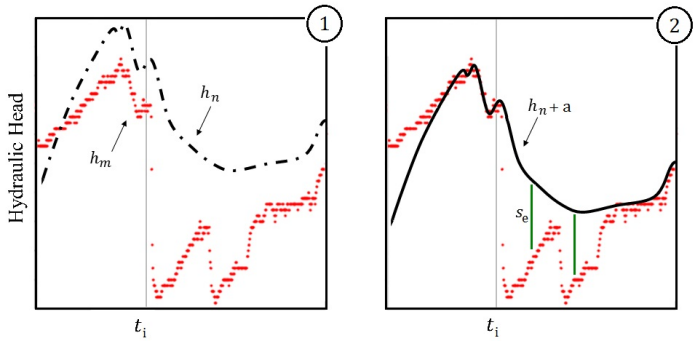

Figure 3.3: Drawdown estimation. On the left, biased heads measured in the field (red dots) and simulated natural head h_n calculated by means of a flow model (black dash line). On the right, bias correction a is added and the drawdown s_e during hydraulic test ($t \geq t_i$) is underlined (green arrow).

second optimization is the solution of the inverse problem written in terms of drawdowns (just calculated). Estimated parameters **p** are then employed to update the natural head model. At first glance, the procedure for estimating **a** seems similar to those in which time series are explicitly adjusted to remove the bias. But differences arise as **a** is estimated using calculated $\mathbf{h}_n$ which depends on hydraulic parameter estimates. As parameter estimates improve throughout the iterations, $\mathbf{h}_n$ improves and the bias changes, leading to improved drawdown estimates. The iterative process will stop when no more relevant changes are seen in drawdown calculation. In the following, we show that this iterative procedure converges to the true solution while removing model bias and measurement errors.

3.4 Application

We investigate the capabilities of the proposed method and some of its most important aspects. For this purpose, we build a synthetic heterogeneous aquifer characterized by long-acting multiple stresses and we simulate a hydraulic test (3.4.1). We then use the simulated head values obtained at few points to test the proposed method. Systematic errors were added to the simulated

head values to bias the head measurements (3.4.2). We finally compare these results with those obtained from the use of absolute head data in the traditional inverse modeling approach. In this case, biased and non-biased absolute head data are used (3.4.3). The latter provides an ideal parameter estimation solution, as we consider that errors in head measurements are zero.

3.4.1 Synthetic scenario

We consider a rectangular synthetic aquifer with dimensions of 30x30 km^2 (Fig. 3.4). The flow model is implemented in TRANSIN, a free finite element code developed by Medina and Carrera (2005). The domain is discretized in 8032 triangular elements. The size of the elements is 0.25 km in the hydraulic test area and gradually increases towards the domain boundaries. The model simulates the fluctuation history of hydraulic heads over a period of 1740 days, discretized in 787 time-steps. A variable time-step increment adjusted to stress conditions is used to properly simulate rapid head changes.

The decimal log of transmissivity is considered to vary in space following a multi-Gaussian random space function model characterized by an isotropic

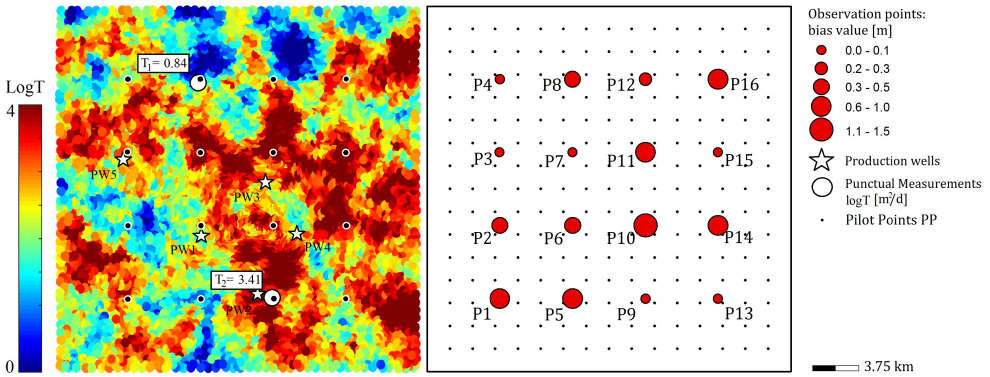

Figure 3.4: Aquifer system domain. Left, transmissivity field, location of pumping wells (white stars), point measurements of transmissivity (white circles). Right, location of pilot points (black dots) and observation points (red circles with a diameter proportional to the bias of head measurements).

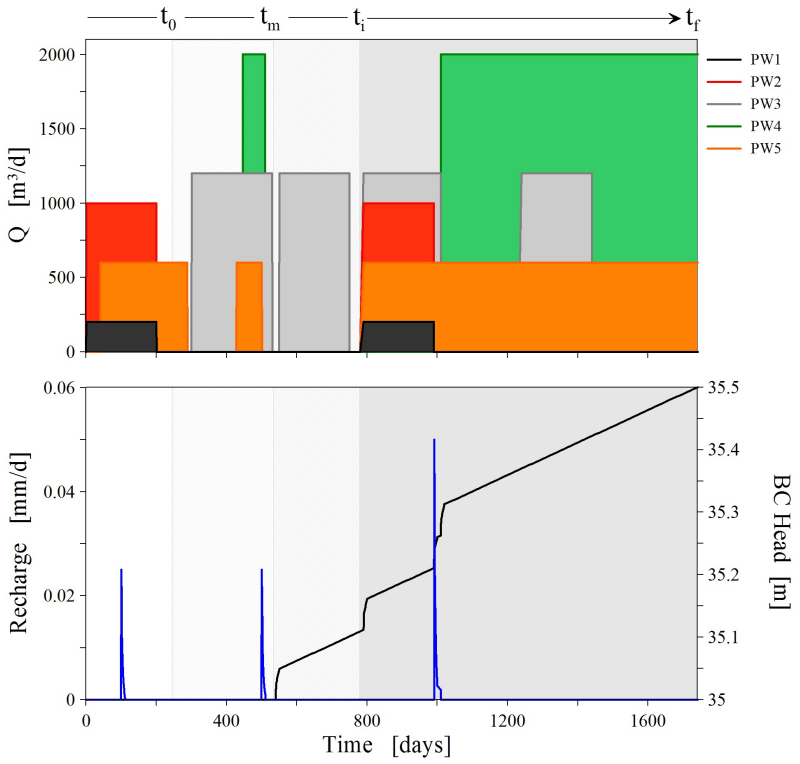

Figure 3.5: Anthropic and natural factors that cause head changes in the aquifer. Above, the pumping rate time series of the 5 wells installed in the area. Below, the time series representing the rainfall events (left axis) and the North boundary head evolution (right axis).

spherical covariance function with zero mean and a variance of one. The integral scale is 4 km. One realization of a sequential Gaussian simulation generated with SGEMS (Remy et al., 2009) was chosen to represent the transmissivity field (Fig. 3.4). The storage coefficient is assumed constant in the whole domain, i.e., $S = 0.0001$. The East and West boundaries are impermeable. The North and South boundaries are characterized by prescribed hydraulic heads. Boundary heads increase monotonically (but not linearly) from 35 to 35.5 m during the simulation in the North boundary (presented in Figure 3.5), whereas head is constant ($h = 30$ m) at the South. Head fluctuations during the simulation are caused by 3 important rainfall events and 5 production

wells operating in the area with variable flow rates. The location of these wells is shown in Figure 3.4.

A network of 16 monitoring piezometers are installed in the area and start recording water levels at time t_m = 540 days with a constant sampling period of 10 days. For each piezometer, water level measurements are biased by adding a uniform random noise [-0.2, 0.2] and an arbitrary positive systematic error $B(\mathbf{x})$ to the simulated heads. The imposed systematic errors $B(\mathbf{x})$ are given in Figure 3.4. The operation of all production wells after a time t_i = 790 days generates an important stress to the aquifer under monitoring conditions (see Figure 3.5). Consequently, the period (t_i,t_f) is considered to act as a hydraulic test from which one wishes to characterize the aquifer.

We assume to know 2 point measurements of transmissivity (shown in Figure 3.4), a rough estimation of the storage coefficient ($S = 0.01$), the true head values of the southern boundary (h = 30 m), and two head measurements taken at different times in the northern boundary ($h(t_m)$ = 35 m and $h(t_f)$ = 35.5 m).

3.4.2 The Filtering-Corrective Method

Our method requires two groundwater models, the natural head model that represents the natural trend of heads and the drawdown model. The specific features of these models for the application of the filtering-corrective method proposed are described below:

Natural head model. The initial transmissivity field $T^{k=0}(\mathbf{x})$ is estimated by ordinary kriging using the two available measurements (T_1 and T_2). For this, we assumed that the geostatistical model is perfectly known. The initial storage coefficient is set to $S^{k=0} = 0.01$ (Fig. 3.6). Boundary conditions are identical to those of the true model, except that northern head is assumed to increase linearly over time, from $h(t_0)$=35 m to $h(t_f)$=35.5 m. In order to represent a typical scenario, we consider that the initial condition of the model is unknown (Gupta et al., 2012; Seck et al., 2015). To handle this, following the

normal practice, we go back in the past with the model for a time period prior to the calibration period to attenuate the spurious transient response given by possibly wrong initial conditions. Thus, the model simulates the fluctuation history of natural heads h_n from $t_0 = 240$ to $t_f = 1740$ over a period of 1500 days. The pumping history at time $t < t_0$ is unknown and consequently initial heads at $t = t_0$ are determined by a blind steady-state solution (without considering extractions or recharge stresses). The time and spatial discretization coincide with those of the synthetic scenario. Rainfall events and pumping well extractions control the transient natural head evolution. We consider the 2 recharge events and pumping rates up to $t = t_i$ shown in Figure 3.5, which are identical to those of the synthetic scenario. In the optimization process, we consider h_n and h_m data from t_m to t_i. We build the diagonal matrix $\mathbf{V}_h$ assigning a unit weight to all available observations, except for the last two measures closest to time t_i, to which a weight of 10 is assigned. In this way we want to ensure drawdowns to be almost zero at the beginning of the hydraulic test.

Drawdown model. The model simulates the fluctuation history of drawdown over a period of 950 days (from $t_i = 790$ to $t_f = 1740$), discretized in 186 time-steps. Time and spatial discretization coincide with those of the synthetic scenario. Boundary and initial conditions are easily set as discussed in Section 3.2: no flow boundaries (*East* and *West*) do not change, prescribed head boundaries (*South* and *Northern*) are prescribed zero head boundaries, and the initial drawdown is zero everywhere. Only pumping rates during hydraulic test period (from t_i to t_f) are considered. They are simulated prescribing the flow rate with time according to Figure 3.5. The optimization process is carried out applying both the classical inverse problem (zonal parametrization) and the regularized pilot points method (Alcolea et al., 2006), with 225 pilot points uniformly distributed throughout the model area (shown in Figure 3.4). The former is used for storage coefficient estimation, as the parameter is spatially homogeneous, while the latter is used to estimate the transmissivity field through conditional estimation. We employ the same geostatistical model as before. The covariance function $\mathbf{V}_s$ is constructed by assigning a

unit weight to all observations while the plausibility term is $\lambda = 1$.

It could be rightfully argued that structural model errors in this synthetic example are modest. They are restricted to the neglecting of small scale variability, the erroneous initial condition and the time variability of the North boundary heads. These types of uncertainties are frequent. But other sources of model error may also affect real models: flow dimension (the Dupuit approximation may not be valid), model extent (location of boundaries often uncertain), etc. We have opted for relatively simple errors so as to facilitate the discussion and because model errors are usually reduced during the modelling process, which would be hard to reproduce in a synthetic example.

3.4.3 Traditional calibration with head data

We use absolute biased head measurements h_m in the traditional inverse modeling approach for estimating hydraulic parameters and compare the results with the ones obtained from the application of the proposed method. The model simulates the fluctuation history of hydraulic heads over a period of 1500 days, from t_0 to t_f. Time and spatial discretization coincide with those of the synthetic aquifer. Initial and boundary conditions as well as the initial hydraulic parameters are the same as those used for the natural head model. Since we simulate the overall behavior of the system, we consider all the stresses that affect the aquifer: recharge events and production wells, including the hydraulic test pumping rates (Fig. 3.5). We calibrate the model employing two different sets of head observations: the biased head measurements used in the natural head model, and the exact head measurements obtained directly from the true aquifer simulation. In both cases, the model is calibrated in the time period between t_m and t_f.

3.5 Results and Discussion

3.5.1 Overall performance

We start by analyzing the overall performance of the proposed method. Figure 3.6 displays the transmissivity field and drawdown estimates obtained at three iterations (0, 1, and 7) of the two-stage optimization method. The figure also compares these results with the true solution. We first note that the process converges in just seven iterations. The most important change in the parameter estimates (including drawdown) occurs in the first iteration. The storage coefficient decreases two orders of magnitude approaching to the real value, and the transmissivity field considerably changes in terms of both spatial patterns and absolute values towards the true solution. In subsequent iterations, S and $T(\mathbf{x})$ improve but field patterns are maintained. Comparison with the true solution points out that the method can identify the overall trends of transmissivity variation. The final drawdown estimates obtained after 7 iterations resemble the true solution, except in the central eastern area of the domain.

The estimated transmissivity map is smooth because the pilot point method is coupled with conditional estimation. Small-scale variations cannot be properly represented by the conditional estimation pilot point method. Still variability patterns are well captured in the central portion and become more blurred toward the boundaries for several reasons. First, no observation points are available, so that there is a strip of domain that remains "unforked" (i.e., without observations on both sides) near the boundaries. Second, even if observations had been available at the boundary, transmissivity estimates would have remained uncertain because drawdowns are less informative about transmissivity. Near no flow boundaries, the normal component of the gradient is zero regardless of the transmissivity value. Near zero drawdown boundaries, drawdown will be small regardless of the transmissivity value. Observations near the boundary can be relevant to understand the type of boundary condition and to understand natural heads, but they are not very informative about transmissivity. Comparing the estimated S and $T(\mathbf{x})$ with estimates obtained

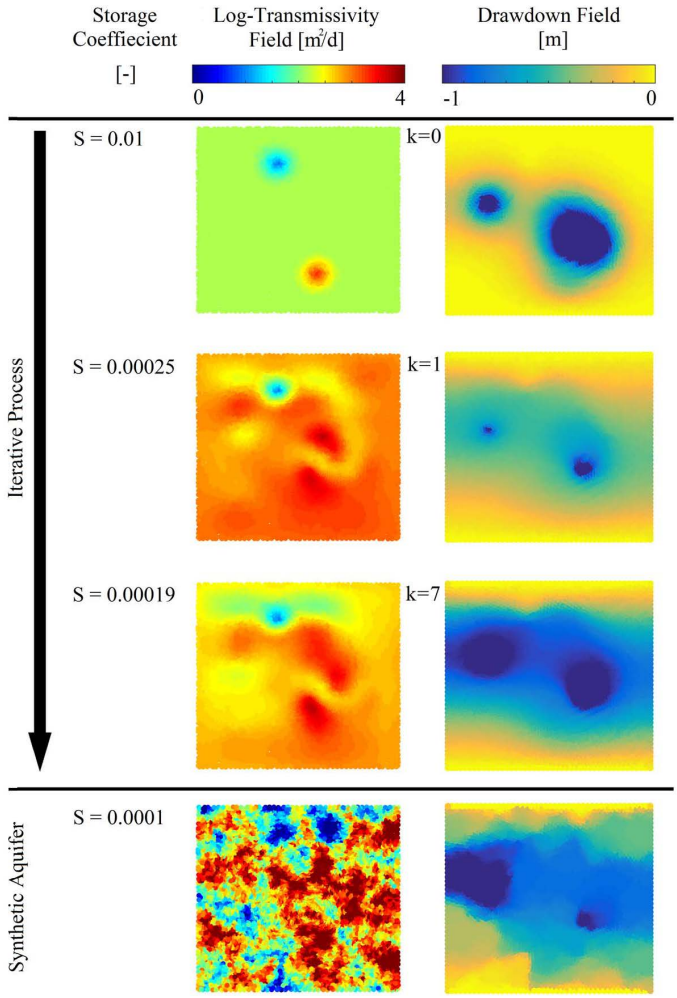

Figure 3.6: Sequence of estimated hydraulic parameters (T and S) and drawdown fields along the iterative process. The top row contains the initial data (k=0, i.e. the hydraulic parameters used at the beginning of the modeling phase for the natural head model). The next two rows contain the results of the first (k=1) and last (k=7) iterations, respectively. The "real" aquifer data are plotted in the bottom row for comparison purposes. The estimated aquifer behavior (drawdown) resemble the real one. At the same time, the zones of high and low permeability are well captured, even if conditional estimation is not capable of reproducing small scale variability.

using directly head data may be more appropriate than comparing them with true values.

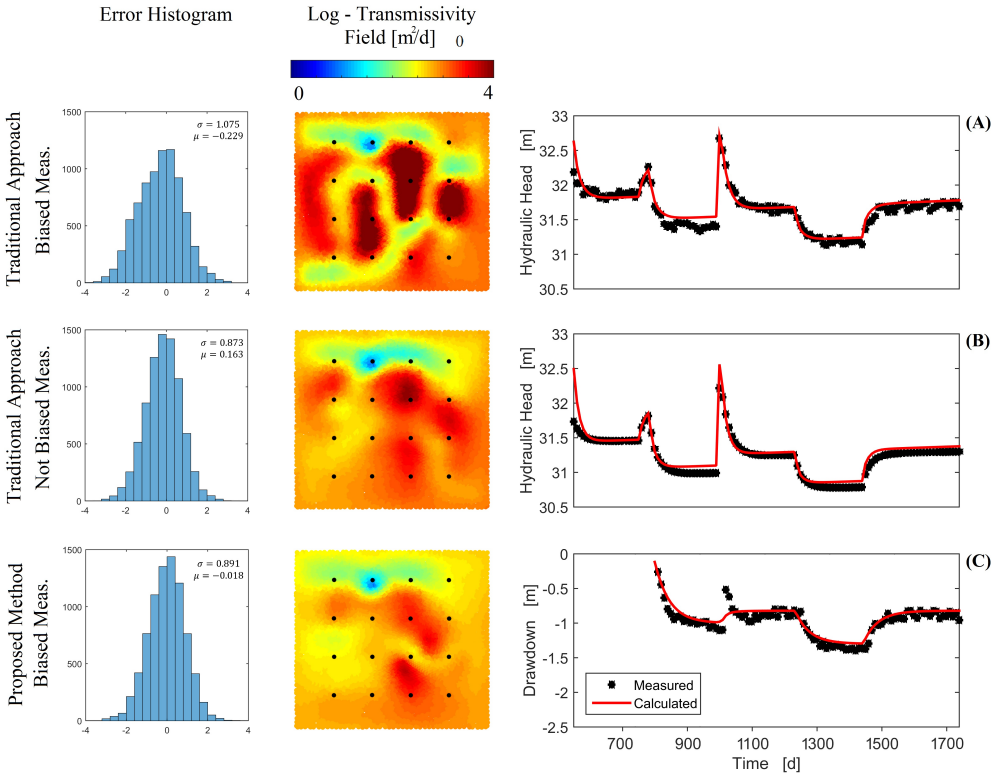

Figure 3.7: Comparison of the three calibrations (A, top row, traditional inversion with noisy and biased measurements; B, middle row, same with exact measurements; and, C, proposed method). The comparison is made in terms of estimated transmissivity (decimal logarithm) $\log_{10} T$ error histograms (left column), transmissivity fields (middle column) and measured (dots) and computed (red line) hydrographs at one observation point (right column). The hydrograph fits are analogous, but error histograms for the "ideal" (exact head data) top row and the proposed method are smaller than with traditional inversion.

Figure 3.7 displays the estimated transmissivity fields and histograms of errors obtained by the use of head data in the traditional inverse modeling approach. The traditional approach with exact (non-biased and error free)

head measurements provides the "best" estimate of the transmissivity field conditioned to head data and transmissivity values because in this case head errors were neglected. Therefore, we could qualitatively state that the estimated field recovers all the information contained in the data. The filtering-corrective method yields results that are similar to this best solution, which allows us to conclude that the method is capable of properly filtering systematic errors in head data without sacrificing fitting accuracy. On the contrary, the traditional approach with biased head measurements converges to an incorrect solution of the transmissivity field with an important overestimation of transmissivity in extensive areas of the domain. Note though that the goodness-of-fit is still similar. These results are supported by quantitative measures given by the histograms of the transmissivity error, which is defined by $\varepsilon(\mathbf{x}) = \ln T^{true}(\mathbf{x}) - \ln T^{(7)}(\mathbf{x})$. The filtering-corrective method and the traditional approach with exact measurements follow a normal distribution centered close to zero with a standard deviation of about $\sigma \approx 0.9$. Instead, the traditional approach with biased measures exhibit an asymmetric distribution centered at $\mu = -0.23$ with $\sigma = 1.1$.

In sum, results demonstrate that the filtering-corrective method should be the choice for groundwater modeling calibration when head measures are systematically biased. In this case, the method is capable to automatically detrend natural heads and estimate drawdown data for accurate aquifer characterization. Otherwise, caution should be taken when dealing with systematic head errors in groundwater models since these errors can lead to a poor estimation of transmissivity even when a good fit is obtained. Results also show further evidence of what is already known, namely that a model cannot be trusted just for having a good fit.

3.5.2 Natural heads, drawdowns, and bias correction

We analyze the evolution of the estimated natural head, drawdown, and bias correction obtained by the filtering-corrective method to get further insight.

Figure 3.8 displays the natural heads and drawdown hydrographs at one observation well for several iterations. Consistently with previous results, the first iterations ($k = 0, 1, 2$) exhibit a great improvement. The estimated natural head approach the real solution, never reaching it because of systematic errors, but reproducing well the relative head variations in the system.

This is actually a very nice feature of the method proposed, i.e., we can remove the bias and calibrate the model only through relative heads. In general, small discrepancies can be observed at early times (up to time t_m) due to a poor representation of the initial condition in the natural head model but an almost constant error is displayed for longer times $t > t_m$ (Fig. 3.8). These

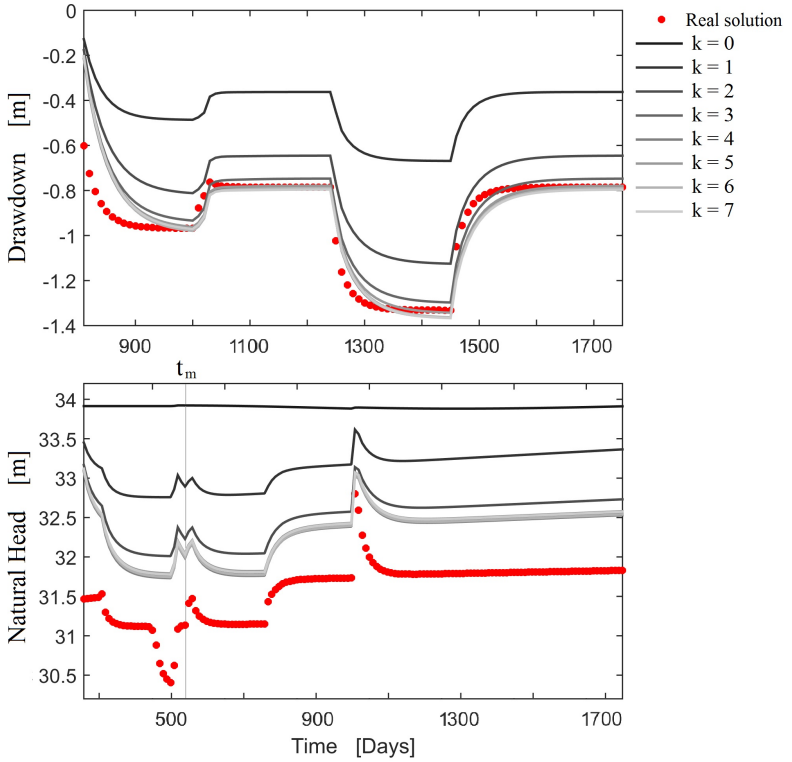

Figure 3.8: Drawdowns (above) and natural heads (below) calculated along the iterative process in observation well OW12 are presented. Real solutions (red dots) are also plotted for comparison purposes.

model errors partially reflect that head observations are systematically biased. Most importantly, the estimated drawdown data converge satisfactorily to the real solution (Fig. 3.8), meaning that both modeling and measurement errors have been corrected. It is important to underline that in general, the broader and more correct the knowledge of stresses (in particular those that generate long transient responses), the better the estimate of natural heads. A poor definition of the stresses could rebound on hydraulic parameter estimates, without affecting the quality of the calibration (Fig. 3.7).

An additional note of caution is required regarding the impact of high frequency head fluctuations on long-term large scale models as the one discussed here. Typically they are driven by fluctuating stresses (Earth or sea tides, daily fluctuations in pumping, barometric pressure, etc.) that are rarely included in models because they are hard to model, because their impact is relatively small, because they dissipate quickly, because they reflect local parameters that may not be relevant for large scale models, and because they

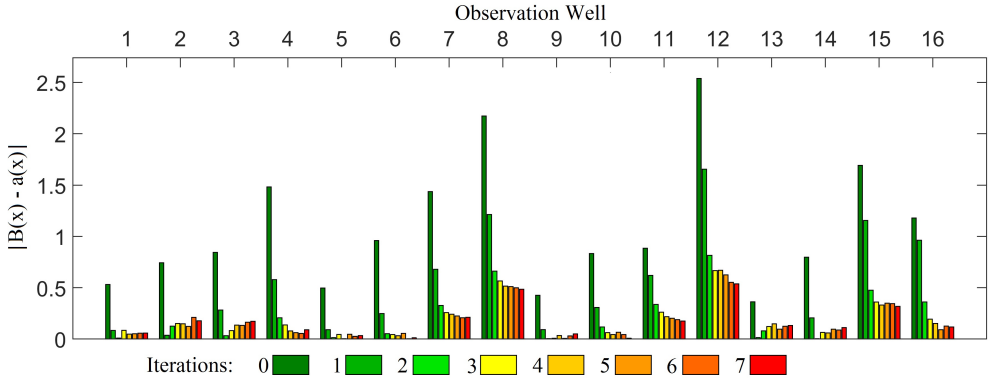

Figure 3.9: For each observation well, the evolution of the absolute difference between imposed error $B(x)$ and estimated bias correction $a(x)$ is presented. Throughout the iterations, in some wells the corrective factor get closer and finally approaches $B(x)$. Others present an estimated bias that initially tends to B(x) but finally converges to another value (e.g. OW8 and OW12). The difference that remains probably acts as correction for errors not related to $B(x)$, as, for example, modeling errors.

are filtered away when averaging dense time series data. Still, they may be relevant in numerous occasions: when drawdowns are small (low Q/T ratio or distant piezometers), specially for short term, or when measurements are scattered, so that averaging them is not possible. A number of methods are available in such cases (Halford et al., 2012; Garcia et al., 2013; Del Val, 2020).

Due to its importance in the overall process and its dual role in dealing with measurements and model errors, we analyze the evolution of the correction term $a(\mathbf{x})$ during the iterative process. For this purpose, we show in Figure 3.9 the evolution of $\Delta = \mid B(\mathbf{x}) - a(\mathbf{x}) \mid$ with the number of iterations at each observation well. Results show an important decrease of Δ in the first iterations during which model parameters are being actively adjusted based on relative heads. After a few iterations, the parameters reach a final solution and Δ seems to stabilize to a constant value. In some cases, for example, in observation wells OW1, OW5 and OW6, the correction term $a(\mathbf{x})$ approaches to $B(\mathbf{x})$, meaning that model errors no longer affect the estimated natural head in these zones. However, an appreciable difference remains in other observation wells. Most of them are located in the north-eastern part of the domain where boundary conditions control the outcome of the model. Here, the correction term $a(\mathbf{x})$ accounts also for structural model errors (neglecting small scale variability, errors in initial conditions and time dependence of North boundary head) that cannot be resolved.

3.5.3 Discussion

The proposed method can be viewed as splitting the complex modelling problem (model construction and parameter estimation) into two simpler problems: the natural heads model, which is sensitive to boundary and initial conditions, and the drawdowns model, which is sensitive to aquifer parameters within the model domain. While drawdowns have been widely used in groundwater hydrology, primarily for pumping test interpretation, the proposed method allows generalizing the problem to large scale regional models. In this context, the method is similar to what Halford and Jackson (2020)

term "stress-response models", which isolate the response of portions of the model to known stresses, thus facilitating model construction. The question may be raised as to when is this splitting favourable and whether solving the full problem might be better. We do not have a straight answer to this, but we feel that two criteria should be followed: knowledge and sensitivity. First, stresses should be well known for the drawdown (stress-response) model to be reliable. Second, sensitivities should be quite well separated for the problem to converge. The natural heads model is primarily sensitive to boundary and initial conditions. The drawdowns model is basically sensitive to hydraulic parameters within the model domain and, possibly, the type of boundary condition, but not the actual value of boundary heads and fluxes.

3.6 Conclusions

Systematic errors in drawdown data driven by uncertain past stresses and errors in head measurements typically hinder the use of drawdown data in complex aquifer systems. We have presented a filtering-corrective method for automatic calibration of groundwater models that is capable of detrending natural heads and correcting head measurements with a bias correction term. This procedure is shown to improve drawdown estimates and, consequently, the estimated properties of the aquifer. The method combines a natural head model with a drawdown model in the same inverse problem. Since these two models depend on the same parameters, a two-stage iterative optimization algorithm has been developed to jointly estimate the bias and the parameters.

Among the features of the proposed method we highlight the following findings:

- First, the use of a groundwater natural head model for h_n estimation. Instead of using statistical methods or data from distant wells, we have chosen to calculate h_n, necessary to de-trend head measurements, through a numerical flow model. Applying the proposed method is thus possible to take into consideration aquifer heterogeneity and the different

influence that stresses have on observation points, given the spatial variability of the hydraulic parameters.

- The correction term $a(x)$ is crucial for a good estimation of drawdowns. Basically, we trust the relative variations of both calculated natural heads and head measurements, but not their absolute values that are therefore corrected applying the bias correction.
- Dividing the process into two groundwater models made it possible to attenuate the effect of uncertainties associated with the definition of boundary and initial conditions in the natural head model.
- At the same time, no uncertainties characterize boundary and initial conditions in the drawdown model, where hydraulic properties have to be estimated. Thus, the optimization process is not directly affected by these uncertainties.

The comparison with traditional approach also highlighted some interesting and other well-known aspects of inversion.

- Applying the proposed method has allowed us to reach the same quality of results that could be obtained if we had used exact (not-biased) field measurements, which is practically impossible.
- Trying to calibrate a flow model with wrong (biased) observation data could lead to very good fits, with parameters that are far from the true ones.
- The inverse problem is a very powerful tool for aquifer characterization, but results may be affected by errors in observation data and conceptual model. Therefore, results consistency should be always checked with independent information.

The fact that the corrective term is properly estimated improves the quality of both natural head measurements and models. This is important because drawdowns are relevant for estimating hydraulic parameters (T and S), but

by themselves contain no information of where and how much groundwater flows from/to, which is the ultimate goal of modeling.

Chapter 4

The worth of stochastic inversion for identifying connectivity by means of a long-lasting large-scale hydraulic test: the Salar de Atacama case study

This chapter is an edited version of: Trabucchi, M., Fernàndez-Garcia, D., & Carrera, J. (2021). The worth of stochastic inversion for identifying connectivity by means of a long-lasting large-scale hydraulic test: the Salar de Atacama case study. *Water Resources Research* (Under review)

4.1 Introduction

Understanding aquifer heterogeneity in terms of the spatial variability of the hydraulic properties is important for the assessment of groundwater resources and the protection of its quality. Special interest is growing for the role of connectivity in aquifers, i.e., the presence of high permeability geological bodies that can lead to preferential flow (Western et al., 2001; Zheng and Gorelick, 2003; Knudby and Carrera, 2005; Fernàndez-Garcia et al., 2010; Bianchi et al., 2011; Renard and Allard, 2013). These bodies act as channels that may control the behavior of hydrogeological systems, causing flow and transport to concentrate in just a small portion of the medium (de Marsily, 1985).

In contaminant transport, these geological features typically leads to anomalous concentration breakthrough curves measured at observation points with unexpectedly fast arrivals, peaked distributions and persistent tailing (Wen and Gómez-Hernández, 1998; LaBolle and Fogg, 2001; Zinn and Harvey, 2003; Zheng and Gorelick, 2003). Tailing can be attributed to the varying advection time of highly mobile zones (well-connected structures) and less mobile zones, and the exchange of solute mass between them (Haggerty and Gorelick, 1995; Carrera et al., 1998; Haggerty et al., 2000; Willmann et al., 2008; Fernandez-Garcia et al., 2009). In practice, tailing complicates and extends the duration of most remediation efforts in groundwater polluted sites, since part of the contaminant becomes temporally trapped in low permeability regions and released by back-diffusion when pumping ceases (Chapman et al., 2012). The latter generates the so-called rebound of the contaminant concentration after remediation (e.g., Stroo et al., 2012; de Barros et al., 2013). The presence of well-connected structures can also significantly affect the assessment of risk posed by a contaminant, controlling the ultimate position of the risk hot spot (Henri et al., 2015). Connectivity is also of importance in oil and gas production. During waterflooding, channeling results in water bypassing large quantities of oil, producing huge losses in recovered oil and monetary income (Hoefner and Fogler, 1988).

Well-connected structures can also generate unexpectedly fast aquifer responses in hydraulic tests. Meier et al. (1998) and Sánchez-Vila et al. (1999) showed that the storage coefficient estimates S_{est} obtained from Jacob's method interpretation of pumping tests depends on the connectivity between pumping well and observation well. If they are well connected the response will be fast and the estimated storage coefficient low. Similarly, the interpretation of a tracer test can lead to an under/overestimation of porosity, depending on the high/low connectivity between the tracer injection point and the observation (Sánchez-Vila and Carrera, 1997; Fernàndez-Garcia et al., 2002; Trinchero et al., 2008).

The effects summarized above highlight the importance of connectivity in many hydrogeological applications and underscore that it is important to characterize heterogeneity with special attention to the presence of connectivity structures. Stochastic hydrogeology can properly represent the spatial variability of aquifer properties by considering the parameters to be spatial random functions. This renders the flow equation a stochastic partial differential equation, which can then be coupled with the inverse problem in several ways (e.g., RamaRao et al., 1995; Gómez-Hernánez et al., 1997b; Alcolea et al., 2006) to infer the heterogeneous structure of an aquifer. The application of the stochastic inverse method in synthetic aquifers and laboratory experiments (Yeh and Liu, 2000; Liu et al., 2007; Hao et al., 2008, among others) have shown a satisfactory characterization of preferential flow channels (Hao et al., 2008). The application in relatively small field sites have also demonstrated its capability to reveal and identify the coarse structure of heterogeneity and connectivity patterns when using information from cross-hole pumping tests (e.g., Meier et al., 2001; Berg and Illman, 2013; Brauchler et al., 2013; Hochstetler et al., 2016) and tidal responses (e.g., Alcolea et al., 2007). However, few applications span to the regional scale, exceeding hundreds of meters. An exception is the work of Pool et al. (2015), who characterized the spatial variability of transmissivity of an aquifer of ca. 1000 km^2. The authors were capable to identify through the application of the regularized pilot point method (Alcolea et al., 2006) some of the main large-scale connectivity

structures.

Aquifer heterogeneity can qualitatively range from random to highly organized, depending on the primary and secondary processes that contribute to the formation of the porous media (Western et al., 2001). Sediment deposition in fluvial systems illustrates how primary processes can lead to well-organized connectivity structures occurring over multiple scales that range from well-connected sand lenses to paleochannels (Sanchez-Vila et al., 1996; Pedretti et al., 2014). Secondary processes such as tectonic events and dissolution produce fractures, fault zones and karst networks that can act as impermeable barriers or preferential flow paths. The latter are very common in fractured media (e.g., open fractures) and karstic media (e.g., dissolution conduits).

This work focuses on karst systems formed in saline aquifers. Saline systems constitute a small percentage of the world karst aquifers (BGR et al., 2017), but are extremely important from an economic and environmental point of view. The Central Andes contain three of the largest salt flats in the world: the Salar de Uyuni in Bolivia, the Salinas Grandes in Argentina, and the Salar de Atacama in Chile. Due to climatic conditions, these formations house unique environments and natural reserves (e.g., Flamingos protection zones) as well as valuable mineral resources (e.g., lithium for car batteries and potassium for fertilizers, among others), which are highly concentrated in the brine (Kesler et al., 2012; Vikström et al., 2013). In this context, connectivity can strongly condition the economic development of salt flats as well as their surroundings. Connectivity can affect exploitation efficiency by enhancing the inflow of less evaporated brine into the aquifer, diminishing its mineral potential. The presence of karst conduits can also connect the aquifer with environmentally sensitive areas.

Although the need to characterize preferential flow channels in these systems is evident, the task is challenging because of their complexity and dimension. In the Salar de Atacama, the case study in the present work, we have to deal with an extension of about 3000 km^2. At this scale, the uncertainty related

to external stresses increases as well. Beyond uncertain external conditions, complexity is further driven by the exploitation of part of the brine reservoir in the nucleus. All these stresses should be filtered out to properly characterize the aquifer through hydraulic tests information. Several methods can be used to filter external stresses from hydraulic test data (see, e.g., Halford et al. (2012); Garcia et al. (2013)). Recently, Trabucchi et al. (2021) have presented a corrective-filtering method to filter systematic errors in drawdown data during the automatic calibration of a groundwater model.

In this chapter, we present and interpret a sequence of long-lasting hydraulic tests using stochastic inversion to characterize the large-scale connectivity structures of the Salar de Atacama aquifer using drawdown data obtained with the corrective-filtering method. In doing this, we address the following questions: 1) Is it possible to assess the heterogeneity over tens of kilometers in karst aquifer by performing long-lasting cross-hole hydraulic tests?, 2) can we infer the existence and location of highly conductive zones (preferential flow paths) and delineate aquifer connectivity structures through stochastic inversion?, and 3) can we observe a scale effect of the hydraulic conductivity in karst systems at the regional scale?

4.2 Site description

The Salar de Atacama (SdA) is the third largest Salar in the world, after Uyuni in Bolivia and Salinas Grande in Argentina, with an area that covers some 3000 km^2 and an average elevation of 2300 m above sea level. The SdA basin is located in the south-central part of an endorheic compressive tectonic basin in northern Chile and it is surrounded by mountains. In the east, the Andean mountains encloses the basin with a north-south trending line of volcanoes, including the Lascar volcanoe, which is one of the most active in Chile nowadays.

In the west, the SdA is bounded by the Cordillera de Domeyko and the Cordillera de la Sal, which run parallel to the main chain. In the south, the

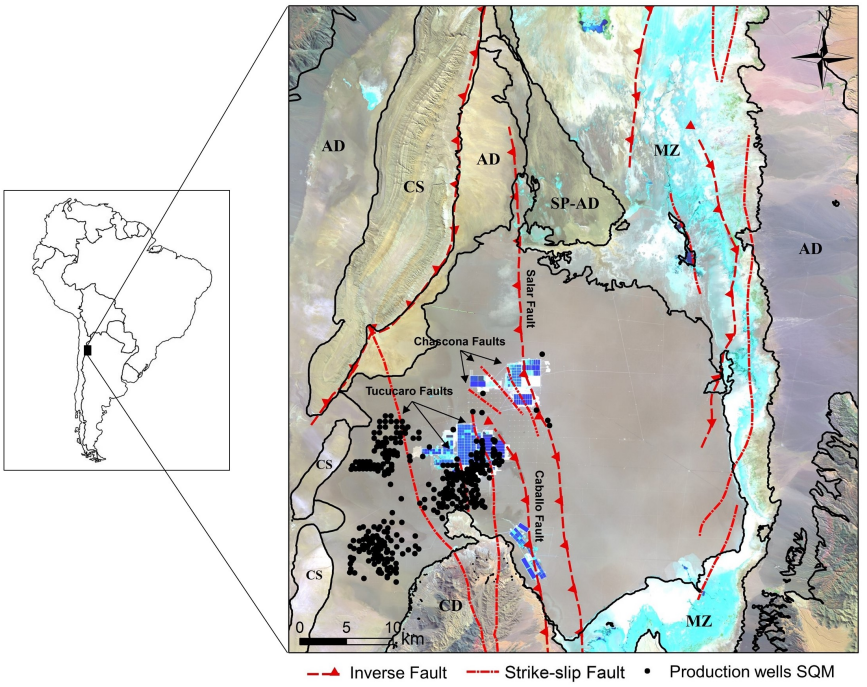

Figure 4.1: Main features of the Salar de Atacama. 1) Subaerial environments: marginal zone (MZ), Halite nucleus (H), alluvial deposits (AD), Cordillera de la Sal (CS), alluvial deposits of the San Pedro River (SP-AD) and Cordon de Lila (CDL); 2) tectonic structures (red lines) and 3) exploitation areas (dark dots = production wells; blue areas = precipitation ponds).

Cordon de Lila cross-cut the actual trend of the Andean Range. The SdA north boundary consists of deltaic deposits formed by the San Pedro River which, jointly with the Vilama River, constitutes one of the main water inlets of the SdA basin. The San Pedro and Vilama rivers run along the north-south direction. The San Pedro river has an average flow rate of 1 m^3/d with torrential episodes of up to 25 m^3/d. The Vilama river disappears in the south of San Pedro de Atacama and has an average flow rate of 0.2 m^3/d (Salas et al., 2010). Because of its location and geographical features, the SdA is characterized by climatic conditions that are among the most arid of the world, with an annual

average precipitation of 20 mm/year and an evaporation rate of about 1000 mm/year in vegetated areas. This value rapidly decreases when approaching the rugged halite nucleus, where aquifer brine evaporation is almost absent (Kampf et al., 2005).

The SdA encompasses several subaerial environments; the alluvial-fan environment and the marginal mudflat of the basin are mainly characterized by siliciclastic sediments, whereas the eastern marginal zone (about 1400 km^2) and the nucleus zone (ca. 1600 km^2), which constitute the SdA basin, are dominated by evaporitic deposits. The former is characterized by carbonate and sulfate sediments. The latter consists of nearly pure halite covered by efflorescent halite crust with meter-scale polygon structures and a highly jagged surface that result from the evaporation of ephemeral surface water (Lowenstein et al., 2003). Some areas of the salt flat form part of Los Flamencos National Reserve. The Laguna Cejar is a sink-hole lake in the SdA located 18 km away from San Pedro. It has a salt concentration that ranges from 5 to 28% (50 to 280 parts per thousand), producing a floating effect similar to the Dead Sea.

The minerals distribution in the SdA follows the precipitation sequence of evaporites but it is not concentric with respect to the depocentro of the Salar (Figure 4.1). The Bull's eye pattern is not developed, as the SdA basin is asymmetrically fed by the surface and groundwater recharge stemming from the east, south-east and north boundaries (Salas et al., 2010). Hidden beneath the SdA uninterrupted flat surface is the Salar Fault System (SFS, reverse fault zone), which constitute a north-northwest trending line characterized by past strike-slip movements with important vertical motions. The main fault of the SFS, active since the Pliocene, is the Salar Fault (SF), which cut the Halite Nucleus in two parts: the upthrown block in the western side and the downthrown block in the eastern side. Through the Pliocene and Quaternary, hundreds of meters of vertical offset occurred, increasing the accommodation space in the eastern zone and leading to differential halite unit thickness. While in the western part, the halite nucleus has a thickness of about 200 m, in the eastern side this thickness can reach a depth of about 900 m (Jordan et al.,

2002). Nevertheless, the topographic manifestation of faults and folds is not visible, probably due to the aggradation of subaerial efflorescent crusts that kept pace with the subsidence (Lowenstein et al., 2003).

From a hydrostratigraphic point of view, the Salar brine reservoir of the nucleus can be vertically classified into five main stratigraphic units that can be grouped into three hydrogeological units. The upper unit of halite (thickness up to ca. 50 m) represents the main aquifer of the nucleus, with hydraulic conductivities ranging from 10^1 to 10^3 m/d. Deeper into the nucleus, a second aquifer unit mainly composed by halite (1-10 m/d) is separated from the upper hydrogeological unit by a relatively thin layer formed by gypsum, carbonate and sometimes clay that acts as an aquitard system. As previously mentioned, the groundwater entering from the northeast, east and southeast boundaries constitutes the main source of recharge of these aquifers. Again, despite the hyper-arid environment, sporadic precipitation events into the nucleus are also an important component of recharge (Boutt et al., 2016).

The SdA aquifer has been continuously explored and exploited by different mining companies since 1994. The exploitation has grown over the years and is still growing. Two companies are currently exploiting the area: Albemarle (former Rockwood Lithium GmbH) and SQM (Sociedad Química y Minera). The former developed its plants in the South of the nucleus, in the surroundings of the Cordon de Lila (Ignimbrites). The latter, which is the main exploitative company of the SdA, covers a larger surface that extends from the SW up to the center of the nucleus (Figure 4.1). Exploitation focusses on Lithium (Li) and Potassium (K) production, being Li increasingly required for batteries manufacturing (Kesler et al., 2012) and K as a fertilizer. The production is usually seasonal, with periods of high exploitation alternating low activity periods. The process of exploitation consists of pumping pore brines from the aquifer into solar saltworks (evaporation ponds), where a saline sequence precipitates leading to Li-rich-brine that is treated to obtain lithium carbonate (Pueyo et al., 2017). Leftover brine is reinjected into the system, contributing to the recharge of the shallow aquifer.

The high economic and environmental interest of the area has led to increased attention of the general public and the scientific community towards the salt flats, which have become the target of several studies aimed at better understanding the dynamics of the system (Boutt et al. (2016); Munk et al. (2018); Marazuela et al. (2018, 2019) among others). SQM has also explored the nucleus of the aquifer over a decade to improve the knowledge about the system in terms of geology, hydraulic properties and geochemistry. The following important information was provided by SQM to conduct the current study. This information refers to the upper aquifer unit, which is the aquifer of interest in this study:

- *Geophysics studies aimed at characterizing the Salar Fault System*. In addition to the main fault (SF), three different minor fault-sets, preferentially oriented N-S and NW-SE, have been found in the nucleus: the Tucucaro faults on the South-West, the Caballo fault in the South, and the Chascona fault in the center of the nucleus. Their hydraulic role is not clear (Figure 4.1).
- *Hydraulic tests at different scales*. A fairly complete database of hydraulic conductivity and transmissivity estimates of the shallow aquifer consisting in 520 packer hydraulic tests and 172 pumping tests of relatively short duration (Figure 4.4).
- *Brine elements concentration*. A total of 57 brine samples taken from the upper aquifer and located in the NE zone of the nucleus was provided. This information includes Mg, Li, SO_4, H_3BO_3, Cl, Na, K and Ca concentrations.
- *Brine isotopes studies*. Isotopic data of the shallow aquifer are available, taken during a sampling campaign carried out in 2011 (Huerta, 2012). Data of isotopic deviation $\delta^{18}O$ are available for 75 points distributed in the whole nucleus.

4.3 Methodology

The method used to characterize the heterogeneous structure of the aquifer and identify large-scale preferential channels involves two main components: (1) a large-scale, long-term cross-hole hydraulic test aimed at observing multiple aquifer responses over long (kilometers) distances, and (2) stochastic inversion of drawdown data obtained with the corrective-filtering method proposed by Trabucchi et al. (2021). The latter allows filtering systematic errors in head data (e.g., external trends of hydraulic heads caused by the normal exploitation of the aquifer) during calibration.

4.3.1 Large-scale long-term cross-hole hydraulic tests

The long-term cross-hole hydraulic test consists of a sequence of three pumping tests performed in different wells and a continuous monitoring of the head responses in multiple observation points. The cross-information derived from the sequential operation of the different wells improves the quality of the information and increases the reliability of the inversion. The equipment consists of three pumping wells operated sequentially in different areas of the domain, starting from November 18th, 2016, and ending in December 31st, 2017 (Figure 4.2). Each pumping well has one injection platform associated (TH01, TH02, TH03) for reinjecting the total amount of brine pumped from the aquifer.

The aquifer response was monitored with 55 pressure transducers. A first set of transducers was installed in August 2016, recording data every thirty minutes. In November 18th, at the beginning of the test, all transducers had already been installed and were recording data for at least a month, allowing getting information about the regional trend. The recording time was set to 30 minutes for the whole period of the hydraulic test. Daily averages of the time series recorded in the observation points are shown in Figure 4.3.

Despite the low historical precipitation, three important rainfall events

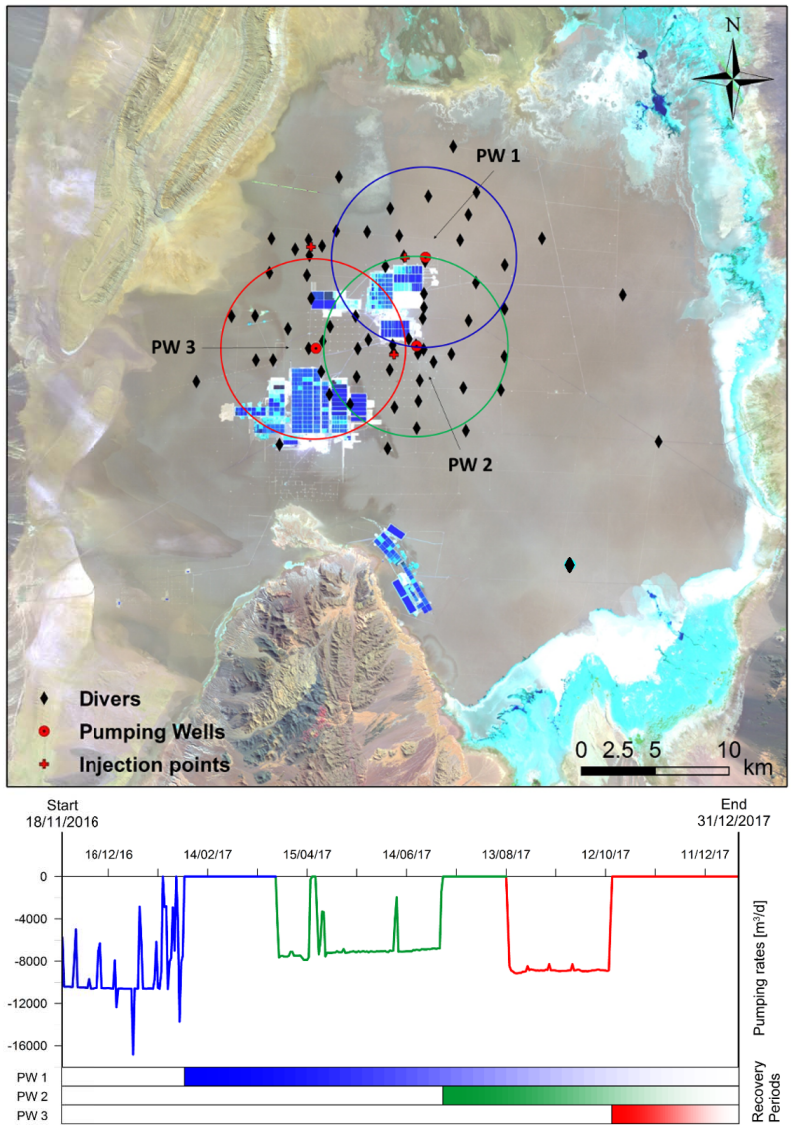

Figure 4.2: Long-term cross-hole hydraulic test. The map displays the location of the three pumping wells (PW1, PW2, PW3), their estimated area of influence and the monitoring network. Below, pumping rates (reverse scale) of the three test versus time. Also highlighted are the recovery period for each pumping well.

occurred in January, February and June 2017, during the hydraulic tests (Figure 4.3). These events were measured with fifteen pluviometers, three located in the nucleus and the rest in the neighboring areas. As expected, given the large extent of the SdA, the magnitude of the precipitation changes from pluviometer to pluviometer. Visual inspection of Figure 4.3 makes it clear that these events cause a significant head rise throught the SdA and must be incorporated in the model. Also apparent in some piezometers are the head drops caused by increases in brine production (Nov.2016 - Feb.2017; Aug.2017 - Nov.2017).

The time evolution of heads displays similar patterns in most piezometers. Data from two corrupted sensors (P20 and P33) was discarded and the weight given to sensors highly influenced by local productions variability (P19 and P27) was significantly reduced.

4.3.2 Drawdown estimation and calibration through stochastic inversion

We calibrated the model using drawdowns rather than heads because we were primarily interested in the identification of transmissivity. One advantage of modeling drawdowns, as opposed to heads, is that they are not sensitive to the magnitude of boundary conditions (heads or fluxes), but only to the type (Neumann, Dirichlet, Cauchy, or others) and to the aquifer hydraulic properties (see, e.g., Trabucchi et al. (2021)), which is why pumping tests are usually interpreted using drawdowns. Another advantage of working with drawdowns is that they are less sensitive to density variations than heads (Ataie-Ashtiani et al., 2001; Slooten et al., 2010). The issue was not critical here because brine density is virtually constant in the modeled portion of the SdA, but might had been if the model had included the not-so-salty edges. Drawdowns are also advantageous in that they are not sensitive to systematic head measurement errors, such surveying elevation errors, and in that initial conditions (zero drawdown) are trivial. But working with drawdowns suffers two relevant drawbacks. First, drawdowns are defined as the difference

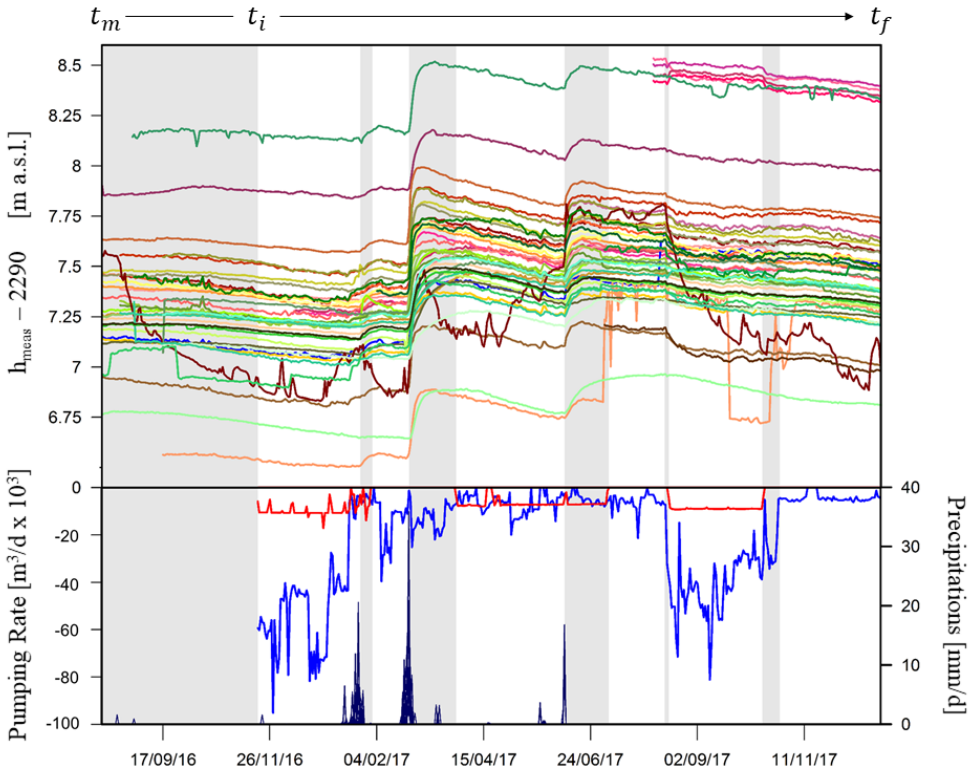

Figure 4.3: Above, daily average of head data recorded with pressure transducers during the hydraulic test period. Below, factors that influenced flow dynamics during the hydraulic test period: 1) the sum of pumping rates of production wells located in the study area (light blue); 2) pumping rates of wells involved in the hydraulic test (red line) and finally rainfall events (dark blue). Finally, every change in the background color (either grey or white) marks a factor change.

between observed and natural heads (natural heads are the ones that would have been observed if the pumping test had not been performed).

Therefore, data filtering is required to separate drawdowns from measured heads, which are affected by natural stresses, boundary effects and complex operational conditions such as those maintained in the SdA. Second, unlike heads, drawdowns do not inform about groundwater flow (where water

comes from or flows to, or most other hydrologically relevant questions), only about hydraulic properties.

Several methods can be used to determine the natural head and calculate drawdowns. Here, we used the method presented by Trabucchi et al. (2021) that allows estimating drawdowns and carrying out the stochastic inversion for aquifer characterization simultaneously. They redefine the estimated drawdown as

$$s_e(\mathbf{x}, t) = h_n(\mathbf{x}, t) - h_m(\mathbf{x}, t) + a(\mathbf{x}), \tag{4.1}$$

where h_n is the natural head obtained by solving the flow natural head model, h_m is the head measured in the field, a is a corrective factor that applies to both h_n and h_m, and s_e is the calculated drawdown to be fitted in the inverse problem.

The advantages of the selected method are that: (1) it describes the natural head conditions through numerical modeling (h_n); (2) accounts for systematic modeling errors as well head measurement errors (a); (3) allows estimating relative fluctuations in the system (s_e) with respect to what we choose to consider as natural head; (4) admits setting much simpler boundary and initial conditions in the drawdown model to be fitted; and finally (5) permits the characterization of the aquifer through stochastic inversion. As the natural heads used to calculate drawdowns depends on the hydraulic parameters, the method implies an iterative process: the parameters estimated through stochastic inversion replace those initially set in the natural head model to run a new iteration until convergence. Thus, in order to apply this method, two groundwater models are required: the natural head model which represents anything but what you consider as part of the hydraulic test, and the drawdown model that simulates aquifer fluctuations due to hydraulic testing and that will be automatically calibrated to estimate the hydraulic properties of the aquifer.

In this work, due to the influence of important rainfall events on the piezometric level, we also considered precipitations as additional hydraulic tests. Still, as the initial production plan of operational wells close to those involved in the hydraulic test changed, we had to consider them as well as part of the tests. Thus, the natural head does not include these stresses, representing instead the head change caused by natural conditions as well as the normal exploitation of the aquifer before t_i = November 18th, 2016. Both natural head and drawdown models are implemented using the finite element code TRANSIN (Medina and Carrera, 2005). Hereafter, the features of each model involved in the application of the method are described.

Natural head model

The model represents the upper hydrogeological units of the SdA nucleus, where we adopt the Dupuit approximation to simulate flow in two dimensions. We discretize the domain using a finite element mesh consisting of 17010 triangular elements of variable sizes (from 100 m, near the pumping centers, to 1000 m at the boundary).

The model simulates heads from July 1st, 2013 until the end of the hydraulic test experiment in December 31st, 2017. Time is discretized with a constant time-step of one day, for a total of 1644 time steps. Boundary conditions are no-flow conditions in the NW and SSW limits, representing the San Pedro formation and the Ignimbrites, respectively. Prescribed heads are imposed otherwise by projecting nearby head observation data in the NE, E and SE marginal zone boundaries. The SW region of the SdA with continuous exploitation is far away from the hydraulic tests. To simplify the system, this region is not explicitly included in the model. Instead, a time-varying prescribed head boundary condition obtained from head observations in the SW limit is used (Figure 4.4).

The initial head condition $h_0(x)$ was determined by an interpolation of available monitoring data collected in July 2013. Recharge is activated for: (1) the rainfall events prior to the experiment, (2) leakage from infiltration ponds,

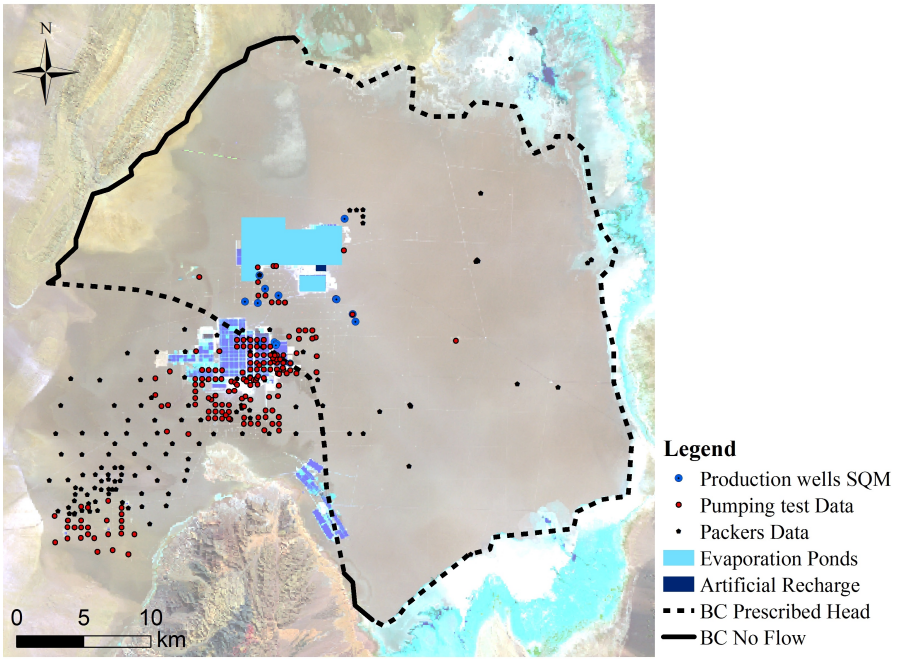

Figure 4.4: Model set up and available hydraulic conductivity data. Boundary conditions, artificial recharge zones and pumping wells considered in the model are shown. The location of K data shared by SQM obtained from pumping test of short duration and packers are also shown.

and (3) the areas of artificial recharge (Figure 4.4). Rainfall recharge is assumed homogeneously distributed in the whole domain, except for the evaporation ponds artificial recharge areas, where the infiltration rate is homogeneously distributed in the space within each zone and its variation through time is defined by three different time functions. Finally, production wells operating from July 1st, 2013 to November 18th, 2016 are modeled as point extractions whose flow rates change over time.

After each simulation of the natural head model h_n, the bias correction term a was calculated at each observation point by fitting the model $h_n + a$ to head measurements h_m by least squares regression. Head measurements taken at times close to t_i were strongly weighted in the regression (10 times larger than the rest). After this, the estimated drawdown at each observation

point was estimated through equation (4.1).

Drawdown model

This flow model simulates the fluctuation history of drawdowns during the hydraulic test period that took place over 408 days, from November 18th, 2016, to December 31st, 2017. Geometry, spatial discretization, and parameter zonation coincide with those set in the previous model. The time is discretized with a constant time-step increment of one day, for a total of 408 time steps.

Applying the superposition principle, initial and boundary conditions are easily set to zero (Trabucchi et al., 2021). The long-term cross-hole hydraulic test and production pumping rates are simulated by prescribing a time-varying flow rate at each well. The recharge of each rainfall event considers the spatial distribution of precipitation and a time-dependent transfer function relationship between precipitation and recharge. To do this, the recharge is represented by a linear combination of spatial and temporal functions,

$$r(\mathbf{x}, t) = f_1(\mathbf{x})F_1(t) + f_2(\mathbf{x})F_2(t) + f_3(\mathbf{x})F_3(t). \tag{4.2}$$

Each term represents a different precipitation event. The spatial distribution of recharge $f_i(\mathbf{x})$ is estimated by cokriging the precipitation data of the rainfall event obtained from two different sources of information: punctual precipitation obtained with pluviometers and MODIS temperature obtained at the scale of one km from satellite information. Prior to the application of cokriging, the temperature measurements from MODIS were translated into precipitation by applying the following relationship that best fitted the pluviometer precipitation measurements with MODIS temperature at the same location,

$$\log P = 1.134 \log(4.5 - \Delta T) + 0.4577, \qquad P \geq P_0, \tag{4.3}$$

where ΔT is the deviation of the temperature in each pluviometer from the daily mean. Only the precipitation larger than $P_0 = 2$ mm was assumed to contribute to recharge. The precipitation maps express that rainfall events relate to the Bolivian winter coming from the Andes. The time function is determined by considering that an instantaneous rainfall event described by $p(t) = \delta(t)$ translates into an exponential recharge time function g(t),

$$g(t) = \alpha e^{-\alpha(t-t_0)}, \tag{4.4}$$

characterized by an infiltration attenuation rate coefficient, $\alpha = 1/3$ d^{-1}, and a recharge time-lag in the unsaturated zone, t_0. Since precipitation occurs over several days, the resulting recharge can be obtained by the principle of superposition, which determines that the final recharge $r(t)$ is the convolution of precipitation over the function $g(t)$

$$F_i(t) = \int_0^t p_i(\tau) g(t-\tau) d\tau, \tag{4.5}$$

where $p(\tau)$ is the normalized rain rate that satisfies that $F_i(t)$ is a unitary function.

Parametrization and geostatistical models

The two flow models share the same parametrization. We distinguished six different zones for representing the spatial distribution of permeability and storage coefficient (Figure 4.5). We refer to them as East and West geobodies, FS1, FS2, FS3, and SW area. The first two zones describe the East and West region of the Salar with respect to the main fault. FS1, FS2, and FS3 divide the main fault into three separate regions, and the SW area represents the boundary region near the production area of the Salar nucleus. The spatial distribution of the decimal log of the hydraulic conductivity $Y(\mathbf{x})$ in the East and West geobodies is heterogeneous and represented by independent random fields. The other zones in the model (FS1, FS2, FS3, SW) are assumed

homogeneous and represented by a single hydraulic conductivity value. The storage coefficient S is assumed constant in each of the sixth zones.

A reliable variogram model of the decimal log of hydraulic conductivity $Y(\mathbf{x}) = \log K(\mathbf{x})$ was difficult to infer from available data in each geobody. However, the variogram model associated with the entire aquifer based on pumping test data of short duration seems to follow an isotropic spherical random function model characterized by a range of 7962 m, a sill of 0.9, and a nugget of 0.3 (Figure 4.6).

Since other interpretations can be considered due to variogram uncertainty, we considered other possible variogram characterized by an anisotropic

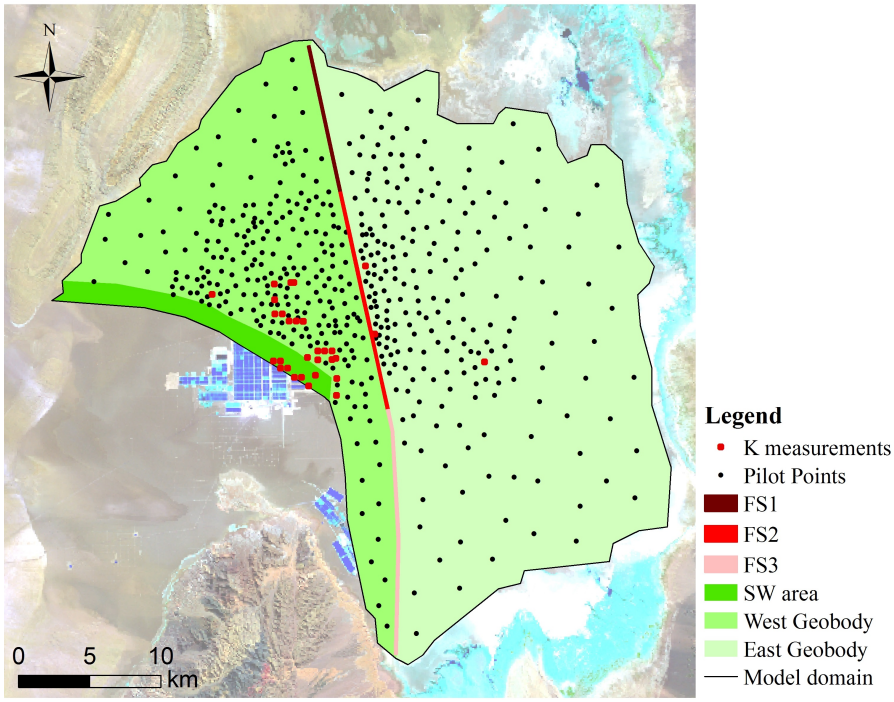

Figure 4.5: Model parametrization: the six zones defined for representing the spatial variability of K are shown. Also, the location of pilot points distributed in both the East and West Geobody and that of conditioning measurements (K measures) is shown.

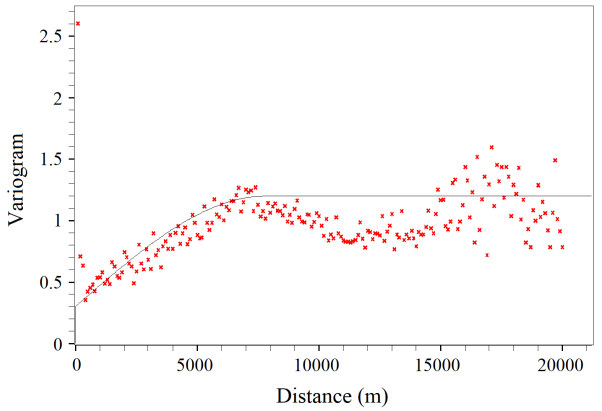

Figure 4.6: Experimental and estimated variogram calculated using the hydraulic conductivity data obtained from pumping tests of short duration in both the East and West Geobody (shallow aquifer).

spherical variogram function with a minimum and maximum range of 4000 m and 7962 m, respectively. The maximum range was oriented along the ENE-WSW direction to represent the potential presence of preferential flow paths developed over time from the nucleus to the eastern region. This was suggested by independent data (see section 4.4.2). Based on this, we considered that three different geostatistical models can equally represent the heterogeneous structure of the SdA. These models were obtained by assigning the estimated variograms to the different geobodies. A summary of the adopted

Table 4.1: Parameters of geostatistical models set to apply the inverse problem with pilot points.

	Model	Geobody	Min. Range [m]	Max. Range [m]	Anisotropy Direction [°]
Isotropy	1	East	7962	7962	-
	1	West	7962	7962	-
Anisotropy	2	East	4000	7962	70
	1	West	4000	7962	70
Isotropy / Anisotropy	3	East	4000	7962	70
	1	West	7962	7962	-

geostatistical models is provided in Table 4.1.

Calibration using drawdown data

We chose to couple the drawdown model with the regularized pilot point method developed by Alcolea et al. (2006) to estimate the spatial distribution of hydraulic conductivity in the SdA conditioned to drawdowns and permeability data. The method is a modification of the pilot point method (de Marsily et al., 1984) and can be used for both conditional estimation CE and conditional simulation CS (Alcolea et al., 2008). The method consists in estimating the hydraulic properties at a set of arbitrary points (pilot points PP) to best fit the observations and the spatial variability patterns through the solution of the geostatistical inverse problem. In our case, the application of the method considered the following main features:

- The spatial distribution of the decimal log of the hydraulic conductivity $Y(\mathbf{x})$ in each geobody is represented by the combination of a drift field $Y_D(\mathbf{x})$ and an uncertain residual field $\Delta Y(\mathbf{x})$. The drift field is obtained through both conditional estimation (CE) and conditional simulation (CS) of $Y(\mathbf{x})$. The residual field can be seen as the perturbation of $Y_D(\mathbf{x})$ required to better fit measurements of dependent variables (i.e., drawdown data). It is expressed as a linear combination of unknown model residuals at pilot point positions,

$$Y(\mathbf{x}) = Y_D(\mathbf{x}) + \Delta Y(\mathbf{x}) = Y_D(\mathbf{x}) + \sum_{j=1}^{N_p} \lambda_j^P \Delta Y_j, \tag{4.6}$$

  where N_p is the number of pilot points, ΔY_j is the perturbation of Y at the jth pilot point position, and λ_j^P are the kriging weights of ΔY. The model residuals at pilot point positions are unknown model parameters. A total of 445 pilot points were distributed in these two zones (Figure 4.5)

with higher density in regions where more measurements and observations were available. The large number of pilot points used allowed the identification of the spatial patterns with high resolution.

- The objective function to be minimized during calibration can be written as

$$F(\mathbf{p}, \mathbf{a}) = F_s + \lambda F_p, \tag{4.7}$$

where

$$F(\mathbf{p}, \mathbf{a}) = (\mathbf{s}(\mathbf{p}) - \mathbf{s}_e)^t \mathbf{V}_s^{-1} (\mathbf{s}(\mathbf{p}) - \mathbf{s}_e) + \lambda (\mathbf{p}_m - \mathbf{p})^t \mathbf{V}_p^{-1} (\mathbf{p}_m - \mathbf{p}). \tag{4.8}$$

Here, $\mathbf{p}$ is the vector of model parameters, and $\mathbf{V}_s$ and $\mathbf{V}_p$ are the covariance matrices of errors in drawdown and prior information of the parameters, respectively. The model parameters used for calibration were the pilot point residuals $\{\Delta Y_1, ..., \Delta Y_{N_p}\}$, the hydraulic conductivity of the FS1, FS2, FS3, and SW zones, and the storage coefficient of each zone. In the definition of the objective function, λ is the plausibility term, which is essentially a criterion that regulates the variation of the model parameters from their corresponding prior estimate. We considered different values of the plausibility term (λ = 1, 0.1, 0.01). The calibration did not converge for smaller λ values. We assigned a high standard deviation (low weight) to points P27 and P33 because of data inconsistencies, and to point P19 and P20 because they displayed severe fluctuations caused by the MOP production wells on head fluctuations. All other observations had a unitary standard deviation.

- As the lowest objective function does not necessary mean best model solution, the optimum value of λ has to be finally chosen as the one that yield the maximum of the expected likelihood, i.e. the minimum of the support function S_2 (Medina and Carrera, 2003), reads

$$S_2 = N + \ln|\mathbf{H}| + N\ln\frac{F}{N} - \sum_j k_j \ln\mu_j \tag{4.9}$$

where N is the number of available data (both measurements and prior estimates of model parameters), $\mathbf{H}$ is the first order approximation of the Hessian of the total objective function F, k_j is the number of data of the parameter type j and μ_j is the weighting scalar for the parameter (i.e. λ).

The corrective-filtering method

The corrective-filtering method of Trabucchi et al. (2021) was used to obtain reliable estimates of drawdown data. In this case, the method requires to first estimate drawdowns with the natural flow model and then calibrate the parameters to fit drawdown estimates with the pilot point method. The parameters obtained are then used to simulate natural heads, which lead to new drawdown estimates to re-calibrate model parameters. The process is repeated until convergence. To initialize this iterative process, we set the hydraulic conductivity and storage coefficient to a constant value equal to $K = 430$ m/d, i.e., geometric mean of available K measurements in the upper aquifer, and $S = 0.05$ (UPC-CSIC, 2015), respectively. Once reliable estimates of drawdown data were calculated with the geostatistical model 1 through conditional estimation, we carried out further calibrations, changing the geostatistical model and performing both CE and CS.

4.4 Model results

4.4.1 Calibration and identification of flow connectivity structures

Several metrics are used to analyze the goodness of the calibrated model. For each case, we report (1) the support function S_2 as defined by Medina and Carrera (2003) as minus two times the expected likelihood, (2) the total objective function F, and (3) the drawdown contribution to the objective function

F_s in Table 4.2. In all cases, the objective function decreases with the plausibility factor λ because higher freedom is given to the model. This leads to the better fitting, but not necessarily to better solution in terms of the hydraulic conductivity field (Alcolea et al., 2006). For that purpose, we consider the values of the support function S_2. Here, S_2 and F show a minimum value when $\lambda = 0.01$ in all cases. We conclude that the six different scenarios considered reach the best solution for λ=0.01. Note that all calibrated models reach similar values of S_2 and F. This means that all scenarios and calibrated parameters can equally represent the system with similar reliability, which illustrates the non-uniqueness of the inverse problem in this case.

Figure 4.7 compares the time evolution of measured drawdowns to those simulated with the geostatistical model 1 through conditional estimation for $\lambda = 0.01$ with measurements estimated through equation (4.1). Due to the large number of observations, just a number of spatially representative points are shown. It is quite clear that the aquifer response is well captured everywhere in the domain with centimeters precision. The contribution of the objective function to each observation point (shown at the top of each figure) is impressively small in most observations given the large area of the domain. The best fit corresponds to P12 with a mean error of 1×10^{-2} m, the worst calibrated point is P63 with a mean error of 5.5×10^{-2} m. The different responses to rainfall events (highlighted in the figure by a thick background gray color) are well reproduced both in terms of magnitude and recovery slope. Still, the influence of the pumping wells is well captured. This can be especially appreciated in the second half of the hydraulic test period, with the activation of the third well in the NW zone. The strong decrease of the production, with a consequent recovery of the aquifer is also well captured in most observation points.

Estimated spatial distributions of hydraulic conductivity in the East and West geobodies are shown in Figure 4.8 for all cases and $\lambda = 0.01$. The

Table 4.2: Results of the stochastic inversion for six different test problems (for CE, test problems from 1 to 3; for CS test problems from 4 to 6). For each calibrated model, the final objective functions and support function S_2 are presented. Hydraulic parameters estimated applying the traditional inverse problem are also shown for each calibrated zone.

			Objective Function			Hydraulic conductivity estimation [m/d]				Storage coefficient estimation [-]				
	Geost. Model	λ	Total	Drawdown	S_2	SF1	SF2	SF3	SW zone	SF1	SF2	SF3	East Geobody (+ SW zone)	West Geobody
Conditional Estimation	1	0.01	18.07	15.83	$-1.18 \cdot 10^5$	$1.17 \cdot 10^6$	$4.20 \cdot 10^7$	$3.02 \cdot 10^5$	$6.90 \cdot 10^2$	0.10	0.10	0.10	0.06	0.04
		0.1	28.15	20.07	$-1.09 \cdot 10^5$	$6.04 \cdot 10^4$	$8.05 \cdot 10^6$	$3.70 \cdot 10^5$	$1.01 \cdot 10^3$	0.10	0.12	0.11	0.06	0.04
		1	70.43	35.03	$-8.98 \cdot 10^4$	$5.76 \cdot 10^4$	$1.17 \cdot 10^6$	$1.43 \cdot 10^5$	$3.35 \cdot 10^3$	0.11	0.17	0.10	0.06	0.03
	2	0.01	17.90	15.72	$-1.19 \cdot 10^5$	$8.12 \cdot 10^5$	$1.45 \cdot 10^7$	$5.78 \cdot 10^5$	$8.73 \cdot 10^2$	0.10	0.11	0.10	0.06	0.04
		0.1	27.25	19.23	$-1.09 \cdot 10^5$	$4.84 \cdot 10^4$	$7.54 \cdot 10^6$	$5.65 \cdot 10^5$	$9.64 \cdot 10^2$	0.10	0.13	0.11	0.06	0.04
		1	68.53	33.60	$-9.04 \cdot 10^4$	$5.02 \cdot 10^4$	$1.29 \cdot 10^6$	$1.41 \cdot 10^5$	$3.15 \cdot 10^3$	0.11	0.17	0.10	0.05	0.03
	3	0.01	18.58	16.36	$-1.18 \cdot 10^5$	$5.61 \cdot 10^5$	$1.61 \cdot 10^7$	$1.33 \cdot 10^6$	$7.67 \cdot 10^2$	0.10	0.11	0.10	0.06	0.04
		0.1	28.28	19.60	$-1.09 \cdot 10^5$	$8.34 \cdot 10^4$	$9.35 \cdot 10^5$	$4.07 \cdot 10^6$	$1.04 \cdot 10^3$	0.10	0.12	0.11	0.06	0.04
		1	70.44	34.53	$-8.98 \cdot 10^4$	$5.25 \cdot 10^4$	$8.12 \cdot 10^5$	$1.69 \cdot 10^5$	$3.82 \cdot 10^3$	0.11	0.17	0.10	0.05	0.03
Conditional Simulation	1	0.01	16.25	13.72	$-1.21 \cdot 10^5$	$5.54 \cdot 10^3$	$3.46 \cdot 10^3$	$1.02 \cdot 10^6$	$8.46 \cdot 10^2$	0.10	0.11	0.10	0.05	0.04
		0.1	24.08	18.50	$-1.12 \cdot 10^5$	$4.35 \cdot 10^5$	$4.68 \cdot 10^6$	$3.90 \cdot 10^5$	$9.383 \cdot 10^2$	0.10	0.11	0.11	0.05	0.05
		1	46.77	26.79	$-9.81 \cdot 10^4$	$4.91 \cdot 10^4$	$8.80 \cdot 10^5$	$5.51 \cdot 10^4$	$1.92 \cdot 10^3$	0.10	0.17	0.11	0.06	0.03
	2	0.01	16.82	15.21	$-1.20 \cdot 10^5$	$4.92 \cdot 10^5$	$5.86 \cdot 10^6$	$2.87 \cdot 10^6$	$1.07 \cdot 10^3$	0.10	0.10	0.10	0.05	0.04
		0.1	21.83	17.43	$-1.14 \cdot 10^5$	$2.29 \cdot 10^4$	$5.42 \cdot 10^6$	$9.19 \cdot 10^4$	$8.96 \cdot 10^2$	0.10	0.12	0.10	0.06	0.04
		1	43.27	26.00	$-9.96 \cdot 10^4$	$6.65 \cdot 10^4$	$2.16 \cdot 10^5$	$1.42 \cdot 10^5$	$3.84 \cdot 10^3$	0.11	0.28	0.11	0.05	0.03
	3	0.01	15.51	13.14	$-1.22 \cdot 10^5$	$3.02 \cdot 10^4$	$3.80 \cdot 10^3$	$1.29 \cdot 10^6$	$6.10 \cdot 10^2$	0.10	0.10	0.10	0.05	0.04
		0.1	28.18	20.42	$-1.09 \cdot 10^5$	$1.12 \cdot 10^4$	$2.54 \cdot 10^3$	$4.03 \cdot 10^5$	$5.92 \cdot 10^2$	0.09	0.11	0.11	0.05	0.04
		1	47.63	27.16	$-9.77 \cdot 10^4$	$4.67 \cdot 10^4$	$4.11 \cdot 10^4$	$6.25 \cdot 10^4$	$2.38 \cdot 10^3$	0.10	0.20	0.10	0.05	0.03

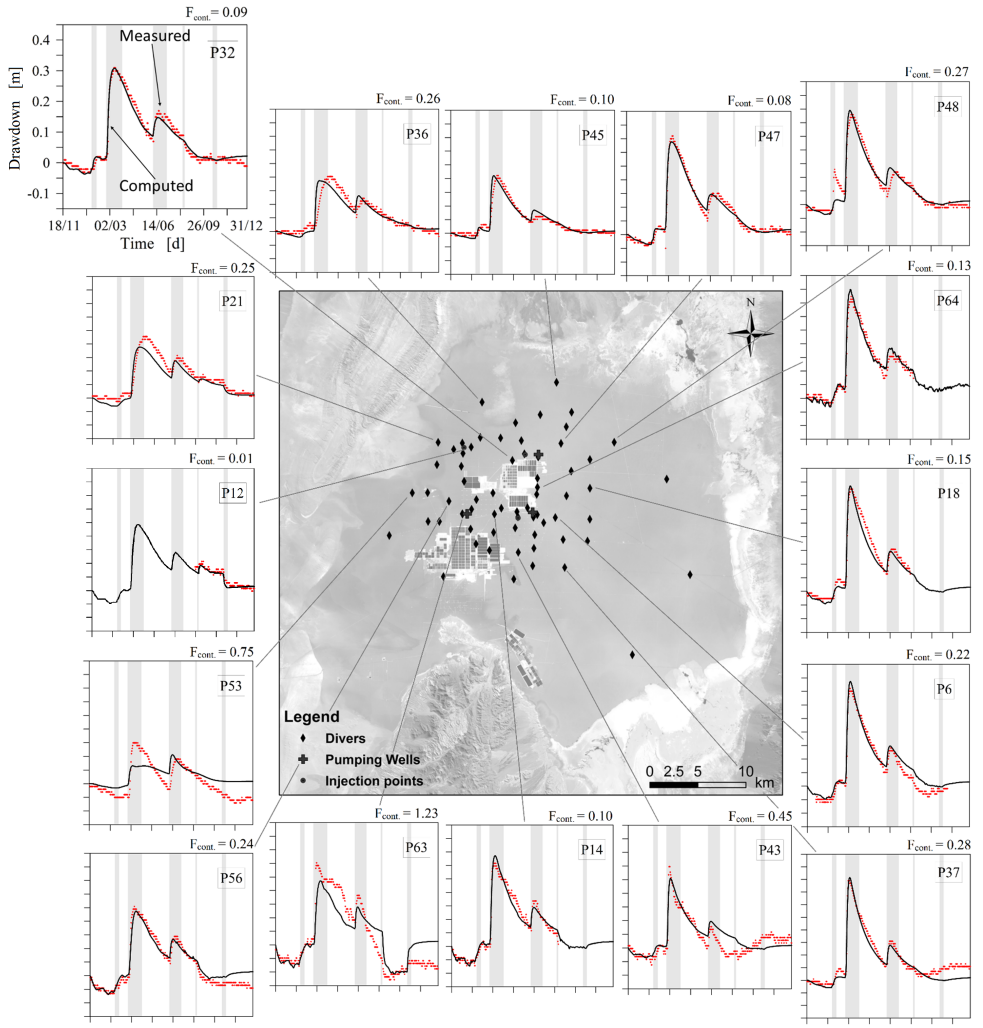

Figure 4.7: The calibration results are presented in terms of calculated and measured relative heads vs. time for a selected number of observation points. For each point, the contribution to the objective function is reported in the upper part of the graph. Still, every change in the background color (either grey or white) marks some hydraulic factor change (either precipitation, production or hydraulic test changes).

other estimated parameters are summarized in Table 4.2. In all cases, the estimated hydraulic conductivity vary orders of magnitude, ranging from approximately 10^{-3} to 10^{5} m/d in CE calibrations. As expected, conditional estimation maps of hydraulic conductivity are far smoother than those obtained by conditional simulation because the latter represent the small-scale spatial variability of the hydraulic conductivity. In general, conditional estimation results show two or three high permeability structures. One is always located in the West Geobody, which coincides with the Chascona fault zone (Figure 4.1), and another located in the East Geobody, which does not apparently correspond to any known geological feature. The latter is split into two narrower high permeability bodies when the heterogeneous structure of the West geobody follows an anisotropic structure. The orientation and shape of this structure depends on the geostatistical model. It is oriented along the South-East direction when the heterogeneous structure of the West geobody is isotropic and WSW-ENE when an anisotropic structure is considered. In any case, results suggests the presence of a large preferential flow channel that connects the nucleus with the groundwater recharge boundary. The estimated values of the Salar fault zones range between 10^{4} and 10^{6} m/d. This high values indicate that the Salar fault zone behaves as a well-developed karst system (Houston et al., 2011). The calibrated storage coefficient is about 0.1 in the Salar Fault, and 0.06 and 0.04 in the east and west geobodies, respectively. Conditional simulation results show similar patterns but preferential channels exhibit more variability in terms of location and higher hydraulic conductivity values. From this, results indicate that even though the long-term large-scale hydraulic test coupled with the stochastic inverse problem and the corrective-filtering method is capable to identify the presence of large-scale flow connectivity structures, the actual position of these channels is still quite uncertain.

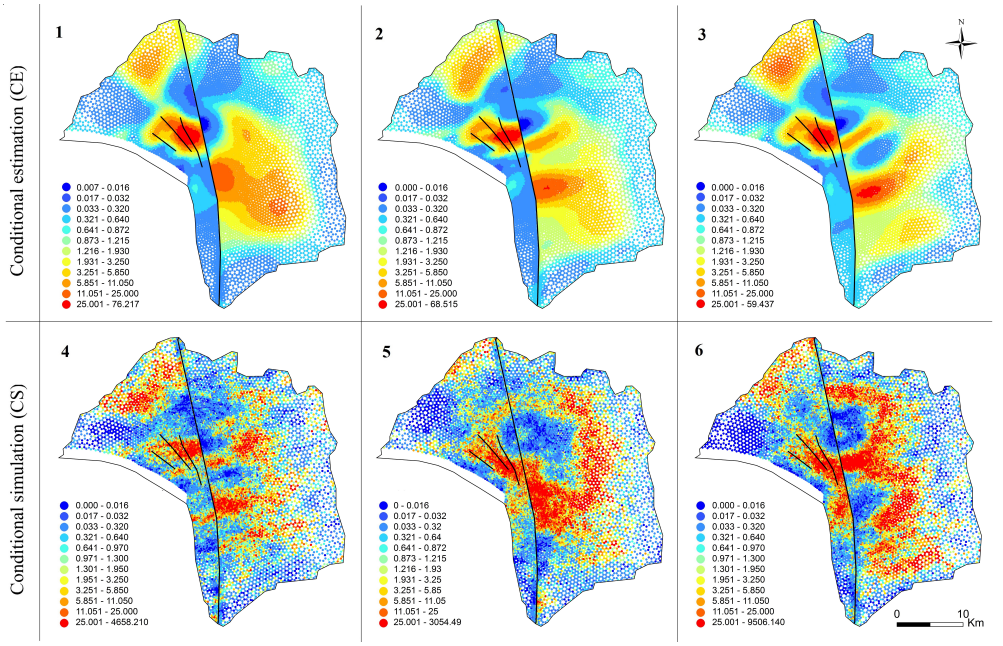

Figure 4.8: Normalized estimates of hydraulic conductivity fields. Above, conditional estimation results for test problem 1, 2 and 3. Below, conditional simulation for test problems 4, 5 and 6. For each geostatistical model, the best result among those obtained by changing the plausibility term (λ) is presented.

4.4.2 Comparison with independent data

In this section, we compare the calibration results with independent data. The objective is to demonstrate that the preferential channels identified during calibration are logical and consistent with isotopic data, mixing ratios, geophysical data, and the response of heads to rainfall events. This gives higher confidence to our results and provides further insights about the dynamics of the system. For comparison purposes, figure 4.9 shows a summary of the results with multiple plots. Geophysical studies performed by SQM have indicated that the study area includes the Salar and the Chascona faults (see Figure 4.1). While the former (SF) was explicitly described in the model, the Chascona faults were not. Yet, the spatial distribution of the hydraulic conductivity in

the West geobody in all calibrated models display a highly permeability area in the Chascona faults. This is highlighted in Figure 4.9, where the Chascona faults are overlapped with the calibrated map of hydraulic conductivity obtained with the goestatistical model 1 and $\lambda = 0.01$ through conditional estimation and conditional simulation.

The isotopic measurements $\delta^{18}O$ reported by Huerta (2012) are also shown in Figure 4.9 with corresponding contour lines. The general trend suggests that brine becomes increasingly heavier when groundwater moves from the eastern marginal region towards the nucleus probably due to intensive evaporation occurring in the marginal zone. Data permits to delineate a narrow ENE-WSW oriented zone of lighter brine that migrates towards the nucleus. However, a smaller area, NW-SE oriented, is visible in the southeastern region with similar values as those characterizing the center-eastern part of the domain. This suggests lower transit times along this region, if compared with the surroundings, and thus highly permeable features such as those identified during model calibration.

We also performed an end-member mixing analysis of hydrochemical data to evaluate recharge sources and identify reaction processes in the SdA. To do this, we used the method developed by Carrera et al. (2004), which incorporates the uncertainty in end-member concentrations. The method is implemented in the free software MIX. A total of 57 brine samples taken from the upper aquifer and located in the NE zone of the nucleus were used, having concentrations of Mg, Li, SO_4, H_3BO_3, Cl, Na, K and Ca. A principal component analysis of the concentrations revealed that two eigenvalues can explain 87% of the data variability. Based on this, we selected 3 end-members. Two end-members represent the entrance of groundwater from the East and North boundaries of the Salar. The other end-member describes a strongly evaporated brine in the Salar nucleus. From this, the likelihood function is maximized to estimate mixing ratios and end-members. Figure 4.9 shows the contour lines of the mixing ratio associated with groundwater recharge coming from the North (α_N) and from the East (α_E) as well as their corresponding

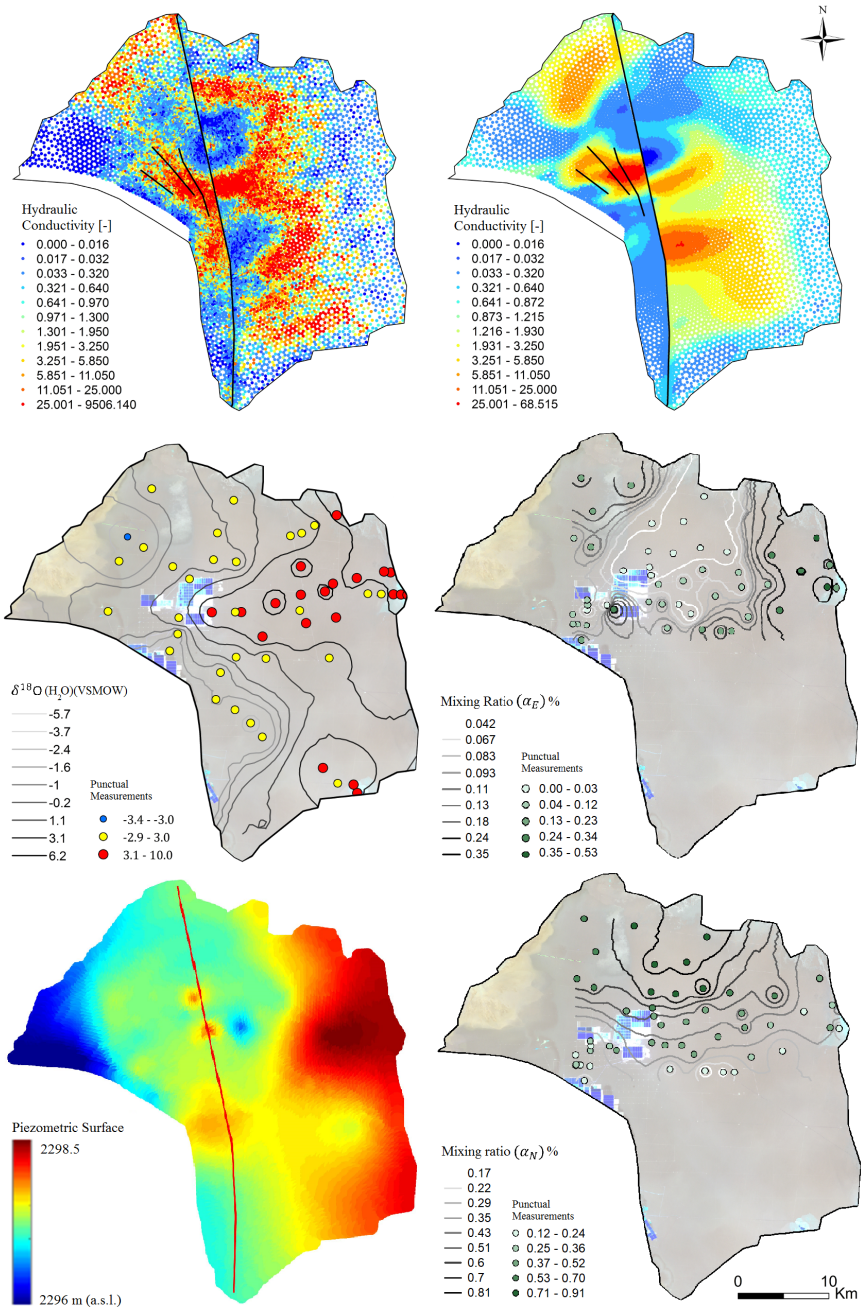
Hydraulic Conductivity [-]
0.000 - 0.016
0.017 - 0.032
0.033 - 0.320
0.321 - 0.640
0.641 - 0.970
0.971 - 1.300
1.301 - 1.950
1.951 - 3.250
3.251 - 5.850
5.851 - 11.050
11.051 - 25.000
25.001 - 9506.140
Hydraulic Conductivity [-]
0.000 - 0.016
0.017 - 0.032
0.033 - 0.320
0.321 - 0.640
0.641 - 0.872
0.873 - 1.215
1.216 - 1.930
1.931 - 3.250
3.251 - 5.850
5.851 - 11.050
11.051 - 25.000
25.001 - 68.515
N
δ18O (H2O)(VSMOW)
-5.7
-3.7
-2.4
-1.6
-1
-0.2
1.1
3.1
6.2
Punctual Measurements
-3.4 - -3.0
-2.9 - 3.0
3.1 - 10.0
Mixing Ratio (αE) %
0.042
0.067
0.083
0.093
0.11
0.13
0.18
0.24
0.35
Punctual Measurements
0.00 - 0.03
0.04 - 0.12
0.13 - 0.23
0.24 - 0.34
0.35 - 0.53
Piezometric Surface
2298.5
2296 m (a.s.l.)
Mixing ratio (αN) %
0.17
0.22
0.29
0.35
0.43
0.51
0.6
0.7
0.81
Punctual Measurements
0.12 - 0.24
0.25 - 0.36
0.37 - 0.52
0.53 - 0.70
0.71 - 0.91
0
10
Km

point measurements. Results indicate the presence of a mixing front moving along the East-West direction that divides the system into two zones: the northern region, richer in norther brine, and the southern region, richer in eastern brine. In agreement with the calibrated hydraulic conductivity maps, the latter is oriented along the East-West direction and suggests the presence of a highly permeable zone that connects the east boundary with the Salar nucleus with minor transit times.

We generated aquifer piezometric surfaces directly from the head measurements recorded during the hydraulic test to analyse the spatial and temporal evolution of the aquifer response. For this, we used ordinary kriging with measurement uncertainty. One time-lapse is presented as an example in Figure 4.9. Results show that the hydraulic gradient and the flow direction can substantially vary over space. The production area is concentrated on the South-West of the Salar and should mostly affect gradient differences in the western region. Contrary, head dynamics in the eastern region are mostly controlled by the heterogeneous structure of the aquifer and fluctuations of boundary heads. Knudby and Carrera (2006) argued that hydraulic diffusivity is a good indicator of both flow and transport connectivity. In this context, the piezometric surface shown in figure 4.9 represents the situation immediately after a rainfall event, where high boundary heads diffusing fast suggest

Figure 4.9: (Previous page.) Comparison of estimated hydraulic conductivity fields with independent data. Above, 1) normalized permeability fields associated to the lowest objective function for both CE (left) and CS (right). The Chascona Faults are also plotted for comparison purposes. On the left, in the middle, 2) punctual data (dots) and interpolated data (contours) of the isotopic deviation $\delta^{18}O$ are plotted (modified from Huerta (2012)). On the left, below, 3) piezometric surface of the SdA shallow aquifer after the precipitation event of February. On the right, in the middle, 4) interpolated data of mixing ratio of the brine entering from the east side. Dots refer to the location of geochemical samplings. On the right, below, 5) interpolated data of mixing ratio of the brine coming from the north side. Dots refer to the location of geochemical samplings.

the presence of a preferential flow channel. This agrees with the high permeability region identified in the east geobody during calibration as well as with isotopic data and mixing ratios.

4.4.3 Scale effect of the hydraulic conductivity

As initially pointed out by Brace (1980, 1984) and remarked by Clauser (1992), the increase of the aquifer volume investigated (whether it is made of crystalline or sedimentary rocks) typically leads to an increase of the estimated permeability. This scale effect strongly depends on the connectivity of highly permeable structures (Sanchez-Vila et al., 1996) and it is a natural consequence of heterogeneity. Several authors have examined the scale effect in porous, fractured and karst media (Clauser, 1992; Rovey II., 1998; Schulze-Makuch et al., 1999; Neuman and Di Federico, 2003; Martinez-Landa and Carrera, 2005, among others). In this context, it is interesting to contrast the hydraulic conductivity values obtained through model calibration against the different measures of hydraulic conductivity obtained at different scales.

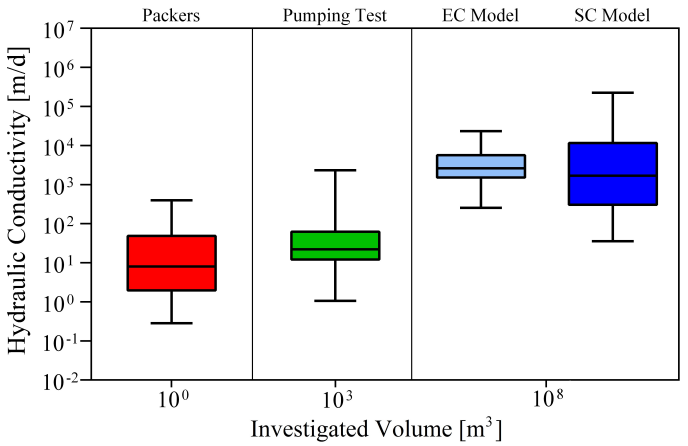

Figure 4.10: Scale effect of the hydraulic conductivity. Boxplots limits correspond to the 95% confidence interval.

For this purpose, we compare the hydraulic conductivity values estimated with packers and single-hole hydraulic tests with those determined from pumping tests and the stochastic inverse model. Data is presented in Figure 4.10 through box plots ordered in increasing scale. We can clearly observe a strong scale effect of the hydraulic conductivity. We note that almost two orders of magnitude separate packers and short-term pumping tests from model calibration. This pronounced scale effect suggests that the SdA nucleus is mostly characterized by preferential flow channels that control the dynamics of the aquifer at a large scale. This also suggests that karst development is probably generalized throughout the entire domain.

4.5 Conclusions

We have carried out a large-scale cross-hole hydraulic test in the SdA evaporitic aquifer (brine reservoir). Head fluctuations have been observed throughout the domain for more than a year, during which additional responses related to external flow dynamics (rainfall, production wells) have been also recorded. After filtering head observations to obtain drawdowns, we have developed a flow model and applied the geostatistical inversion with three main purposes: 1) to assess if data recorded during this long hydraulic test, jointly with the application of the stochastic inversion, make it possible to characterize the heterogeneity over a tens of kilometers karst aquifer and, in particular, 2) if the stochastic approach is capable of identifying connectivity patterns at a large scale, and 3) to assess the scale effect caused by preferential flow paths. With these purposes in mind, we can conclude that:

1. The combined application of a long-lasting large-scale hydraulic test and the stochastic inversion allowed us to investigate an evaporitic aquifer of great extension and to reach a good understanding of the spatial variability of the hydraulic conductivity.

2. In the specific, regarding the cross-hole hydraulic test, head variations recorded during the test show that the main dynamics affecting the

piezometric level are the precipitation events (completely unexpected, given the hyper-aridity conditions of the area) and the exploitation changes. Moreover, since these processes occurred most of the times in correspondence with a variation in the cross-hole test, we detect a slight response of the aquifer to the hydraulic test itself. Still, including all these factors in the definition of the drawdown, has allowed us to identify the hydraulic properties of the aquifer.

3. Still, the stochastic inverse problem conditioned to detailed cross-information of aquifer head responses has been capable to identify the presence of preferential channels zones at the scale of tens of kilometres. The exact delineation of these structures has not been possible.

4. In fact, different test problems (differences in terms of geostatistical model, plausibility term and generation of $f_D(x,t)$) lead to the same quality of the results. We obtain quite good fittings in all the calibrated models (Table 4.2): the application of CS leads to slightly better results than those from the use of CE (as hoped). Still, the aquifer response is well captured in all the runs. Therefore, these results should be viewed as equally probable estimated K fields, despite the non-uniqueness of the stochastic inversion.

5. These K fields are consistent with available independent data proceeding from different sources, which lends support to the characterization process, allowing a step forward in the understanding of connectivity structures involved in the aquifer behaviour. In fact, the main high conductivity zones have been found consistent with information based on isotopes and mixing ratios, as well as piezometric and geophysics data.

6. Furthermore, preferential flows results in a marked scale effect. Comparison of estimated model parameters with local measurements showed that the hydraulic conductivities are about 30 times larger than those estimated from local scale pumping tests, and more than two orders of magnitude larger than those obtained from packer tests, which reflect a even smaller scale than pumping tests. This conclusion suggests that

karst development is probably generalized throughout the Salar, controlling the large scale hydraulic conductivity.

Chapter 5

Evaluation of wormhole formation dynamics in an intermediate-scale dissolution experiment: Hydraulic and transport effects

5.1 Introduction

Mineral dissolution produces time-dependent highly conductive flow channels known as wormholes that control flow dynamics and solute transport behaviour in soluble porous, fractured and karst media (de Marsily, 1985). In karst aquifer systems, dissolution patterns strongly influence the morphology and location of main flow paths (Daccord, 1987; Groves and Howard, 1994), and control cave development long before channels reach explorable dimensions (Daccord, 1987; Groves and Howard, 1994; Li et al., 2019; Cabeza et al., 2020). In this context, a better understanding of wormhole dynamics is seen crucial for characterizing karst aquifers such as those encountered in the Salt Flats of the central Andes (e.g., Salar de Uyuni, Salar de Atacama and Salinas Grandes, among others). These geological formations are unique and valuable both from an environmental and an economic point of view, as they host natural reserves (e.g., Los Flamencos National Reserve) and mobile mineral resources (e.g., lithium for batteries) in the brine (Kesler et al., 2012; Vikström et al., 2013). In these systems, aquifer architecture and conductive features that control hydraulic and transport behavior strongly condition their environmental protection and economic development (Chapter 4). Thus, a deep understanding of the evolution of dissolution patterns is key for the preservation of these systems. Wormhole dynamics is also important in a large variety of problems. In Carbon Capture and Sequestration (CCS), dissolution patterns are recognized as a possible failure mode. The safety of storage due to CO_2 leakage through the caprock can compromise the geological trap (Lombard, J.M. et al., 2010; Luquot et al., 2014; Kampman et al., 2014; Selvadurai et al., 2017). In oil and gas fields, stimulation treatments with acid injection are often employed to enhance oil and gas recovery (EOR). The development of wormholes around the wellbore produces high permeability channels for the oil to bypass the damage zone (Fredd and Fogler, 1998; Bazin et al., 2001; Cohen et al., 2008). However, oil and gas production can also be negatively affected by long conductive channels developed between injectors and producers. During waterflooding, important amounts of oil is typically lost as

water mainly flows through conductive channels, bypassing large amounts of crude oil (Hoefner and Fogler, 1988).

When a geological system is not in thermodynamic equilibrium, fluid-rock interaction can lead to the dissolution of mineral phases, changing the secondary porosity of fractured or porous rocks (Steefel and Lasaga, 1994; Jamtveit and Meakin, 1999). Starting from an almost homogeneous front (unpatterned state), well-ordered dissolution structures (patterned state) can form and develop at different spatial and temporal scales (Ortoleva et al., 1987). Dissolution patterns characterized by preferential flow-paths may form without the intervention of external agents by the so-called self-organization mechanism (Ortoleva et al., 1987; Steefel and Lasaga, 1994; Renard et al., 1998). The triggering factors are small rock imperfections (areas of instability) nearby the dissolution front. The amplifying factor is the positive feedback loop generated by geochemical and hydrodynamic processes. Front instabilities result in areas of slightly higher permeability that concentrate the flow. This leads to faster local dissolution processes and a rapid increase in permeability compared to adjacent areas (Ortoleva et al., 1987; Hoefner and Fogler, 1988; Steefel and Lasaga, 1994; Renard et al., 1998), which develop highly conductive channels usually called as "wormholes" (or "dissolution pipes"). As soon as wormholes start growing, another important process becomes important, i.e., the competition for flow (Ewers, 1982; Daccord, 1987; Hoefner and Fogler, 1988; Buijse et al., 1997; Cohen et al., 2008; Petrus and Szymczak, 2016; Cabeza et al., 2020). Locally dominant wormholes (the longest ones) increase their capture areas, augmenting their growth potential (the concentration of fluid leads to more dissolution capacity) at the expenses of adjacent wormholes that slowly die of starvation. As the competition goes on, dominant wormholes compete with each other (Ewers, 1982; Daccord, 1987; Cohen et al., 2008), with the consequent deactivation of some previously dominant channels.

The multiple implications and applications related to wormhole preferential flow-path development justify the numerous studies carried out over

the past decades to improve our understanding of wormhole dynamics. Several experimental studies have been carried out to study wormhole formation in terms of dissolution patterns and optimum conditions for wormhole development (Daccord, 1987; Hoefner and Fogler, 1988; Daccord et al., 1993; Fredd and Fogler, 1998; Renard et al., 1998; Bazin et al., 2001; Golfier et al., 2001; Detwiler et al., 2003; Weisbrod et al., 2012; Luquot et al., 2014; Luhmann et al., 2014). These experiments were conducted to study the most common evaporitic rock, i.e., most authors focused their attention on carbonates (Hoefner and Fogler, 1988; Daccord et al., 1993; Fredd and Fogler, 1998; Bazin et al., 2001; Luquot et al., 2014; Luhmann et al., 2014), while little has been done considering halite (Renard et al., 1998; Golfier et al., 2001; Weisbrod et al., 2012) and gypsum (Daccord, 1987; Daccord et al., 1993; Li et al., 2019). Most experiments were performed in cylindrical cores, leading to single wormhole formation, while just a few considered an intermediate-scale two-dimensional tank experiment (Renard et al., 1998; Golfier et al., 2001; Detwiler et al., 2003). In these experiments, an aggressive fluid (e.g., acid) was injected at different flow rates. The volume of fluid needed for the wormhole to break through the core was measured for each injection rate. Casting methods (early studies), X-ray micro-tomography (recent studies) or camera recording methods (2D tank) have been used to visualize the resulting dissolution patterns. A common observation is that wormhole patterns depend on the flow rate applied, i.e., as the flow rate increases, compact, conical, dominant, ramified or uniform wormhole patterns develop (Hoefner and Fogler, 1988; Daccord et al., 1993; Fredd and Fogler, 1998; Golfier et al., 2001; Detwiler et al., 2003; Szymczak and Ladd, 2009).

Attempts to describe wormhole dissolution patterns have considered different dimensionless numbers that relates hydrodynamic and geochemical processes. The Peclet (Pe) number relates advection and diffusion, the Damkhöler (Da) number describes the relationship between reaction and advection, the Kinetic number (Ki) is the product of the first two and relates reaction and diffusion, and the Acid Capacity number (N_{ca}) represents the dissolution power of the flowing fluid (Golfier et al., 2002). In this context, Daccord et al. (1993)

introduced a dissolution diagram, later modified by Golfier et al. (2001, 2002), that describes the type of wormhole dissolution pattern as a function of the *Pe* and *Ki* numbers. The diagram depends also on the geochemical conditions given by the Acid Capacity number (N_{ca}). These experiments do not show the evolution of dissolution structures over time and space as well as the growth rate of preferential flow-paths and the competition between them.

Numerical simulations have also been used to study wormhole development (Steefel and Lasaga, 1994; Fredd and Fogler, 1998; Renard et al., 1998; Szymczak and Ladd, 2009, among others). Numerical simulations have studied the effect of heterogeneity and boundary conditions on dissolution patterns (Cheung and Rajaram, 2002; Kalia and Balakotaiah, 2009; Petrus and Szymczak, 2016), as well as the mechanisms controlling wormhole competition (Hoefner and Fogler, 1988; Buijse et al., 1997; Cohen et al., 2008; Szymczak and Ladd, 2009; Cabeza et al., 2020). In this context, Buijse et al. (1997) numerically analyzed the theoretical and experimental findings of Hoefner and Fogler (1988) and found that, during competition, a decreasing distance or an increasing length difference between wormholes leads the smaller wormholes to starvation. Buijse et al. (1997) estimated the flow distribution in two adjacent wormholes based on their length and proximity, finding that the interaction between wormholes becomes important when the interdistance is smaller than the length of the wormhole. Cabeza et al. (2020) formalized the concept of flow competition between wormholes. This mechanism is responsible for dissolution pattern morphology (Cabeza et al., 2020) which, as seen through numerical studies in homogeneous systems, seems to cause the wormhole density to behave as a power law with a slope of -1 (Szymczak and Ladd, 2006; Budek and Szymczak, 2012; Upadhyay et al., 2015; Cabeza et al., 2020). This value seems to agree with the work of De Waele et al. (2011), who studied nearly 200 dissolution pipes in coastal Mediterranean karst systems.

Despite the great importance of karst aquifers, laboratory experiments

aimed at directly observing wormhole competition and the temporal evolution of dissolution patterns are still lacking. In this chapter, we present a dissolution experiment in a two-dimensional synthetic aquifer composed of halite aimed at: (i) visualizing wormhole dynamics and competition; (ii) quantifying the temporal evolution of flow distribution as well as conductive structures; and (iii) examining flow and transport behavior during wormhole competition. To achieve this, a suite of pulsed tracer tests with fluorescent tracers are conducted during the dissolution experiment to delineate wormhole patterns at different times. The tracer experiments not only delineate wormhole patterns but also provide an accurate database on transport of conservative solutes in wormhole formations at an intermediate-scale. In particular, the integrated tracer breakthrough curves obtained at the tank outlet are used for exploring how transport models can effectively describe solute transport in soluble porous media with wormhole formation. We organize the chapter as it follows. In section 5.2, we present the experimental procedure and the methodology adopted for analyzing recorded data and images. Then, in section 5.3, we present and discuss the results, highlighting the outcomes in section 5.4.

5.2 Materials and Methods

5.2.1 Experimental Setup

The dissolution and tracer experiments were performed in a transparent horizontal two-dimensional tank made of plexiglass with dimensions of $26\times20\times1$ cm^3. The flow cross-section is 20×1 cm^2. The halite aquifer was placed in the central chamber of dimensions $20\times20\times1$ cm^3. Two secondary reservoirs (inlet and outlet) of dimension $3\times20\times1$ cm^3 connect the aquifer system with the inlet and outlet of the tank. These reservoirs are separated from the central chamber through a fine mesh 0.5 mm in diameter (Figure 5.1). The fluid can be injected into the inlet reservoir through a mini-pulse peristaltic pump (Gilson® Minipuls 3 Peristaltic Pump). The flow was uniformly distributed in the inlet reservoir through an 8-channel flow cell. The head pressure was

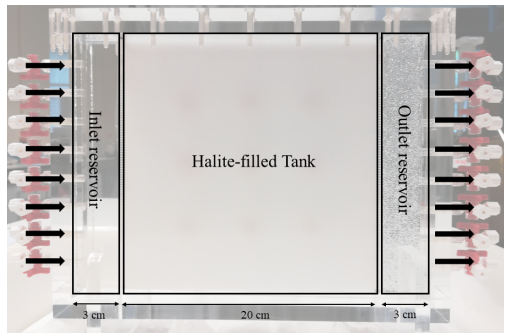

Figure 5.1: Top view of the experimental tank

kept constant at the tank outlet. The outlet reservoir was filled with glass beads of diameter $d = 2$ mm (porosity Œ = 35%). We collected the fluid at the reservoir outlet by means of another 8-channel flow cell.

The central chamber was homogeneously filled with compacted granular halite (NaCl) and brine in equilibrium with halite. Halite was obtained by sieving table salt with nominal aperture ranging between 0.52 and 0.9 mm. The brine was synthesized in the laboratory by mixing the granular halite with distilled water using a magnetic stirrer. The solution was prepared in a volumetric flask, carefully closed to avoid water evaporation. The chemical content considers only Na and Cl elements. We synthesized two different brine solutions whose main properties are summarized in table 5.1.

The first brine solution (B1) is in equilibrium with halite and its properties resemble those encountered in the Salar of Atacama (Kampf et al., 2005; Pueyo

Table 5.1: Characteristics of brine solutions

	Brine $B1$	Brine $B2$	
Dynamic Viscosity μ $^{(a)}$	0.001	0.001	$N{\cdot}s/m^2$
Fluid Density ρ	1.206	1.196	g/cm^3
Concentration C_{NaCl}	360	347	g/L
Saturation Index SI $^{(b)}$	1	0.95	-

Note. $^{(a)}$Rumble et al. (2018); $^{(b)}$calculated using the PHREEQC code (Parkhurst et al., 1999).

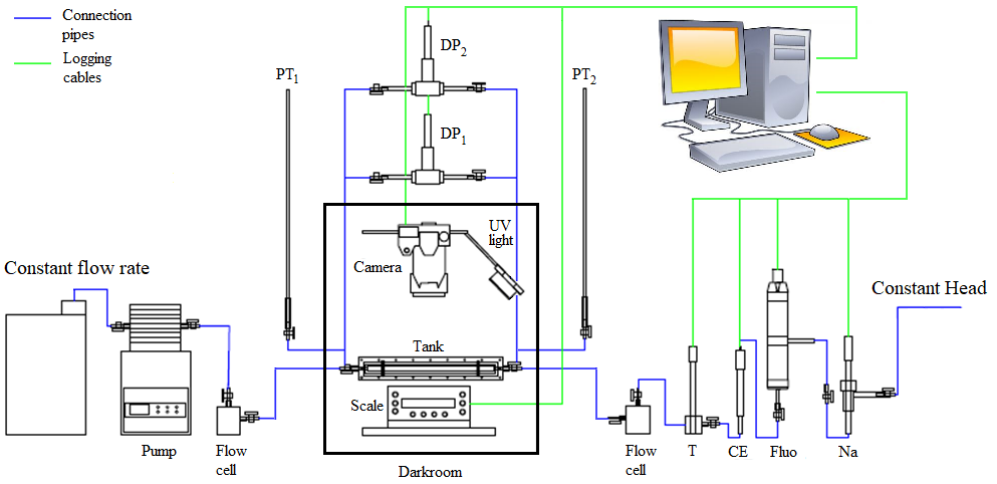

Figure 5.2: Diagram of the experimental set-up

et al., 2017). The second one (B2) is under-saturated in halite and was chosen to reproduce near equilibrium conditions, prevalent in geological systems. On the other hand, the granular halite was compacted thoroughly in the tank to avoid gaps between the plexiglass plates and the porous medium. To achieve this, the tank was flipped vertically to allow adding the halite (previously weighted) from one side. We filled the tank under saturated brine conditions to avoid air bubbles from being trapped during packing. This was done in several steps to avoid particle segregation.

A sketch diagram of the monitoring system is presented in figure 5.2. The tank was placed on top of a scale for continuously monitoring the weight of the aquifer system through the dissolution experiment with an accuracy of 0.01 g. Above the tank framework, we installed a LED Spot Strobee of wavelength λ = 395 nm for fluorophores excitation and a camera Nikon D7100 with a Tamron SP AF17-50mm F/2.8 XR Di II LD ASPHERICAL (IF) lens, jointly with a MidOpt BP525-67 filter (Light Green Band-pass) for capturing only fluorophores emission wavelength. During the experiments, we took pictures of the planar section of the entire tank (26×20 cm^2). A darkroom prevents the entrance of external light into the system. Two differential pressure transducers

(DP_1 and DP_2) and two piezometers (PT_1 and PT_2) were installed at the inlet and outlet reservoir. At the exit of the outlet flow cell, we installed several sensors placed in series: a temperature electrode (accuracy of 0.1 ° C), a conductivity cell (range: 10 µS/cm to 2000 mS/cm), a fluorimeter (FL24 Model, Albillia), and a Sodium Ion Selective Electrode (ISE).

5.2.2 Estimation of initial hydraulic properties

In order to estimate the initial hydraulic conductivity K_0, we injected saturated brine into the system at a constant flow rate of Q=7.8 ml/min. Once the system reached steady state flow conditions, we measured the differential pressure between the tank reservoirs (ΔP_0 = 0.7 cm) and we estimated K_0= 160 m/d by Darcy's law $Q = K_0 A \Delta P_0 / L$, where A= 20 cm^2 is the cross sectional area of the tank, and L= 20 cm is the length of the central chamber. We also estimated the initial porosity by gravimetric methods assuming that the halite density is constant and equal to 2.16 g/cm^3. Since we filled the tank with 568.68 g of salt (equivalent to a volume V_s =263.28 cm^3), we calculated an initial porosity of $\phi_0 = 34.18\%$. In table 5.2 we summarize the estimated properties jointly with transport and geochemical properties of the aquifer.

Table 5.2: Properties of the synthesized aquifer

Initial Hydraulic conductivity K_0	160	m/d
Initial Porosity ϕ_0	34.18	%
Intrinsic permeability k_0 $^{(a)}$	$3.13 \cdot 10^{-10}$	m^2
Specific surface σ_s $^{(b)}$	8450.7	1/m
Molecular diffusion D_m $^{(c)}$	$1.96 \cdot 10^{-10}$	m^2/s
Equilibrium constant k_{eq} $^{(d)}$	$3.72 \cdot 10^{7}$	mol/m^3
Dissolution kinetic constant k_{int} $^{(e)}$	0.68	mol/m^{2}s
Grain diameter d_{50}	0.71	mm

Note. $^{(a)}$Estimated from $k_0 = K_0 \mu / g \rho_{B1}$; $^{(b)}$ Estimated assuming spherical grains as $\sigma_s = 6/d_{50}$; $^{(c)}$ Estimated from $D_m = D \cdot \phi_0^2$, being $D = 1.68 \cdot 10^{-9}$ m^2/s the water molecular diffusion (Lasaga, 1998); $^{(d)}$ PHREEQC database (Parkhurst et al., 1999); $^{(e)}$Alkattan et al. (1997).

5.2.3 Dissolution Experiment

The dissolution experiment involved injecting an under-saturated brine (B2) of known concentration through the halite-filled tank, initially saturated with saturated brine (B1), during 135 minutes. According to Golfier et al. (2002), the dissolution pattern is controlled by the Peclet and the Kinetic number,

$$Pe = \frac{\ell q}{D_m \phi_0}, \tag{5.1}$$

$$Ki = \frac{\ell^2 k_m}{D_m}, \tag{5.2}$$

where ℓ is the characteristic length of the soil grains, estimated as $\ell = \sqrt{K_0}$, D_m is the apparent molecular diffusion, and k_m is the mass transfer coefficient, determined as $k_m = k_{int}\sigma_s / \sqrt{k_{eq}}$, where k_{int} is the dissolution kinetic constant, σ_s the specific surface, and k_{eq} the equilibrium constant (Table 5.2). The B2-Brine was injected through the inlet reservoir at a constant flow rate, Q = 7.8 ml/min. With this flow rate, we estimated that $Pe = 17.58$ and $Ki = 1.50$. According to the $Ki - Pe$ dissolution diagram proposed by Golfier et al. (2002), these experimental conditions (Table 5.3) should allow reproducing a dominant wormhole regime.

Table 5.3: Experimental conditions

Main chamber length L	20	cm
Main chamber width ω	20	cm
Cross sectional area A	20	cm^2
Total flow rate Q	7.8	ml/min
Darcy's flux $q = Q/A$	0.39	cm/min
Initial differential pressure ΔP_0	0.7	cm
Peclet number Pe	17.58	-
Kinetic number Ki	1.50	-

The inlet reservoir allows keeping the head constant throughout the dissolution experiment, allowing the flow to redistribute itself according to the

heterogeneity of the aquifer. At the outlet head is kept constant. The total volume of under-saturated brine injected in the system is V_{B2} = 1053 ml. During the experiment, the following parameters were continuously measured: differential pressure (every second), tank weight (every 5 seconds), temperature and electrical conductivity (every 5 seconds), fluorescence (every 10 seconds), and Na concentration of the downstream brine (every second). The evolution of the dissolution pattern was visually recorded by taking pictures every 32 seconds during the whole dissolution period.

To estimate the variation of hydraulic conductivity we used differential pressures measured with transducer DP_1, while we discarded data recorded with DP_2, as they are corrupted. Raw data (mV), filtered from any fluctuation not related to the experiment through moving average, were transformed into differential pressure ΔP (cm) applying the calibrated equation that relates the two magnitudes. We applied Darcy's law to estimate hydraulic conductivity changes due to the development of wormholes, knowing the injection rate Q = 7.8 ml/min, A = 20 cm^2 and L = 20 cm.

We also estimated porosity changes analyzing the variation of the total mass ΔM_{tot}. During the dissolution experiment, the tank weight may change due to changes in the porosity, differences between brine and halite density ($\Delta\rho$) as well changes in brine density ($\Delta\rho_B$). Neglecting the latter, we can write mass variation as $\Delta M_{tot} = V_{Tank}\Delta\phi\Delta\rho$ (Appendix A). We know V_{Tank} = 400 cm^3 and $\Delta\rho$ = -0.95 g/cm^3; at the same time we measured M_{tot} every second. Thus, we can estimate porosity throughout the whole experiment, knowing ϕ_0 (Table 5.2). The value of the final porosity was compared to the one calculated considering the dissolution capacity of the injected volume of under-saturated brine.

5.2.4 Tracer Test Experiments

We carried out six tracer tests. The first pulse test (T_0) was performed before starting the dissolution experiment. The aim is that of understanding initial

transport behavior of the system and to spatially visualize initial aquifer heterogeneity (if any). We injected saturated brine with a fluorescein concentration C_{T_0} of 1 mg/L. The pulse lasted four minutes after which saturated brine with no tracer was injected for 233 minutes, ensuring an almost full recovery. Once started the dissolution test, four subsequent tracer tests were carried out at times $t_{T1} = 20$, $t_{T2} = 54$, $t_{T3} = 88$ and $t_{T4} = 122$ minutes. Each pulse lasted four minutes in which we injected under-saturated brine with sodium fluorescein (C_T = 20 mg/L). At time t_{d_f} = 135 min. the dissolution test ended but the tracer test went on: without switching off the pump, we started injecting saturated brine to fully recover the last pulse of fluorescein while the system was reaching geochemical stability. Once almost all the fluorescein (T_4) was recovered, we performed an additional tracer test T_5 in stable conditions, starting at t_{T_5} =352. Again, the pulse lasted four minutes and we recovered for 354 minutes, up to t_f = 702. Differential pressure and tank weight as well as temperature and electrical conductivity, fluorescence and Na concentration of the downstream brine were continuously measured during the whole tracer test periods.

5.2.5 Mathematical Models

Wormhole Competition Model

Flow competition has been suggested to control wormhole growth and dissolution patterns (Buijse et al., 1997; Cohen et al., 2008; Cabeza et al., 2020, among others). During the development of a wormhole, the flow rate caught by locally dominant wormholes increases at the expense of shorter wormholes that gradually die of starvation. In this context, Cabeza et al. (2020) have recently developed a competition model for wormhole growth in a two-dimensional aquifer system subject to a natural flux q_N. Assuming that a wormhole grows as a straight line oriented along the flow direction and that the permeability of the wormhole is infinite relative to the matrix (defined as the non-dissolved porous media), these authors found that the flow rate Q_i captured by a given wormhole i can be written as

$$Q_i = \omega_i q_N, \tag{5.3}$$

where q_N is the natural flow rate per unit width in the matrix system. In an analogy with well catchment theory, the authors defined ω_i as the wormhole capture area (the matrix length transverse to the flow direction that carries the same total flow rate as the wormhole). The concept is illustrated in Figure 5.3. We will compare experimental results with the estimates obtained by applying the analytical solution for the wormhole competition model (Cabeza et al., 2020).

For a single wormhole without neighbors, Cabeza et al. (2020) found that the capture area is $\omega_{si} = 2L_i$, where L_i is the wormhole length. For multiple wormholes, the capture area of each one decreases as several flow-paths are competing for the flow. The flow reduction depends on the length of all developing wormholes and their relative interdistance d_{ij}. In this case, Cabeza et al. (2020) found that ω_j should satisfy the following system of equations

$$\sum_{j=1}^{n} \left[\delta_{ij} + (1 - \delta_{ij}) \frac{\omega_{rij}}{\omega_{sj} - \omega_{rji}} \right] \omega_j = \omega_{si}, \qquad for i = 1, ..., n, \tag{5.4}$$

where n is the number of wormholes, and ω_{rij} is the reduction of the ith wormhole capture area caused by the flow rate in the jth wormhole. The reduction is estimated by

$$\omega_{rij} = \gamma_1 \gamma_2 L_j, \tag{5.5}$$

$$\omega_{rji} = \omega_{sj} - \gamma_1 L_j, \tag{5.6}$$

where

$$\gamma_1 = \min\left\{2, \frac{\arctan(U)}{1 - 0.2\arctan(U)}\right\}, \tag{5.7}$$

$$U = 0.0214\frac{L_j}{d_{ij}} + \frac{2d_{ij}}{L_i - \gamma_2 L_j}, \tag{5.8}$$

and

$$\gamma_2 = \min\left\{0.42\ln\left(1 + \frac{L_j}{d_{ij}}\right), \frac{L_j}{L_j + 2d_{ij}}\right\}. \tag{5.9}$$

The Multi-Advection Dispersion Model

The integrated tracer breakthrough curves obtained at the tank outlet before and after the dissolution experiment (T_0 and T_5) were used to explore how can we describe solute transport through geological formations characterized by wormholes with simple models. For this, we consider that the development of wormholes in a porous medium leads to a multi-advection dispersion model, which represents the local variations in flow rates through a series of flow pathways. Solute transport in each flow pathway is described by the following advection-dispersion equation,

$$\frac{\partial C_i}{\partial t} = -v_i\frac{\partial C_i}{\partial x} + D_i\frac{\partial^2 C_i}{\partial x^2}, \qquad fori = 1, ..., N_p, \tag{5.10}$$

where C_i is the local scale solute concentration along the ith pathway, v_i is the fluid velocity along the ith pathway, and $D_i = \alpha_i v_i$ is the dispersion coefficient (we neglect diffusion) where α_i is the dispersivity. For simplicity, we disregard the potential interaction between pathways (mass exchange). Parameters are assumed constant along each pathway. The solute concentration for the entire field is given by the weighted average of the local pathway concentrations. In terms of flux-concentrations, mass conservation (at the tank outlet) requires that

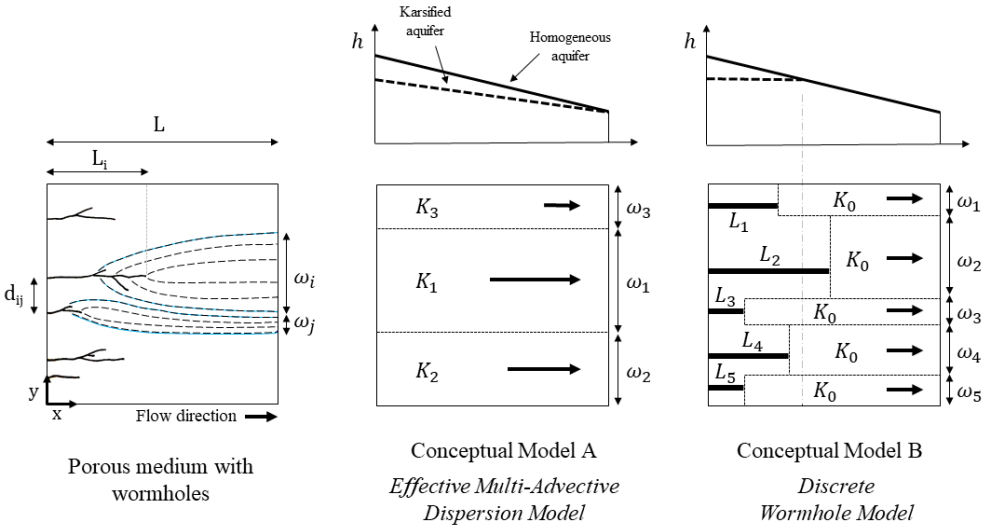

Figure 5.3: On the left, schematic representation of a porous medium characterized by wormholes. We highlight two competing wormholes (i and j) having a interdistance (d_{ij}) and length L_i (wormhole i). The main streamlines (dash-grey) are drawn, highlighting the capture areas ω_i, ω_j bounded by blue streamlines. In the middle, scheme of a transport modelling approach (conceptual model A) that consider a set of equivalent pathways characterized by effective parameters to simulate transport in the karsified system. On the right, the discrete model (conceptual model B) maintains the information on the geometry of the dissolution structure. In this case, the head is constant through the wormhole and transport is estimated only through the undissolved matrix ($L - L_i$), characterized by known effective transport parameters.

$$C^f(x,t) = \sum_{i=1}^{N_p} \beta_i C_j^f(x,t), \qquad \beta_i = \frac{Q_i}{Q} \tag{5.11}$$

where N_p is the number of transport pathways, β_i is the flow contribution of each pathway to the total flow Q passing through the porous media. Flow conservation constraints require that $\sum_{i=1}^{N_p} \beta_i = 1$. The analytical solution of flux concentrations satisfying (5.10) for a semi-infinite one-dimensional system subject to a Heaviside injection is (Parker and van Genuchten, 1984),

$$B_i(x,t) = \frac{1}{2}\text{erfc}\left[\frac{x - v_i t}{2(D_i t)^{1/2}}\right] + \frac{1}{2}\exp\left(\frac{v_i x}{D_i}\right)\text{erfc}\left[\frac{x + v_i t}{2(D_i t)^{1/2}}\right]. \tag{5.12}$$

However, the concentrations at the inlet boundary of the test aquifer vary as a function of time due to dilution in the left chamber. To take this into account, we applied the principle of superposition, which determines that the output concentration is the convolution of the inlet boundary concentration with the Green's function. This can be written as

$$C_i^f(x,t) = C_0(\tau_0)B_i(x, t-\tau_0) + \sum_{j=1}^{\tau_j<t} \Delta C_0(\tau_j)B_i(x, t-\tau_j)d\tau, \tag{5.13}$$

where τ_0 is the injection time, $C_0(\tau_j)$ is the inlet boundary concentration of the aquifer at time τ_j, and

$$\Delta C_0(\tau_j) = C_0(\tau_j) - C_0(\tau_{j-1}). \tag{5.14}$$

The estimate of the inlet boundary concentrations $C_0(\tau)$ is obtained through image processing, later described in section 5.2.7.

5.2.6 Modeling Approach

We considered two transport modeling approaches (Figure 5.3). The first approach considers an effective multi-advection dispersion model characterized by a relatively simple set of flow pathways. In this case, we calibrated β_i, v_i, D_i against the experimental tracer breakthrough curves by minimizing the sum of squared errors between the outlet concentration measurements and $C^f(x = L, t)$, where L is the aquifer length. The interpretation of the T_0 tracer experiment yields the effective transport parameters of the matrix, whereas

the T_5 tracer experiment represents transport in porous media with wormholes. For each tracer test, we considered different numbers of pathways N_p. We sought the simplest conceptual model, i.e., the minimum number of equivalent pathways which can explain the tracer breakthrough curves. When $N_p > 1$, the last flow contribution was fixed to

$$\beta_{N_p} = 1 - \sum_{i=1}^{N_p - 1} \beta_i. \tag{5.15}$$

The other approach considers a discrete wormhole modeling approach that explicitly represent the geometrical properties of wormholes. Here, we assumed that the number of wormholes n, the length of the wormholes L_i, and their capture area ω_i is known, and we construct a multi-advection dispersion model based on this. In this case, the parameters are not calibrated but estimated from the following considerations: (1) the number of pathways is given by the actual number of wormholes, $N_p \approx n$; (2) the flow contribution of each flow path β_i is estimated as $\omega_i / \sum \omega_i$; (3) the permeability of the wormhole is assumed infinite with respect to the matrix so that the concentration is constant along the wormhole and transport in the matrix only takes place along the distance $L - L_i$, i.e., from the tip of the wormhole channel to the end of the aquifer; (4) the velocity v_0 and dispersivity α_0 of the matrix system (the porous media before dissolution) is known. Based on this, the flux concentrations obtained at the tank outlet can be written as

$$C^f(x = L, t) = \sum_{i=1}^{n} \frac{\omega_i}{\omega} C_m^f(L - L_i, t) \tag{5.16}$$

where $C_m^f(L - L_i, t)$ is the flux concentration of a solute that moves through the matrix system from $x = L_i$ to $x = L$ with a velocity and dispersivity fixed to v_0 and α_0, respectively.

5.2.7 Image processing

The camera was used to continuously record 24-bit RGB color images during the tracer test experiments. Tracer images were used to estimate the temporal evolution of wormhole lengths L_i and densities n along the flow direction, the wormhole capture areas ω_i, and the changes in boundary concentrations C_0 at the inlet reservoir.

For each tracer test, the image processing procedure involved the following steps: (1) crop all images to the region that encloses the central aquifer chamber. This yields images with a spatial resolution of 1900×1900 pixels, the size of which are 0.105 mm; (2) remove background noise from all images by subtracting the RGB color image obtained right before the fluorescein tracer enters into the aquifer; (3) convert the RGB images to grayscale images I_{gs}; (4) rescale intensities between 0 and 255 to enhance brightness and contrast; (5) convert the I_{gs} images to binary images I_{bi} using the spatial average of I_{gs} over the area unaffected by the tracer plume as a threshold value I^*_{gs}. When $I_{gs} \leq I^*_{gs}$ then $I_{bi} = 1$, and zero otherwise. The objective here is to delimit the tracer plume area while minimizing background noise. (6) For each image pixel, plot the tracer test duration against binary intensities and estimate the plume front arrival travel time T_f as the smallest time for which $I_{bi} = 1$.

The color map of T_f displays the temporal evolution of the fluorescein front during the tracer experiments that permits to visually identify the wormholes. From this, we calculated wormhole lengths L_i by manually setting the tip position, assuming a straight development from the inlet. During wormhole identification, the movie of color images was used as visual support. Since each wormhole generates a distinct source of tracer entering into the matrix, one can also delimit the capture area of each wormhole. We then measured ω_i by taking the plume width at the aquifer exit (x$\simeq$L).

Since the method is subject to uncertainty given by visual identification, we applied a different procedure for calculating the length of main wormholes (Figure 5.4) and we compared the values of both methods to ensure the

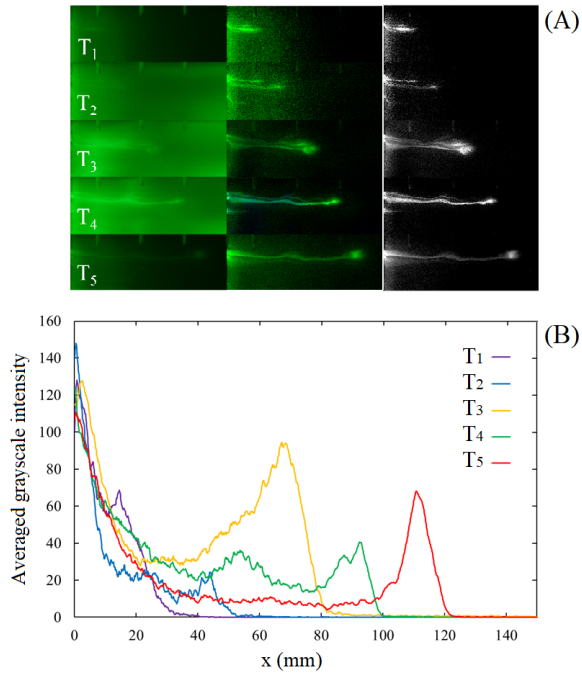

Figure 5.4: Image analysis to estimate wormhole length. The image sequence (A) shows image analysis of the selected area for one wormhole, at different stages (tracer tests T_1 up to T_5. The graph (B) shows the averaged pixel intensity calculated for each T_i.

reliability of the results. For each wormhole and tracer test, the procedure consists of: (1) crop the I_{gs} images to the area that encloses the wormhole; (2) determine the vertical average of I_{gs} along the y direction. For each wormhole, we obtained five graphs, each one corresponding to a different stage of wormhole growth (Fig. 5.4). We assumed that the peak of intensity farthest from the inlet (x=0) corresponds to the wormhole tip. With this assumption we calculated wormhole length assuming a straight development. Comparing the results we calculated a root mean square error of 0.29 cm.

We also estimated the temporal variations of concentrations C_0 at the inlet reservoir during the tracer experiments through image processing. To achieve this, we applied the same image procedure as before to obtain the grayscale

image sequence I_{gs} at the inlet reservoir. The selected background image noise was defined from the time before fluorescein enters into the inlet reservoir. We then calculated the vertical average of I_{gs} at $x = -5$ mm and we rescaled the values between 0 and 255 to cover the entire grayscale range. According to the literature (Zhang et al., 2009; Anna et al., 2014; Haas et al., 2020), we considered that concentrations are proportional to pixel intensities such that $C_0 = a\overline{I}_{gs}$, where $\overline{I}_{gs}$ is the vertically averaged intensity, and C_0 the fluorescein concentrations at the inlet reservoir. The constant of proportionality a was determined by mass balance as

$$a = \frac{\int_0^\infty C_f(t)dt}{\int_0^\infty \overline{I}_{gs}(t)dt}. \tag{5.17}$$

where C_f is the flux concentration measured at the tank outlet.

5.3 Results and discussion

5.3.1 Wormholes Growth Evolution

The dissolution experiment reproduces the dissolution pattern typical of a dominant wormhole regime. Figure 5.5 shows, for each tracer test, two snapshots of the fluorescein tracer images obtained during the dissolution experiment at two different elapsed times from tracer injection. The T_0 tracer plume shows that, before dissolution, the flow generates almost parallel straight streamlines oriented along the x direction. Even though we notice some stratification (mostly due to aquifer packing), the tracer plume front is mostly uniform and the fluid is initially flowing through the porous media with more

Figure 5.5: (Following page). Evolution of the dissolution pattern over time. For each tracer test (T_0 to T_5), two time steps are shown to highlight wormhole development and differences in flow velocity between dominant and secondary wormholes. In each image of the sequence we highlight the time elapsed since the injection of the tracer.

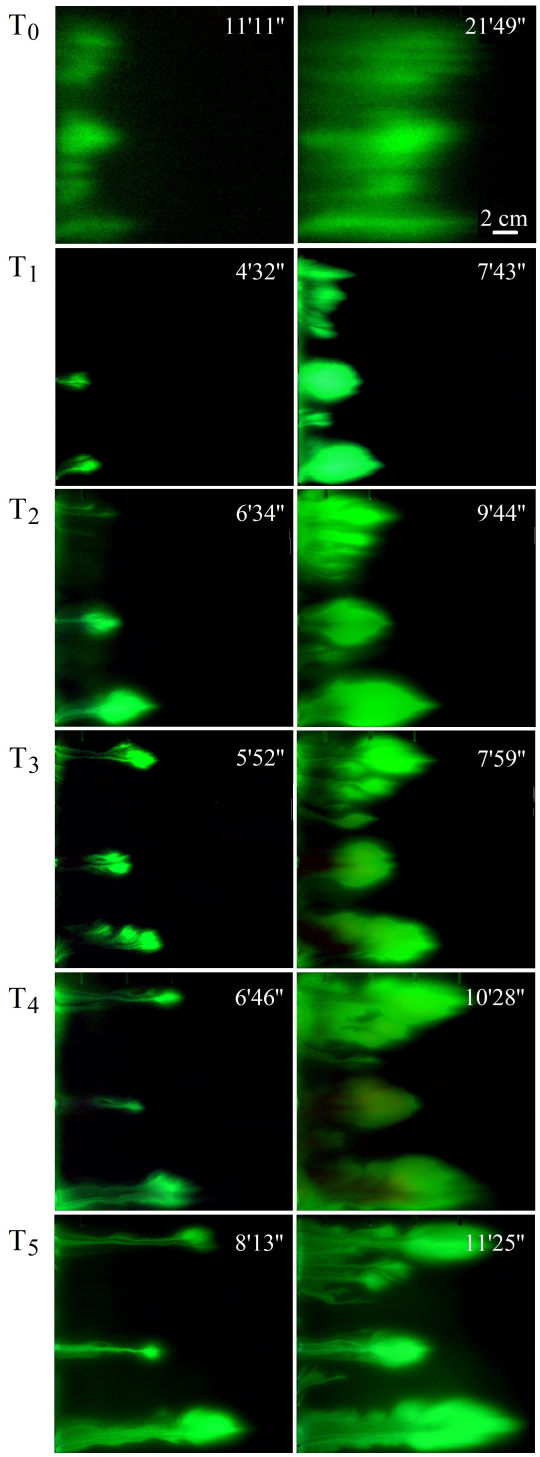
T0
11'11"
21'49"
2 cm
T1
4'32"
7'43"
T2
6'34"
9'44"
T3
5'52"
7'59"
T4
6'46"
10'28"
T5
8'13"
11'25"

or less equal velocity everywhere. Results demonstrate that the fluorescein tracer images taken during and after the dissolution experiment (T_1, T_2, T_3, T_4, T_5) allow visualizing wormhole dissolution patterns because the tracer preferentially flows through the wormholes.

We observe that solute transport is concentrated through few flow-paths moving with greater velocities, which suggests locally higher permeability and growth potential. We refer to these highly conductive flow channels as dominant wormholes. However, we see that solute is carried also with a certain delay through minor secondary wormholes. The secondary wormholes closest to the dominant ones seem to be more developed than their neighbors (Figure 5.6). At the end of the dissolution process it seems that all wormholes are still carrying flow (Figure 5.6).

We note that the tracer images show that the initial variability of the local velocity field (heterogeneity) plays an important role in the location of the flow channels that developed during the dissolution experiment. Dominant

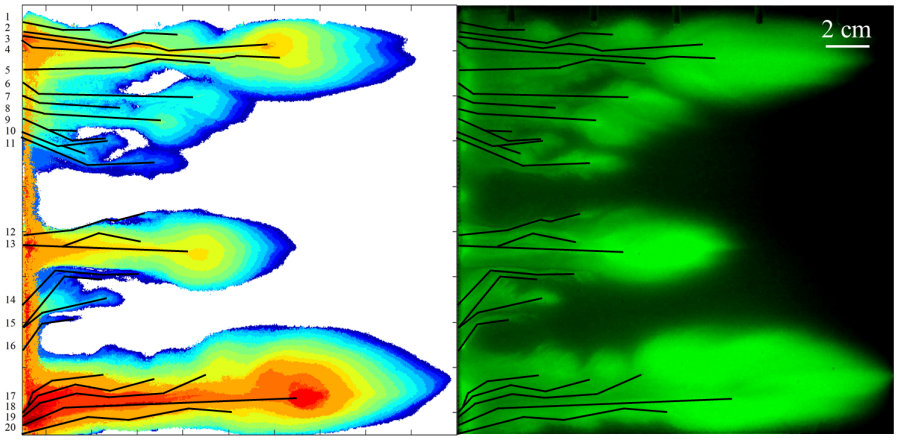

Figure 5.6: Dissolution structures at the end of the dissolution experiment (on the left), highlighted through image processing of the tracer test T_5 (on the right). Time-steps of fluorescein transport are highlighted by different colors. All identified wormholes are drawn as black lines. Numbers correspond to wormholes IDs.

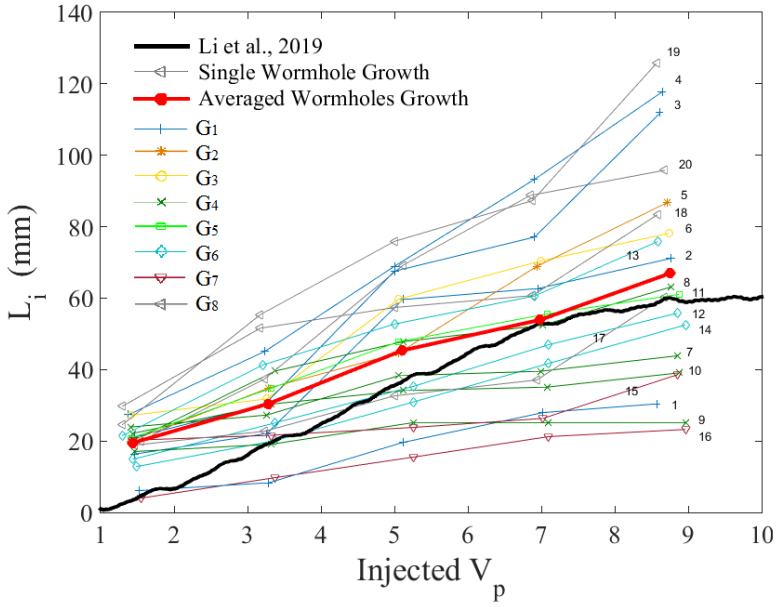

Figure 5.7: Wormhole growth rate: length evolution is plotted for each wormhole developed in the aquifer. Wormholes are grouped by color according to the capture area they belong to. Moreover, we compare the solution for growth evolution of an equivalent wormhole calculated applying equation (5.18) (Li et al., 2019) (black line) and the the average of experimental wormhole growths estimated from image analysis (red line).

wormholes seem to develop in areas with initial higher velocities. This can be seen as the instability front necessary for triggering wormhole development.

In order to better understand the competition between wormholes, we analyzed the temporal evolution of wormhole lengths. Figure 5.7 shows the wormhole length as a function of the injected pore volume of unsaturated brine. Results show that all wormholes grow linearly over time but at different rates. In general, the longer the wormhole length, the faster the growth rate. Results present the first quantitative evidence of the amplifying factor that characterizes the self-organization mechanism in wormhole growth, i.e., dissolution produces highly conductive channels that concentrate the flow

and further enhance dissolution. Most wormholes exhibit a linear trend until the end of the dissolution experiment, except some short wormholes that undergo a decrease in their growth rate at late times, showing symptoms of flow starvation: as the growth potential of dominant wormholes increases (higher flow rate), secondary wormholes slowly die.

5.3.2 Changes in Hydraulic Properties

We now discuss the effect that the evolving wormhole dissolution pattern has on the hydraulic properties of the porous medium. As shown in Figure 5.8, both the experimental effective hydraulic conductivity K^e and porosity vary linearly over time, as wormholes advance throughout the domain, up to the end of the dissolution experiment when they stabilize. In this context, Li et al. (2019) proposed an analytical solution that relates wormhole lengths with differential pressures in a specimen characterized by preferential flowpaths whose permeability is assumed infinite. They consider that the differential pressure between the specimen inlet and the outlet depends only on the undissolved matrix that separates the wormhole tip from the outlet (zero head loss in the wormhole itself). With this assumption, they directly relate wormhole section length L_ω and differential pressure ΔP as:

$$\frac{L_\omega}{L} = 1 - \frac{\Delta P}{\Delta P_0}, \tag{5.18}$$

where L is the specimen length and ΔP_0 the initial differential pressure. In other words, knowing the evolution of wormhole length it could be possible to estimate the evolution of K^e.

$$K^e = K_0 \left(\frac{L}{L - L_\omega} \right) \approx K_0 \left(\frac{L}{L - \overline{L}_i} \right). \tag{5.19}$$

Thus, we compare experimental results with the analytical solution for wormhole growth proposed by Li et al. (2019), as we independently measure the evolution of wormhole lengths and that of ΔP. Knowing L, ΔP_0 and ΔP

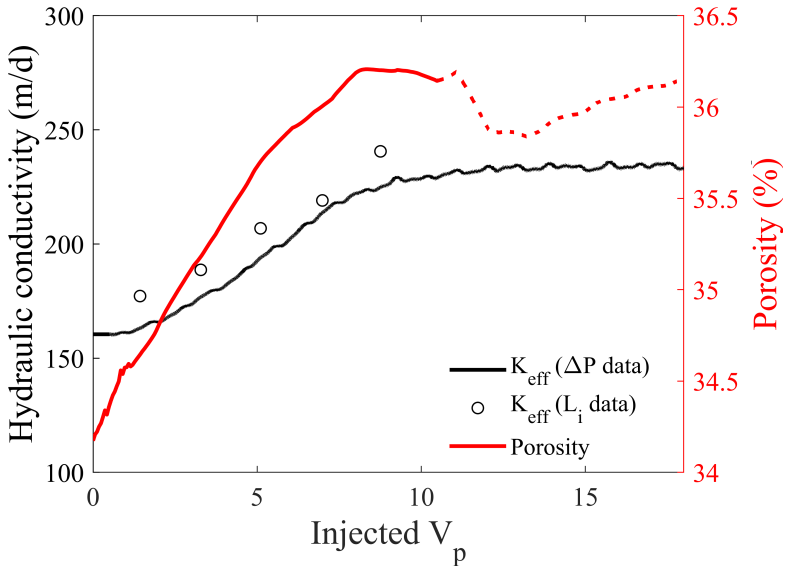

Figure 5.8: Temporal evolution of aquifer hydraulic properties estimated from experimental data. In particular, we compare the effective hydraulic conductivity K^e estimated from differential pressure data (black line) and the one obtained applying equation (5.19), i.e. knowing the evolution of the averaged wormholes lengths $\overline{L_i}$ (black circles).

(continuously measured over time) we estimate wormhole growth from equation (5.18) (Figure 5.7). Since we are in a context of multiple paths, we compare the result with the average of wormhole lengths (equivalent wormhole length) calculated at each measurement time. We find that wormhole growth calculated from equation (5.18) approximate the averaged wormhole growth evaluated from image analysis, even if early times do not fit quite well. Still, late times and the final estimation of the equivalent wormhole length reproduce quite well the experimental results. This suggests that one can estimate the effective hydraulic conductivity of a karstified aquifer system from the geometry of the wormhole dissolution pattern (Figure 5.8).

5.3.3 Wormhole Competition

A direct consequence of different growth rates in wormhole competition is the evolution of the distribution of wormholes over time and space. In figure 5.9A, we represent the evolution of wormholes density over space during the dissolution experiment. Density is defined here as the ratio between the number of wormholes n at a given distance x from the inlet and the initial number of wormholes n_0. At early times (T_1), there is an abrupt decrease of the number of wormholes over space, meaning that wormholes are almost

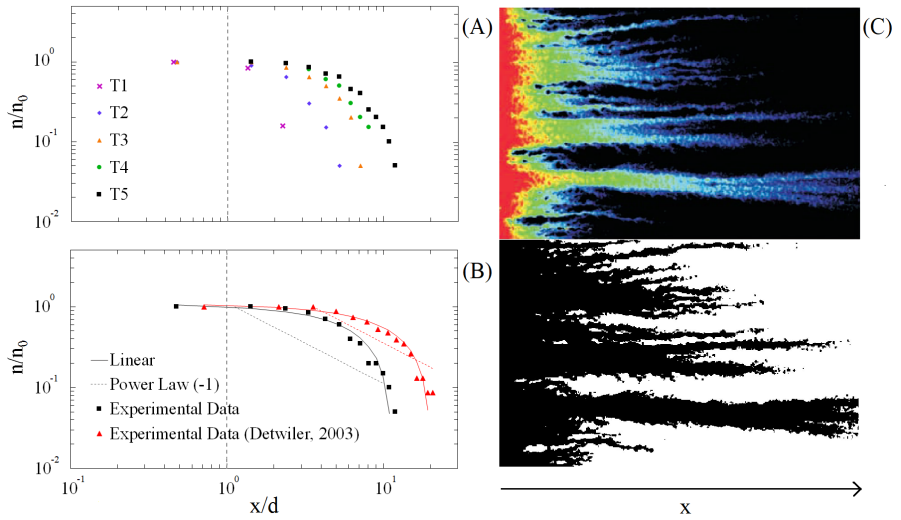

Figure 5.9: Analysis of the dissolution pattern: wormholes density. Figure 5.9A shows density evolution over space during the experiment. Time is expressed in terms of tracer tests sequence (from T_1 to T_5). The normalized distance is the ratio between the actual distance from the inlet (x) and $d = \omega/(n_0 - 1)$, i.e. the interdistance between wormholes if they were equally spaced. In figure 5.9B we plot the comparison between densities calculated from experimental data (Detwiler et al. (2003) and present work) and the power law trend (slope of -1) estimated from numerical models. Figure 5.9C shows image analysis of the resultin pattern obtained by Detwiler et al. (2003) (modified from Detwiler et al. (2003)).

equally developed in the system. The reduction starts around x/d=1, being $d = \omega/(n_0 - 1)$ the relative distance between wormholes if they were equally distributed along the inlet section. In other words, the competition starts when the length of the flow-paths is similar to their interdistance, considering wormholes equally spaced. Results are consistent with what already described in literature by several authors (Hoefner and Fogler, 1988; Buijse et al., 1997; Cabeza et al., 2020), i.e. the interaction between two adjacent wormholes become important when their length is higher than their interdistance. With the evolution of the dissolution pattern (from T_2 up to T_5), the density trend evolves: the rate of density reduction over space decreases and converges to a linear reduction in T_5. This trend evolution over time is justified by what has been previously observed: all wormholes grow over time during the dissolution experiment. The direct consequence is that the number of wormholes that exceed a selected distance x from the inlet increases over time.

The linear trend to which density converges differs from what has been numerically estimated by previous works (Szymczak and Ladd, 2006; Budek and Szymczak, 2012; Upadhyay et al., 2015; Cabeza et al., 2020). The authors estimate density to decay following a power law of slope close to -1. Still, we compare density values with those estimated from the experiment carried out by Detwiler et al. (2003). We select the image of the resulting dissolution pattern for $Pe = 54$ and we calculate the density evolution over space (Figure 5.9C). In figure 5.9B we compare experimental results from both Detwiler et al. (2003) and the present work, as well the linear and power law trends. The experimental dissolution pattern (Detwiler et al., 2003) is characterized by a linear trend of wormhole distribution, in agreement with results of the present work. The difference lies in the rate of density decrease, which is lower in the experiment carried out by Detwiler et al. (2003).

5.3.4 Wormhole capture area

Lastly, we analyze the flow rate distribution along the dissolution pattern, as it is directly related to the growth potential of each wormhole, i.e., related to the competition among them. From image analysis we estimate capture areas ω_i, proportional to the flow rate carried by each flow-path. Results are consistent with previous observations and estimates. Looking at the image sequence we observe that almost all wormholes are still carrying flow during tracer test T_5 (Figure 5.10). It justifies both wormhole growth evolution (Figure 5.7) and density evolution (Figure 5.9). Still, at the outlet of the aquifer we identify eight capture areas.

Table 5.4: For each identified wormhole, we present its final length $L_i(T_5)$ and its normalized capture area calculated applying the analytical solution proposed by Cabeza et al. (2020).

Wormhole ID	L_i (cm)	$\omega_i / \sum \omega_i$
1	3.01	0
2	7.11	0.034
3	11.19	0.16
4	11.78	0.18
5	8.67	0.02
6	7.82	0.02
7	4.38	0
8	6.32	0.015
9	2.51	0
10	3.91	0
11	6.12	0.03
12	5.58	0.01
13	7.59	0.10
14	5.25	0.06
15	3.85	0.004
16	2.32	0
17	6.04	0.002
18	8.35	0.02
19	12.58	0.28
20	9.58	0.11

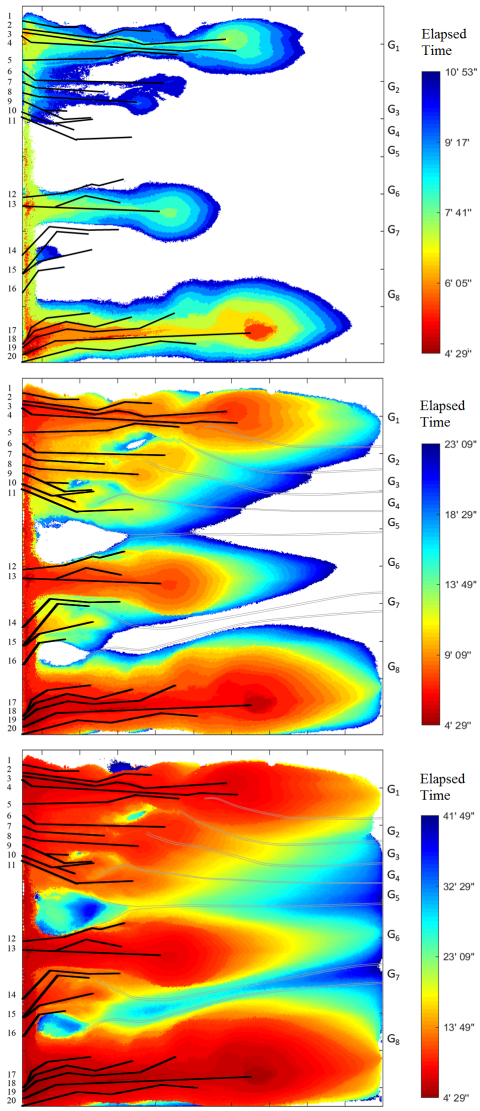

Figure 5.10: Estimating capture areas through image analysis. Three time-steps of solute transport through the undissolved matrix are shown, highlighting i) defined capture areas (grey line, G_i), ii) developed wormholes (black line) and iii) time elapsed from the injection of tracer T_5 (color sequence).

Table 5.5: The table shows, for each group of channels, the normalized capture area $\omega_i / \sum \omega_i$ calculated with the image analysis and from Cabeza et al. (2020), jointly with the equivalent wormhole length L_i, i.e. the average of the lengths of wormholes belonging to the same group.

Wormhole group	L_i (cm)	$\omega_i / \sum \omega_i$ (Image analysis)	$\omega_i / \sum \omega_i$ (Cabeza et al., 2020)
G_1	8.22	0.20	0.37
G_2	8.67	0.06	0.02
G_3	7.82	0.06	0.017
G_4	4.40	0.06	0.015
G_5	6.11	0.05	0.034
G_6	6.14	0.18	0.129
G_7	3.09	0.04	0.004
G_8	9.14	0.35	0.411

Most of them are the result of solute transport through multiple flowpaths. Thus, we define eight groups of wormholes (G_i) and calculate, for each one, an averaged length L_i of the "equivalent" wormhole (Table 5.5). As expected, there are three capture areas much wider than the the others (G_1.G_6, and G_8), which are the one traversed by flow rate carried by dominant wormholes (among others), i.e. the wormholes with the highest growth potential.

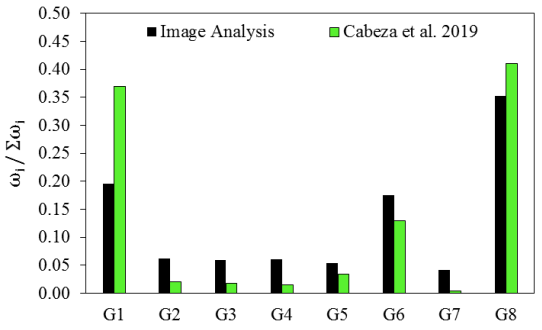

Figure 5.11: Comparison between capture areas ω_i estimated through image analysis and those estimated applying the analytical solution proposed by Cabeza et al. (2020).

We compare results of image analysis with those obtained estimating ω_i applying the analytical solution proposed by Cabeza et al. (2020) and recalled in section 5.2.5. For each wormhole, they consider the reduction of its capture area due to the presence of all other flow-paths.

The reduction depends on their length and distance from the considered wormhole. We estimate the capture area of each flow-path identified in the system (Table 5.4). We add the capture areas belonging to the same group G_i and we compare the results (Figure 5.11, table 5.5). The overall distribution of the flow between main and secondary channels is similar. However, applying the solution proposed by Cabeza et al. (2020) we underestimate the activity of smaller channels.

5.3.5 Tracer Test Breakthrough Curves

The tracer breakthrough curves obtained during the T_0 and T_5 experiments are shown in Figure 5.12 as a function of the injected pore volume. Given that porosity changes were relatively small during the experiment, pore volumes were estimated as $V_p = Q(t - t_T)/V\phi_0$, where V is the aquifer total volume, Q the total injected fluid rate, t_T is the time of tracer injection, and ϕ_0 is the initial porosity of the aquifer (before dissolution). The concentrations are normalized by the injected concentration C_0. The estimated concentrations at the inlet reservoir are denoted as $BC(T_i)$. The T_0 tracer breakthrough curve obtained before the start of dissolution exhibits a Fickian-like behavior even though a relatively long tail is manifested as a result of slow flushing of the tracer out of the inlet reservoir.

The reservoir flushing effect justifies the deviation of the mean arrival of the breakthrough curve from V_p=1. We note a small inflection point at the tail, which may suggest the presence of a secondary pathway, consistent with the slight stratification detected from images. This Fickian-like behavior is destroyed by dissolution. The presence of wormholes in the T_5 experiment produces a faster tracer arrival with two pronounced peaks and a longer tail.

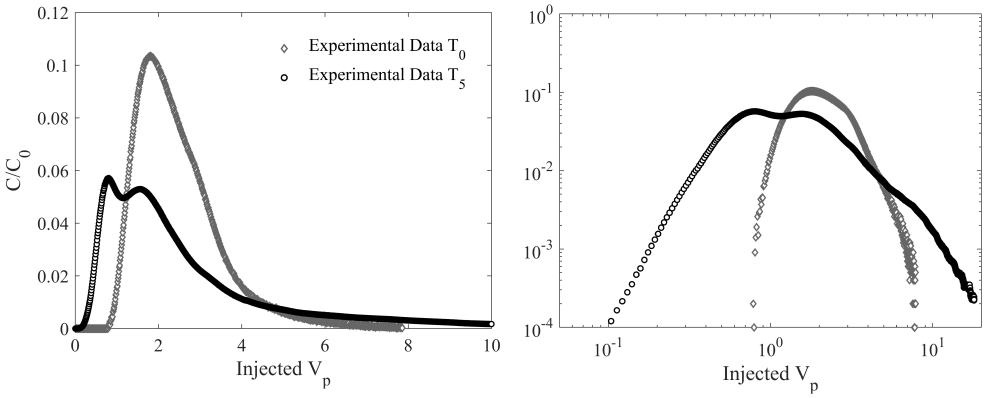

Figure 5.12: Experimental tracer breakthrough curves obtained during the initial (T_0) and final (T_5) tracer tests, carried out before and after wormholes development. Normalized concentrations are plotted as a function of the injected pore volumes V_p in linear (left) and log-log (right) scale. In the former, the final part of the T_5 tail has been omitted to better visualizing main differences in arrival times and peaks.

The tail behaves as a power law with slopes (before and after an inflection point) of about -2 and -4 (Figure 5.14, right).

Effective Solute Transport Modeling

The interpretation of the breakthrough curves with effective models provides a quantitative assessment of the transport behavior. The best fit between the tracer breakthrough curves and the effective multi-advection dispersion model is shown in Figures 5.13 and 5.14 for the T_0 and the T_5 experiment, respectively. The breakthrough curves are presented in actual values and in double-log scale to better appreciate the details (early arrival, peaks, and tail). We seek for the simplest conceptual model characterized by the minimum number of equivalent pathways. Based on the number of peaks detected, we considered that the system can be effectively represented by 1 or 2 pathways in the T_0 experiment and 2 or 3 pathways in the T_5 experiment. The calibrated

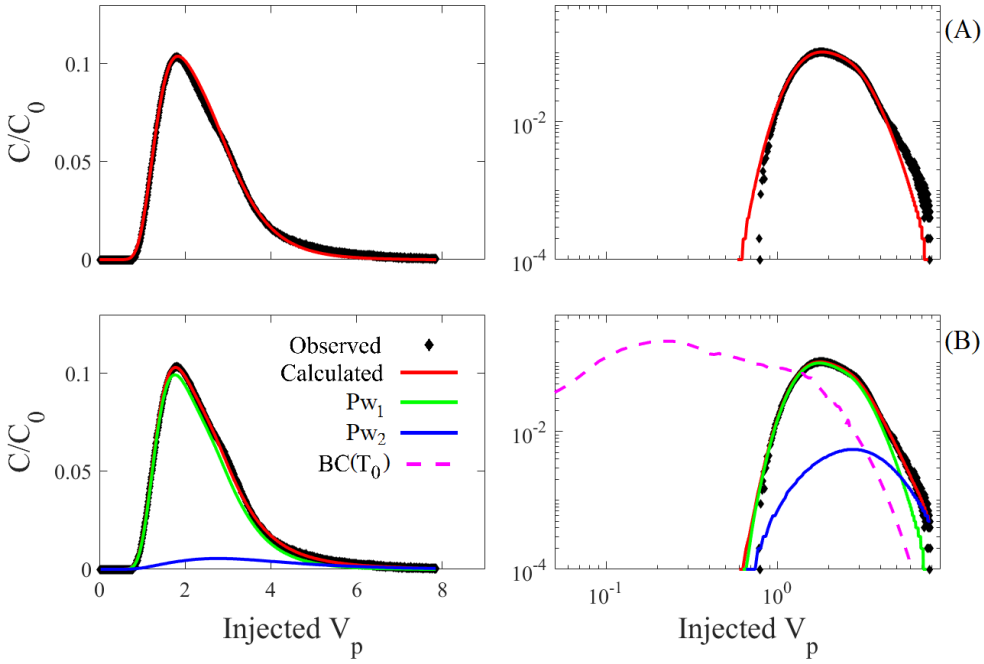

Figure 5.13: Best fit of the effective transport model resulting from the calibration of the T_0 tracer test experiment. Normalized concentrations are plotted as a function of the injected pore volumes V_p in double-log and real scale: (A) single-advection dispersion model; (B) double-advection dispersion model. The blue and green lines correspond to the contributing pathways (Pw_i). The pink dashed line corresponds to the inlet boundary concentrations (BC(T_0)).

parameters are summarized in Table 5.6. All conceptual models seem to satisfactorily reproduce the experimental breakthrough curves, with root mean square errors (RMSE) that range between $1.10{\cdot}10^{-3}$ and $4.22{\cdot}10^{-2}$ mg/L. Figures 5.13A and 5.13B show the calibration of the T_0 experiment with a single-advection and a double-advection dispersion model, respectively. The simulated breakthrough curve shown in Figure 5.13B is decomposed into the two contributing pathways, Pw_1 and Pw_2. One can visually appreciate that, even though the RMSE is slightly larger, the double-advection model better captures the early arrival and the late-time behavior of the breakthrough curve. The second pathway Pw_2 (with a contribution of about 10%) is half as fast as

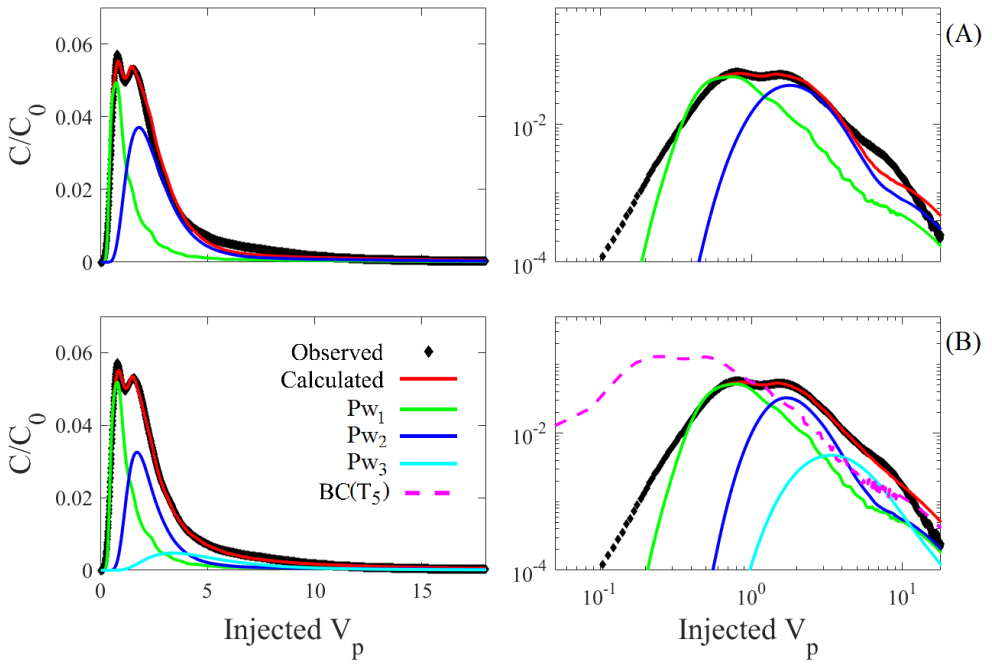

Figure 5.14: Normalized breakthrough curve concentrations resulting from the calibration of tracer test T_5. Concentrations are plotted over injected pore volumes V_p. Above (A), linear and log-log plots show measured and calculated BTC considering two-advective pathways (Pw_i). Below (B), linear and log-log plots show the experimental BTC calibrated considering three-advective pathways. The pink dashed line correspond to inlet boundary concentrations (BC(T_5)).

Pw_1 and it is characterized by a much higher dispersivity (α=3.7 cm). This pathway is key to reproducing the inflection point and the late-time concentrations. The high dispersivity of Pw_2 suggests that this slow pathway represents a part of the porous media where larger variations in local velocities occur due to the slight initial stratification.

Figure 5.14A shows the best fit between the T_5 experimental breakthrough curve and the double-advective dispersion model. The simulated breakthrough curve reproduces satisfactorily the overall transport behavior, with a root

mean square error of $4.22{\cdot}10^{-2}$ mg/L. The model properly reproduces the two peaks, each one corresponding to a different pathway. The contribution of the fastest pathway is 40% with an estimated velocity of about 3.7 cm/min. This velocity is almost four times larger than that of the secondary pathway, which resembles the velocity of the initial porous medium obtained in the T_0 experiment (primary velocity). However, the simulated breakthrough curve cannot properly represent the tail and the early times. For this reason, we further examined an effective transport model with 3 equivalent pathways. Figure 5.14B shows the best fit of the breakthrough curve with a root mean square error of $2.12{\cdot}10^{-2}$ mg/L. The first peak of the breakthrough curve is mostly described by the first pathway Pw_1 with similar contribution as before (β_1 changed from 40 to 42.4%). However, the previous second pathway is decomposed now into two. A slightly faster path with a contribution of $\beta_2 = 0.42$, characterized by half of the previous dispersivity, and another one with slower velocity but greater dispersivity. It is worth noting that transport parameters and contribution of the latter resemble those of the second pathway considered for the matrix system (when interpreted by the double-advective dispersion model). A visual inspection of the fit suggest that the 3-pathway model provides a more adequate description of the tail, even though

Table 5.6: Results of model calibration of both prior- (T_0) and post-dissolution (T_5) tracer test interpretation.

	T_0			T_5				
N_p	1	2		2		3		
N. Parameters	2	5		5		8		
v_i (cm/min)	0.82	0.87	0.4	3.7	0.73	3.2	0.85	0.28
α_i (cm)	0.89	0.71	3.7	0.9	2.63	1	1.33	3.7
β_i	1	0.9	0.1	0.4	0.6	0.425	0.42	0.155
RMSE (mg/L)	$1.1{\cdot}10^{-3}$	$1.3{\cdot}10^{-3}$		$4.22{\cdot}10^{-2}$		$2.12{\cdot}10^{-2}$		

*Note.*The table shows, for each calibrated model, the number of pathways that define the transport model (N_p), the number of effective parameters to calibrate (N.Parameters), calibrated values of flow velocity v, dispersivity α and contribution β for each pathway, as well as the root mean square error (RMSE).

still some errors in reproducing the early and late time behavior can be observed.

Physical Interpretation of Effective Parameters

Results show so far that wormholes accentuate the differences between the more mobile and less mobile flow paths. This effect is well captured by the effective multi-advection dispersion model with few equivalent flow pathways. The nice fit with this model suggests that mass transfer processes between flow pathways were not relevant in this case, mostly like because the residence time in the synthetic aquifer was small relative to the time-scales of mass transfer. We now seek for a correspondence between equivalent model pathways and groups of wormholes identified through image analysis. This can give us further insights about the physical interpretation of the effective parameters. To do this, we associate groups of wormholes with equivalent flow pathways of the transport model by assuming that wormhole groups G_i of similar length L_i (Table 5.5) simultaneously contribute to the same model pathway. Table 5.7 provides a summary of the adopted correspondence between model pathways and wormhole groups. Then, we estimate β_i based on physical grounds as the ratio between the sum of capture areas ω_i (estimated from image analysis) associated with the ith pathway and the total width of the reservoir ω,

$$\beta_i = \frac{Q_i}{Q} \approx \frac{1}{\omega} \sum_{\omega_i \in \beta_i} \omega_i \tag{5.20}$$

This estimation of β_i matches quite well with the corresponding effective values (Table 5.7). This means that the fastest equivalent flow pathway (green line in Figures 5.14A and B) represents solute transport through dominant (longest) wormholes, associated in this case with groups G_2 and G_8. On the contrary, the less important flow pathway seems to represent solute transport through the matrix (porous media not affected by dissolution). This can be seen for instance by the similarity between the estimated values of β_2 and

Table 5.7: Contribution β_i of individual pathways to the composite BTC of tracer test T_5.

N_p	Parameter	From capture areas ω_i	Calibrated model	Wormholes Groups	BTC Color Line
2	β_1	0.41	0.4	G_2, G_8	—
	β_2	0.59	0.6	G_1, G_2-G_7	—
3	β_1	0.41	0.425	G_2, G_8	—
	β_2	0.49	0.420	G_1, G_3, G_5, G_6	—
	β_3	0.10	0.155	G_4, G_7	—

Note. We compare the contribution estimates obtained from BTCs calibration and those obtained from capture areas previously calculated through image analysis. In column 5 we highlight the groups of wormholes associated to each pathway considered for the calibration while the coloured lines help visualizing the correspondence with pathways plotted in Figure 5.14.

α_2 in the matrix system (T_0 experiment) and β_3 and α_3 in the wormhole formation (T_5 experiment). Here a large scale triggering factor can be seen; the more permeable matrix ($\beta_1(T_0)$) concentrates the majority of the dissolution pattern development ($\beta_{1-2}(T_5)$) during dissolution experiment, whereas the less permeable areas (β_2 (T_0)) remain almost undissolved ($\beta_3(T_5)$).

Discrete Wormhole Transport Modeling

Results shown in section 5.3.2 suggest that one can estimate the effective hydraulic conductivity of a karstified system from the geometry of the wormhole channel patterns. In the same vein, in this section, we study if it is possible to make a direct prediction of solute transport from the geometry of wormholes and the transport parameters of the undissolved matrix (v_0 and α_0). The answer to this question is crucial for making long-term predictions of mobile resources exploited in aquifers characterized by preferential-flow dissolution structures. In this context, we carry out a blind prediction of the T_5 tracer test breakthrough curve using the discrete wormhole transport model defined in equation (5.16). We consider 20 flow pathways which represent the 20 wormholes previously identified in section 5.3.1. The flow contribution of each

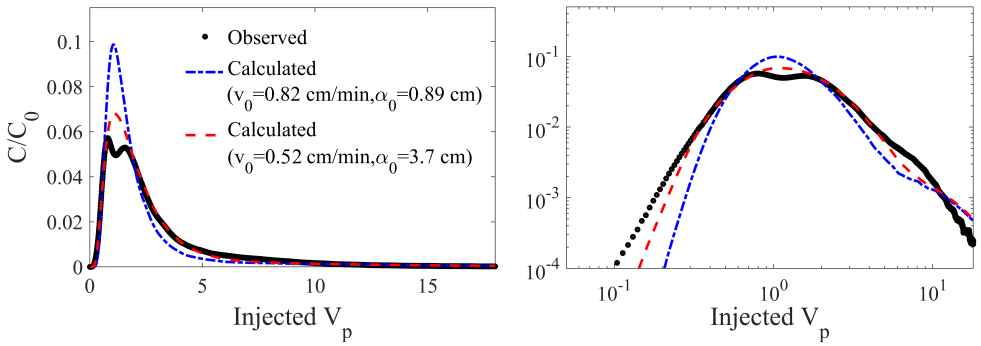

Figure 5.15: Normalized breakthrough curve concentrations resulting from two blind predictions of tracer test T_5 (Eq. 5.16). Concentrations are plotted over injected pore volumes V_p. The blu dashed BTC results from considering transport parameters of $Pw_1(T_0)$ while the red BTC is characterized by adjusted transport parameters.

pathway is determined by the wormhole capture areas calculated from equation (5.4) and summarized in Table 5.4 jointly with their length L_i. We first consider the matrix system as characterized by parameters $v_0 = 0.82$ cm/min and $\alpha_0 = 0.89$ cm, previously calibrated for reproducing transport behavior in the undissolved matrix (T_0, table 5.6). Nevertheless, we are aware that the assumptions made for the discrete wormhole model are not fully fulfilled at the experimental level. Thus, we carry out a further prediction adjusting v_0 and α_0.

In Figure 5.15 we compare the results with the measured BTC. The proposed conceptual model (B) surprisingly captures the overall transport behavior in both predictions, with a RMSE of respectively $1.7{\cdot}10^{-1}$ mg/L and $6.27{\cdot}10^{-2}$ mg/L. Employing the parameters of the calibrated effective model (T_0), the mean velocity of the experimental breakthrough curve is well captured as well, although the model overestimates the maximum concentration and fails to properly reproduce the double-peak in the breakthrough curve. The prediction notably improves applying a lower velocity ($v_0 = 0.52$ cm/min) and a higher dispersivity ($\alpha_0 = 3.7$ cm). A possible explanation is

that the experiment slightly departs from the assumptions we made, since i) the wormholes do not grow in a straight line as described in the conceptual model, ii) the flow does not enter into the matrix exclusively from the tip, and iii) the flow dimension is not uniform throughout the aquifer, specially nearby the wormhole tip. These features can reasonably explain the need for both a higher dispersivity and lower mean velocity values. It is worth noting as well that in this second prediction the RMSE is close to that of the effective multi-advective model (Table 5.6). Anyway, despite the fact that we obtain similar results, we contend that the discrete wormhole model is more valuable. This model not only describes the system but also can make physically-based transport predictions in a karsified porous medium.

5.3.6 Joint discussion on experimental results

All experimental results (growth rate, wormhole density and flow distribution) are consistent with each other and suggest that the mechanism of wormhole competition is slower than that estimated numerically and analytically. Wormhole starvation is manifested farther in time (and space). The statement is true for the present and Detwiler et al. (2003)'s work. We might look for an explanation in the choice of flow boundary conditions. However, the experiments have been carried out under different conditions: Detwiler et al. (2003) sets inlet and outlet constant heads, unlike the flow rate fixed in the current experiment (section 5.2). Neither the "confinement effect" (Cohen et al., 2008) plays an important role here, since we stop the dissolution process so that the length of the largest wormhole is half the width of the aquifer. A possible explanation is that the dissolution regime reproduced during the experiment tends to a ramified regime. We want to recall that the dissolution diagram (Golfier et al., 2002) is only a guide in choosing the optimal conditions for reproducing a dominant wormhole regime. Actually, the limits change as the acid capacity number changes. A ramified regime is characterized by a high injection rate (High Pe) and the fluid is usually forced into smaller pores (Fredd and Fogler, 1998), leading to a more branched dissolution pattern. Thus, experimental conditions at the limit with the ramified regime,

i.e. high injection-rate conditions, would explain why the competition for the flow is slower than what expected and secondary wormholes grow so long. On the other hand, it could justify, jointly with features of competition, why secondary wormholes closest to the dominant ones are larger than other secondary flow-paths. During the competition, an increasing amount of flow is directed towards the dominant channels. At high injection rates, some of it would be forced into neighboring flow paths and the farthest ones would be the first to starve.

5.4 Conclusions

Wormhole formation during the dissolution of a soluble porous media controls flow and transport dynamics in karst aquifers. Optimal conditions to promote dissolution structures have been historically studied, mainly in the oil and gas field, where hydrodynamic and geochemical conditions are usually under control. However, the mechanisms underlying the spatio-temporal evolution of dissolution structures, the redistribution of flow among wormholes, and its effects on transport behavior are largely unknown. In this context, we have presented a dissolution experiment in a two-dimensional intermediate-scale synthetic aquifer that resembles an evaporitic system. Colored tracer tests have been performed during the experiment to delineate the dissolution structures and to explore transport modeling approaches. We highlight here the most important results:

- Carrying out a sequence of colored tracer tests during the dissolution experiment and recording tracer images through a digital camera allowed visualizing the evolution of the morphology of the dissolution structure.
- Tracer transport before the start of dissolution showed a slight stratification of the porous medium. This heterogeneity significantly influenced wormhole formation acting as triggering factor (front instability).
- We were able to analyze some features of wormhole dynamics and competition for flow. In particular, we observed that: i) preferential flow

channels grow linearly over time until they start dying of starvation (decrease of their growth potential until death); and ii) the longer the flow channel, the faster its growth rate (evidence of increasing growth potential). This features are clear evidences of wormhole competition for the flow. We observed as well that: iii) wormhole density evolution (i.e. wormhole distribution in time and space) converges to a linear trend, in agreement with others experimental results but not with what expected from numerical analysis; and iv) with the evolution of the dissolution pattern, most of the flow is redistributed towards the areas characterized by dominant wormholes. However, almost all channels are still active at the end of the experiment, in disagreement with what is expected based on wormhole geometry and the redistribution of flow in the aquifer. These features suggest that the competition is slower than expected. A possible explanation could be that the experimental conditions are bordering those necessary to reproduce a ramified dissolution regime, characterized by high injection-rate.

- We could analyze the changes in the hydraulic properties of the porous medium in the context of wormhole dynamics. Both the porosity and the effective hydraulic conductivity increased linearly over time up to the end of the dissolution experiment. Furthermore, the estimation of the effective hydraulic conductivity of the karstified medium from wormholes lenght agrees with experimental values. It suggests that knowing the geometry of a karstified aquifer system, it could be possible to estimate its effective hydraulic conductivity.

- The choice of the number of tracer tests to be carried out during the dissolution experiment was not easy. On the one hand, making a very close sequence of tracer tests makes image analysis difficult. On the other hand, the less number of tracer tests, the less the time resolution of wormhole development one has for visualization.

In order to understand how flow and transport behavior changes with the formation of wormholes during the dissolution of a soluble porous medium

in a context of competition, we have sought for conceptual transport models that can explain the integrated concentration breakthrough curves obtained at the tank outlet during the first and last tracer test experiments carried out under flow steady-state conditions (geochemical equilibrium). We have explored the suitability of the multi-advection dispersion model, which represents the wormhole-bearing porous media as a bundle of streamtubes with different local velocities and dispersivities. We have considered two modeling approaches. The first approach provides the best fit of the breakthrough curves with effective transport parameters. The other investigates the predictive power of a discrete wormhole modeling approach. The latter constructs the multi-advection dispersion model from the geometry of the wormhole channel pattern. Results have shown that:

- Solute transport through a wormhole-bearing porous media, characterized by highly conductive flow channels resulting from dissolution, can be effectively described by a multi-advection dispersion model with two or three streamtubes. The model is shown to properly capture the double-peak distribution of the concentrations and the early and late-time behavior of the breakthrough curves. The fastest streamtubes represent the dominant wormholes and the slowest streamtube the matrix system. The contribution of each streamtube is shown to nicely correlate with the corresponding wormhole capture areas, which characterizes the fraction of flow passing through the wormhole group. Mass transfer processes between streamtubes were not seen relevant in this case, mostly like because the residence time in the synthetic aquifer was small relative to the time-scales of mass transfer.

- The discrete wormhole model explicitly represents the geometrical properties of each individual wormhole in a transport model. Each streamtube represents an actual wormhole. The transport model is constructed from information about the longitudinal length of wormholes and the transport properties of the matrix system. The flow contribution of each

wormhole can be estimated from the wormhole competition model presented by Cabeza et al. (2020), which determines the capture area of wormholes (proportional to the flow passing through each wormhole) from their length. Results have shown that this model can be used to provide a fairly accurate blind prediction of solute transport even though the double-peak of the breakthrough curve is not properly captured.

Chapter 6

Conclusions

6.1 Overall conclusions

In this thesis, the characterization of the Salar de Atacama aquifer system has been the driving force that made us undertake different paths, through which we have applied existing methodologies and developed new ones, through which we have tried to understand, at different scales, processes and features that are governing flow and transport in an evaporitic aquifer system, through which we can now look more clearly at the SdA system as a whole, although there is still a lot to do to fully understand its dynamics. Regarding this journey, below we report the main conclusions for each chapter:

- in Chapter 2 we emphasized the importance of characterizing an aquifer system interpreting recovery data, as they are not only as quantitatively and qualitatively valuable as pumping data, but also less influenced by pumping perturbations. We validated Agarwal's method, that result to be a great choice for recovery data interpretation under ideal conditions as well under non-ideal conditions in the case of fully radial regime development. Otherwise, for non-radial regimes, as well for short pumping periods (or far observation wells), the proposed method is shown to overcome Agarwal's limitations. Lastly, we showed up a new "equivalent time" that allows interpreting recovery data accounting for pumping rate variability, either in ideal nor non-ideal conditions.
- in Chapter 3 we proposed a filtering-corrective method that, jointly with the inverse problem, allows filtering systematic errors in drawdown estimates (errors arising from the modelling and measuring process) during the calibration of a groundwater model (synthetic scenario). We demonstrated the capability of the method for obtaining very good estimates in terms of drawdowns and hydraulic properties, even when absolute head data is strongly biased. Above all, we emphasized the effectiveness of estimating natural heads by mean of a flow numerical model and introducing a corrective term for a good drawdown estimation and model calibration. Lastly, we showed that the use of biased

absolute head data in the traditional inverse problem can also provide good fittings but, in this case, the bias leads to an incorrect solution.

- in Chapter 4 we investigated the possibility of characterizing connectivity structures in an evaporitic aquifer of great extension (i.e. the Salar de Atacama) by means of hydraulic testing and stochastic inversion. We concluded that the applied methodology allowed to identify the presence of these connective structures that seem to govern the flow dynamics of the system. Anyway, the location of preferential flow-paths could not be defined from the applied method itself. Thus, we emphasized the importance of dealing with independent information: the consistency among results from different sets of information and methodologies increased the reliability of results themselves and the knowledge of the overall system.

- in Chapter 5 we investigated the features of wormhole dynamics and the effects of dissolution pattern development on flow and transport behavior by mean of an intermediate-scale dissolution experiment coupled with several tracer tests. Above all, we emphasized the capability of visualizing the spatio-temporal evolution of the dissolution structure, which allowed analysing the main features of wormholes development. We could observe some evidence of the triggering and amplifying factors involved in the self-organization mechanism that lead to the development of preferential flow-paths. Furthermore, from the interpretation of the tracer tests we could determine the suitability of the multi-advection dispersion model for reproducing the transport behavior in the porous medium with wormholes. Finally, we emphasized the worth of the discrete wormhole model that is shown to have a high predictive power.

Appendix A

Porosity Changes from Total Mass Measurements

The total mass M_{tot} continuously recorded by the scale can be written as

$$M_{tot} = V_t\rho_t + V_i\rho_{B1} + V_m\phi_m\rho_{B1} + V_m(1-\phi_m)\rho_s + V_o\phi_o\rho_{B1} + V_o(1-\phi_o)\rho_{B1}, \tag{A.1}$$

where V_t and ρ_t are respectively volume and density of the tank skeleton itself. V_i, V_m and V_o are the volumes of the inlet (i), main (m) and outlet (o) reservoirs and ϕ_m, ϕ_o their porosity ($\phi_i = 1$). ρ_{B1} is the density of the brine and ρ_s the one of the Halite. The mass of the tank skeleton, as well the mass of inlet and outlet reservoir are assumed constant throughout the experiment. As the kinetic is almost instantaneous, we assume the main reservoir to be filled with saturated brine.

Thus, mass changes due to porosity changes can be written as

$$\Delta M_{tot} = V_m(\phi_{s1} - \phi_{s2})\rho B1 + V_m(1-\phi_{s1})\rho_s - V_m(1-\phi_{s2})\rho_s, \tag{A.2}$$

$$\Delta M_{tot} = V_m(\phi_{s1} - \phi_{s2})(\rho_{B1} - \rho_s), \tag{A.3}$$

and,

$$\Delta\phi = \frac{\Delta M_{tot}}{V_m \Delta\rho} \tag{A.4}$$

Appendix B

Publications

AGU100 ADVANCING EARTH AND SPACE SCIENCE

Water Resources Research

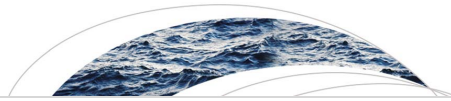

RESEARCH ARTICLE
10.1029/2018WR022684

Key Points:
- The validity of Agarwal's method under ideal and non-ideal conditions is analyzed
- An alternative method is developed to overcome Agarwal's limitations, leading to a better interpretation, especially for early times data
- A new equivalent time is proposed to take into consideration the variable pumping rate during the recovery data interpretation process

Correspondence to:
M. Trabucchi,
trabucchi.michela@gmail.com

Citation:
Trabucchi, M., Carrera, J., & Fernàndez-Garcia, D. (2018). Generalizing Agarwal's method for the interpretation of recovery tests under non-ideal conditions. *Water Resources Research*, *54*. https://doi.org/10.1029/2018WR022684

Received 31 JAN 2018
Accepted 25 JUL 2018
Accepted article online 3 AUG 2018

Generalizing Agarwal's Method for the Interpretation of Recovery Tests Under Non-Ideal Conditions

Michela Trabucchi[1,2], Jesús Carrera[1,3], and Daniel Fernàndez-Garcia[1,2]

[1]Associated Unit: Hydrogeology Group (UPC-CSIC), Barcelona, Spain, [2]Department of Civil and Environmental Engineering, Universitat Politècnica de Catalunya (UPC), Barcelona, Spain, [3]Institute of Environmental Assessment and Water Research (IDAEA), CSIC, Barcelona, Spain

Abstract Pumping tests are performed during aquifer characterization to gain conceptual understanding about the system through diagnostic plots and to estimate hydraulic properties. Recovery tests consist of measuring head response in observation and/or pumping wells after pumping termination. They are especially useful when the pumping rate cannot be accurately controlled. They have been traditionally interpreted using Theis' recovery method, which yields robust estimates of effective transmissivity but does not provide information about the conceptual model. Agarwal proposed a method that has become standard in the oil industry, to obtain both early and late time reservoir responses to pumping from recovery data. However, the validity of the method has only been tested to a limited extent. In this work, we analyze Agarwal's method in terms of both drawdowns and log derivatives for non-ideal conditions: leaky aquifer, presence of boundaries, and one-dimensional flow. Our results show that Agarwal's method provides excellent recovery plots (i.e., the drawdown curve that would be obtained during pumping) and parameter estimates for nearly all aquifer conditions, provided that a constant pumping rate is used and the log derivative at the end of pumping is constant, which is too limiting for groundwater hydrology practice, where observation wells are usually monitored. We generalize Agarwal's method by (1) deriving an improved equivalent time for time-dependent pumping rate and (2) proposing to recover drawdown curves by extrapolating the pumping phase drawdowns. These yield excellent diagnostic plots, thus facilitating the conceptual model analysis for a broad range of conditions.

1. Introduction

Hydraulic testing is the most widely used technique for aquifer systems characterization and the only one providing direct estimates of aquifer parameters through the interpretation of the aquifer response to pumping or other hydraulic perturbations. Well testing results are a function of the range and the quality of the drawdown and rate data available and of the approach used for their interpretation (Gringarten, 2008).

Pumping test interpretation emerged largely from the Theis (1935) analytical solution for the drawdown caused in an ideal homogeneous, infinite, and confined aquifer by pumping at a constant rate Q from a fully penetrating well. A feature of this solution is that, when sufficient time has elapsed since the beginning of pumping, the drawdown increases linearly with the logarithm of time. This feature prompted Cooper and Jacob (1946; CJ in the following) to develop the straight line method for applying Theis' method through a manageable logarithmic approximation of the analytical solution, which works very well also for a broad range of conditions, including heterogeneous formations (Halford et al., 2006; Meier et al., 1998).

Rereading the paper of Theis (1935) is joyful, because he himself identified the numerous limitations of his solution (we suspect that his USGS colleagues and reviewers must have helped). In reality, aquifers are rarely homogeneous or fully confined and they have boundaries. Storage release is not instantaneous but delayed with respect to head variations. Wells do not fully penetrate the aquifer and may have significant storage. Over the years, hydrologists and oil engineers developed numerous analytical solutions to overcome these limitations (see, e.g., Kruseman & de Ridder, 1990). While the main purpose of these methods was to estimate transmissivity T and storage coefficient S, they realized that drawdown curves contain a wealth of information about the well and the aquifer beyond the actual value of hydraulic parameters. Unfortunately, the large number of solutions and the subtle variations among them made it difficult to identify which one is best.

Water Resources Research

RESEARCH ARTICLE
10.1029/2020WR028097

Automatic Calibration of Groundwater Models With Bias Correction and Data Filtering: Working With Drawdown Data

Michela Trabucchi[1,2], **Daniel Fernàndez-Garcia**[1,2], **and Jesús Carrera**[1,3]

[1]Associated Unit: Hydrogeology Group (UPC-CSIC), Barcelona, Spain, [2]Department of Civil and Environmental Engineering, Universitat Politècnica de Catalunya (UPC), Barcelona, Spain, [3]Institute of Environmental Assessment and Water Research (IDAEA), CSIC, Barcelona, Spain

Key Points:

- We estimates drawdowns caused by hydraulic testing to characterize a complex aquifer system
- We employ a numerical groundwater model to calculate natural heads to de-trend head measurements
- We introduce a corrective factor to remove errors that arise in the modeling and measuring process

Correspondence to:
M. Trabucchi,
trabucchi.michela@gmail.com

Citation:
Trabucchi, M., Fernàndez-Garcia, D., & Carrera, J. (2021). Automatic calibration of groundwater models with bias correction and data filtering: Working with drawdown data. *Water Resources Research*, *57*, e2020WR028097. https://doi.org/10.1029/2020WR028097

Received 8 JUN 2020
Accepted 11 FEB 2021

Abstract The drawdown response to a hydraulic stress contains crucial information to characterize an aquifer. Modeling drawdowns is far easier than modeling heads because they are subject to homogeneous (zero) internal sink/sources, and boundary and initial conditions. The problem lies on the fact that drawdowns are not measured directly but derived from measurements of head fluctuations. Resulting drawdowns may suffer persistent inaccuracies in complex systems with uncertain long-acting external stresses, so that they are affected not only by errors in head measurements, but also in estimates of the natural head evolution. This hinders the use of drawdowns in groundwater models, and forces modelers to employ absolute heads and soft information. In this context, we present a method to filter systematic errors in drawdown data during the calibration of a groundwater model. To do this, we introduce a bias correction term in a composite inverse problem that combines a natural head model with a drawdown model. Since these two models share the same parameters, a two-stage iterative optimization algorithm is developed to jointly estimate the bias, natural trends, and parameters. The method is illustrated by a synthetic example in a heterogeneous aquifer. The example shows that the method converges to the best conditional estimate even when absolute head data is strongly biased. In the same example, we demonstrate that the use of biased absolute head data in the traditional inverse problem can also provide good fittings but, in this case, the bias leads to an incorrect estimation of the transmissivity field.

1. Introduction

Hydraulic tests are typically used to characterize aquifers by analyzing the aquifer response to a known imposed stress. The term test is used here in a broad sense, including any perturbation to the normal functioning of the aquifer, such as pumping tests, stream-stage tests, or in general known water production periods. In any of these cases, the aquifer response to pumping or other hydraulic perturbations contains valuable information about the conceptual model and hydraulic properties (e.g., Domenico et al., 1998; Freeze & Cherry, 1979; Gringarten et al., 2008; Renard, 2006; Trabucchi et al., 2018). The response must be not only properly measured but also processed and interpreted to extract such information. The procedure usually involves fitting water level changes or drawdown to a mathematical model.

The definition of drawdown is well-known, simple and intuitive, but we want to briefly recall it to argue why modeling drawdowns, rather than heads, in the context of transient model calibration may be the best choice for aquifer test interpretation. Drawdown is defined as the difference between two heads: $s = h_n - h$, where h is the actually observed head resulting from the hydraulic test, and h_n is the natural head evolution (i.e., the head that would have been measured if the hydraulic test had not been performed). As a result, as we will show later, drawdown models enjoy homogeneous initial and boundary conditions (i.e., boundary and initial drawdowns are zero and boundary and internal sink/source terms are zero). This is advantageous because it avoids the problem of defining initial and boundary conditions during groundwater modeling (Renard, 2006). Only the stress that causes the drawdown, which should be well known, needs to be specified. At the same time, it allows one to avoid working with absolute heads, which are characterized by weak dependence on hydraulic properties and represent the solution to a differential equation with complex boundary and initial conditions (Renard, 2006). The downside of working with drawdowns lies on the fact that they do not inform directly about the functioning of the aquifer (i.e., where water comes from

Bibliography

Ram G Agarwal et al. A new method to account for producing time effects when drawdown type curves are used to analyze pressure buildup and other test data. 1980.

Andrés Alcolea, Jesús Carrera, and Agustín Medina. Pilot points method incorporating prior information for solving the groundwater flow inverse problem. *Advances in Water Resources*, 29(11):1678 – 1689, 2006. ISSN 0309-1708. doi: https://doi.org/10.1016/j.advwatres.2005.12.009. URL http://www.sciencedirect.com/science/article/pii/S0309170805002976.

Andrés Alcolea, Eduardo Castro, Manuela Barbieri, Jesus Carrera, and Sergio Bea. Inverse modeling of coastal aquifers using tidal response and hydraulic tests. *Groundwater*, 45(6):711–722, 2007. doi: 10.1111/j.1745-6584.2007.00356.x. URL https://ngwa.onlinelibrary.wiley.com/doi/abs/10.1111/j.1745-6584.2007.00356.x.

Andrés Alcolea, Jesús Carrera, and Agustín Medina. Regularized pilot points method for reproducing the effect of small scale variability: Application to simulations of contaminant transport. *Journal of Hydrology*, 355(1):76 – 90, 2008. ISSN 0022-1694. doi: https://doi.org/10.1016/j.jhydrol.2008.03.004. URL http://www.sciencedirect.com/science/article/pii/S0022169408001297.

Marwan Alkattan, Eric H. Oelkers, Jean-Louis Dandurand, and Jacques Schott. Experimental studies of halite dissolution kinetics, 1 the effect of saturation state and the presence of trace metals. *Chemical Geology*, 137(3):201–219, 1997. ISSN 0009-2541. doi: https://doi.org/10.1016/S0009-2541(96)

00164-7. URL https://www.sciencedirect.com/science/article/pii/S0009254196001647.

Pietro de Anna, Joaquin Jimenez-Martinez, Herve Tabuteau, Regis Turuban, Tanguy Le Borgne, Morgane Derrien, and Yves Meheust. Mixing and reaction kinetics in porous media: An experimental pore scale quantification. *Environmental science & technology*, 48(1):508–516, 2014. doi: https://doi.org/10.1021/es403105b.

Javad Ashjari. Determination of storage coefficients during pumping and recovery. *Groundwater*, 51(1):122–127, 2013. doi: doi:10.1111/j.1745-6584.2012.00917.x.

B. Ataie-Ashtiani, R. E. Volker, and D. A. Lockington. Tidal effects on groundwater dynamics in unconfined aquifers. *Hydrological Processes*, 15 (4):655–669, 2001. doi: https://doi.org/10.1002/hyp.183. URL https://onlinelibrary.wiley.com/doi/abs/10.1002/hyp.183.

PN Ballukraya and KK Sharma. Estimation of storativity from recovery data. *Groundwater*, 29(4):495–498, 1991.

Olivier Banton and Lumony Mulongo Bangoy. A new method to determine storage coefficient from pumping test recovery data. *Ground Water*, 34(5): 772–777, 1996.

B Bazin et al. From matrix acidizing to acid fracturing: a laboratory evaluation of acid/rock interactions. *SPE Production & Facilities*, 16(01):22–29, 2001. doi: https://doi.org/10.2118/66566-PA.

Steven J. Berg and Walter A. Illman. Field study of subsurface heterogeneity with steady-state hydraulic tomography. *Groundwater*, 51(1):29–40, 2013. doi: 10.1111/j.1745-6584.2012.00914.x.

BGR, IAH, KIT, and UNESCO. *World Karst Aquifer Map, 1: 40000000*. Berlin, Reading, Karlsruhe, Paris, 2017.

Marco Bianchi, Chunmiao Zheng, Crystal Wilson, Geoffrey R. Tick, Gaisheng Liu, and Steven M. Gorelick. Spatial connectivity in a highly heterogeneous aquifer: From cores to preferential flow paths. *Water Resources Research*, 47(5), 2011. doi: 10.1029/2009WR008966. URL https://agupubs.onlinelibrary.wiley.com/doi/abs/10.1029/2009WR008966.

Yuksel K Birsoy and WK Summers. Determination of aquifer parameters from step tests and intermittent pumping data. *Groundwater*, 18(2):137–146, 1980.

Dominique Bourdet, TM Whittle, AA Douglas, and YM Pirard. A new set of type curves simplifies well test analysis. *World oil*, 196(6):95–106, 1983.

Dominique Bourdet, JA Ayoub, YM Pirard, et al. Use of pressure derivative in well test interpretation. *SPE Formation Evaluation*, 4(02):293–302, 1989.

David F. Boutt, Scott A. Hynek, Lee Ann Munk, and Lilly G. Corenthal. Rapid recharge of fresh water to the halite-hosted brine aquifer of salar de atacama, chile. *Hydrological Processes*, 30(25):4720–4740, 2016. doi: 10.1002/hyp.10994. URL https://onlinelibrary.wiley.com/doi/abs/10.1002/hyp.10994.

W. F. Brace. Permeability of crystalline rocks: New in situ measurements. *Journal of Geophysical Research: Solid Earth*, 89(B6):4327–4330, 1984. doi: 10.1029/JB089iB06p04327. URL https://agupubs.onlinelibrary.wiley.com/doi/abs/10.1029/JB089iB06p04327.

W.F. Brace. Permeability of crystalline and argillaceous rocks. *International Journal of Rock Mechanics and Mining Sciences & Geomechanics Abstracts*, 17(5):241 – 251, 1980. ISSN 0148-9062. doi: https://doi.org/10.1016/0148-9062(80)90807-4. URL http://www.sciencedirect.com/science/article/pii/0148906280908074.

R. Brauchler, R. Hu, L. Hu, S. Jiménez, P. Bayer, P. Dietrich, and T. Ptak. Rapid field application of hydraulic tomography for resolving aquifer heterogeneity in unconsolidated sediments. *Water Resources Research*, 49(4):2013–2024,

2013. doi: 10.1002/wrcr.20181. URL https://agupubs.onlinelibrary.wiley.com/doi/abs/10.1002/wrcr.20181.

Agnieszka Budek and Piotr Szymczak. Network models of dissolution of porous media. *Phys. Rev. E*, 86:056318, Nov 2012. doi: 10.1103/PhysRevE.86.056318. URL https://link.aps.org/doi/10.1103/PhysRevE.86.056318.

Marten A Buijse et al. Understanding wormholing mechanisms can improve acid treatments in carbonate formations. In *SPE European Formation Damage Conference*. Society of Petroleum Engineers, 1997. doi: https://doi.org/10.2118/38166-MS.

Yoar Cabeza, Juan J. Hidalgo, and Jesus Carrera. Competition is the underlying mechanism controlling viscous fingering and wormhole growth. *Geophysical Research Letters*, 47(3):e2019GL084795, 2020. doi: https://doi.org/10.1029/2019GL084795.

M. L. Calvache, J. P. Sánchez-Úbeda, C. Duque, M. López-Chicano, and B. de la Torre. Evaluation of analytical methods to study aquifer properties with pumping tests in coastal aquifers with numerical modelling (Motril-Salobreña Aquifer). *Water Resources Management*, 30(2):559–575, Jan 2016. ISSN 1573-1650. doi: 10.1007/s11269-015-1177-6. URL https://doi.org/10.1007/s11269-015-1177-6.

J. Carrera, E. Vazquez-Suñe, O. Castillo, and X. Sanchez-Vila. A methodology to compute mixing ratios with uncertain end-members. *Water Resources Research*, 40(12), 2004. doi: 10.1029/2003WR002263. URL https://agupubs.onlinelibrary.wiley.com/doi/abs/10.1029/2003WR002263.

Jesus Carrera and Shlomo P. Neuman. Estimation of aquifer parameters under transient and steady state conditions: 1. maximum likelihood method incorporating prior information. *Water Resources Research*, 22(2):199–210, 1986. doi: 10.1029/WR022i002p00199. URL https://agupubs.onlinelibrary.wiley.com/doi/abs/10.1029/WR022i002p00199.

Jesus Carrera, Xavier Sánchez-Vila, Inmaculada Benet, Agustín Medina, Germán Galarza, and Jordi Guimerà. On matrix diffusion: formulations, solution methods and qualitative effects. *Hydrogeology Journal*, 6(190):1435–0157, 1998. doi: 10.1007/s100400050143. URL https://doi.org/10.1007/s100400050143.

Steven W. Chapman, Beth L. Parker, Tom C. Sale, and Lee Ann Doner. Testing high resolution numerical models for analysis of contaminant storage and release from low permeability zones. *Journal of Contaminant Hydrology*, 136-137:106 – 116, 2012. ISSN 0169-7722. doi: https://doi.org/10.1016/j.jconhyd.2012.04.006. URL http://www.sciencedirect.com/science/article/pii/S0169772212000599.

Djaouida Chenaf and Robert P Chapuis. Methods to determine storativity of infinite confined aquifers from a recovery test. *Ground water*, 40(4):385, 2002.

Wendy Cheung and Harihar Rajaram. Dissolution finger growth in variable aperture fractures: Role of the tip-region flow field. *Geophysical Research Letters*, 29(22):32–1–32–4, 2002. doi: https://doi.org/10.1029/2002GL015196. URL https://agupubs.onlinelibrary.wiley.com/doi/abs/10.1029/2002GL015196.

Mesut Çimen. A straight-line method for analyzing residual drawdowns at an observation well. *Mathematical Problems in Engineering*, 2015(1):1–5, 2015. doi: http://dx.doi.org/10.1155/2015/978040.

Christoph Clauser. Permeability of crystalline rocks. *Eos, Transactions American Geophysical Union*, 73(21):233–238, 1992. doi: 10.1029/91EO00190. URL https://agupubs.onlinelibrary.wiley.com/doi/abs/10.1029/91EO00190.

Charles Edouard Cohen, Didier Ding, Michel Quintard, and Brigitte Bazin. From pore scale to wellbore scale: Impact of geometry on wormhole growth in carbonate acidization. *Chemical Engineering Science*, 63(12):3088 – 3099, 2008. ISSN 0009-2509. doi: https://doi.org/10.1016/j.

ces.2008.03.021. URL http://www.sciencedirect.com/science/article/pii/S0009250908001255.

HH Cooper Jr and Charles Edward Jacob. A generalized graphical method for evaluating formation constants and summarizing well-field history. *Eos, Transactions American Geophysical Union*, 27(4):526–534, 1946.

Emery A. Coppola Jr., Anthony J. Rana, Mary M. Poulton, Ferenc Szidarovszky, and Vincent W. Uhl. A neural network model for predicting aquifer water level elevations. *Groundwater*, 43(2):231–241, 2005. doi: 10.1111/j.1745-6584.2005.0003.x. URL https://ngwa.onlinelibrary.wiley.com/doi/abs/10.1111/j.1745-6584.2005.0003.x.

Nadim K Copty, Paolo Trinchero, and Xavier Sanchez-Vila. Inferring spatial distribution of the radially integrated transmissivity from pumping tests in heterogeneous confined aquifers. *Water Resources Research*, 47(5), 2011. doi: doi:10.1029/2010WR009877.

G. Daccord, R. Lenormand, and O. Liétard. Chemical dissolution of a porous medium by a reactive fluid—i. model for the "wormholing" phenomenon. *Chemical Engineering Science*, 48(1):169 – 178, 1993. ISSN 0009-2509. doi: https://doi.org/10.1016/0009-2509(93)80293-Y. URL http://www.sciencedirect.com/science/article/pii/000925099380293Y.

Gérard Daccord. Chemical dissolution of a porous medium by a reactive fluid. *Phys. Rev. Lett.*, 58:479–482, Feb 1987. doi: 10.1103/PhysRevLett.58.479. URL https://link.aps.org/doi/10.1103/PhysRevLett.58.479.

F. P. J. de Barros, D. Fernàndez-Garcia, D. Bolster, and X. Sanchez-Vila. A risk-based probabilistic framework to estimate the endpoint of remediation: Concentration rebound by rate-limited mass transfer. *Water Resources Research*, 49(4):1929–1942, 2013. doi: 10.1002/wrcr.20171. URL https://agupubs.onlinelibrary.wiley.com/doi/abs/10.1002/wrcr.20171.

G de Marsily. Flow and transport in fractured rocks: connectivity and scale effect. In *International symposium on the hydrogeology of rocks of low permeability.*

International Association of Hydrogeologists,Tucson, AZ (USA), pages 267–277, 1985.

G. de Marsily, G. Lavedan, M. Boucher, and G. Fasanino. Interpretation of interference tests in a well field using geostatistical techniques to fit the permeability distribution in a reservoir model. *Geostatistics for Natural Resources Characterization*, 2:831–849, 1984.

Jo De Waele, Stein-Erik Lauritzen, and Mario Parise. On the formation of dissolution pipes in quaternary coastal calcareous arenites in mediterranean settings. *Earth Surface Processes and Landforms*, 36(2):143–157, 2011. doi: https://doi.org/10.1002/esp.2022. URL `https://onlinelibrary.wiley.com/doi/abs/10.1002/esp.2022`.

L. Del Val. *Advancing in the characterization of coastal aquifers. A multimethodological approach based on fiber optics distributed temperature sensing*. PhD thesis, Universitat Politècnica de Catalunya, Jun 2020.

Russell L. Detwiler, Robert J. Glass, and William L. Bourcier. Experimental observations of fracture dissolution: The role of peclet number on evolving aperture variability. *Geophysical Research Letters*, 30(12), 2003. doi: https://doi.org/10.1029/2003GL017396. URL `https://agupubs.onlinelibrary.wiley.com/doi/abs/10.1029/2003GL017396`.

JF Devlin and CD McElwee. Effects of measurement error on horizontal hydraulic gradient estimates. *Groundwater*, 45(1):62–73, 2007. doi: 10.1111/j.1745-6584.2006.00249.x.

Patrick A Domenico, Franklin W Schwartz, et al. *Physical and chemical hydrogeology*, volume 506. Wiley New York, 1998.

Robert C Earlougher Jr, Keith M Kersch, et al. Analysis of short-time transient test data by type-curve matching. *Journal of Petroleum Technology*, 26(07): 793–800, 1974.

Owen Ralph Ewers. *Cavern development in the dimensions of length and breadth*. PhD thesis, 1982.

D. Fernandez-Garcia, G. Llerar-Meza, and J. Jaime Gómez-Hernández. Upscaling transport with mass transfer models: Mean behavior and propagation of uncertainty. *Water Resources Research*, 45(10), 2009. doi: 10.1029/2009WR007764. URL https://agupubs.onlinelibrary.wiley.com/doi/abs/10.1029/2009WR007764.

D. Fernàndez-Garcia, P. Trinchero, and X. Sanchez-Vila. Conditional stochastic mapping of transport connectivity. *Water Resources Research*, 46(10), 2010. doi: 10.1029/2009WR008533. URL https://agupubs.onlinelibrary.wiley.com/doi/abs/10.1029/2009WR008533.

Daniel Fernàndez-Garcia, Xavier Sánchez-Vila, and Tissa H. Illangasekare. Convergent-flow tracer tests in heterogeneous media: combined experimental–numerical analysis for determination of equivalent transport parameters. *Journal of Contaminant Hydrology*, 57(1):129 – 145, 2002. ISSN 0169-7722. doi: https://doi.org/10.1016/S0169-7722(01)00214-5.

JG Ferris, DB Knowles, RH Brown, and RW Stallman. Theory of aquifer tests: US Geological Survey Water-Supply Paper 1536-E. *E69-E174*, 1962.

Christopher N. Fredd and H. Scott Fogler. Influence of transport and reaction on wormhole formation in porous media. *AIChE Journal*, 44(9):1933–1949, 1998. doi: https://doi.org/10.1002/aic.690440902. URL https://aiche.onlinelibrary.wiley.com/doi/abs/10.1002/aic.690440902.

RA Freeze and John A Cherry. Groundwater. Pretice-Hall. *Inc., Englewood Cliffs, NJ*, 1979.

C.A. Garcia, K.J. Halford, and J.M. Fenelon. Detecting drawdowns masked by environmental stresses with water-level models. *Groundwater*, 51(3):322–332, 2013. doi: https://doi.org/10.1111/gwat.12042. URL https://ngwa.onlinelibrary.wiley.com/doi/abs/10.1111/gwat.12042.

J. Jaime Gómez-Hernánez, Andrés Sahuquillo, and José E. Capilla. Stochastic simulation of transmissivity fields conditional to both transmissivity and piezometric data—i. theory. *Journal of Hydrology*, 203(1):162 – 174,

1997a. ISSN 0022-1694. doi: https://doi.org/10.1016/S0022-1694(97)00098-X. URL http://www.sciencedirect.com/science/article/pii/S002216949700098X.

J. Jaime Gómez-Hernánez, Andrés Sahuquillo, and José E. Capilla. Stochastic simulation of transmissivity fields conditional to both transmissivity and piezometric data—i. theory. *Journal of Hydrology*, 203(1):162 – 174, 1997b. ISSN 0022-1694. doi: https://doi.org/10.1016/S0022-1694(97)00098-X. URL http://www.sciencedirect.com/science/article/pii/S002216949700098X.

F Golfier, B Bazin, Cesar Zarcone, R Lernormand, D Lasseux, Michel Quintard, et al. Acidizing carbonate reservoirs: numerical modelling of wormhole propagation and comparison to experiments. In *SPE European Formation Damage Conference*. Society of Petroleum Engineers, 2001. doi: https://doi.org/10.2118/68922-MS.

F Golfier, Cesar Zarcone, B Bazin, R Lenormand, D Lasseux, and Michel Quintard. On the ability of a darcy-scale model to capture wormhole formation during the dissolution of a porous medium. *Journal of fluid Mechanics*, 457: 213, 2002.

Alain C Gringarten, Dominique P Bourdet, Pierre A Landel, Vladimir J Kniazeff, et al. A comparison between different skin and wellbore storage type-curves for early-time transient analysis. pages 1–11, 1979.

Alain C Gringarten et al. From straight lines to deconvolution: The evolution of the state of the art in well test analysis. *SPE Reservoir Evaluation & Engineering*, 11(01):41–62, 2008. doi: 10.2118/102079-PA.

Christopher G. Groves and Alan D. Howard. Early development of karst systems: 1. preferential flow path enlargement under laminar flow. *Water Resources Research*, 30(10):2837–2846, 1994. doi: https://doi.org/10.1029/94WR01303. URL https://agupubs.onlinelibrary.wiley.com/doi/abs/10.1029/94WR01303.

Hoshin V. Gupta, Martyn P. Clark, Jasper A. Vrugt, Gab Abramowitz, and Ming Ye. Towards a comprehensive assessment of model structural adequacy. *Water Resources Research*, 48(8), 2012. doi: 10.1029/2011WR011044. URL https://agupubs.onlinelibrary.wiley.com/doi/abs/10.1029/2011WR011044.

C. Haas, R. Horn, R.H. Ellerbrock, and H.H. Gerke. Fluorescence imaging for mm-scale observation of macropore-matrix mass transfer: Calibration experiments. *Geoderma*, 360:114002, 2020. ISSN 0016-7061. doi: https://doi.org/10.1016/j.geoderma.2019.114002. URL https://www.sciencedirect.com/science/article/pii/S0016706119301752.

Roy Haggerty and Steven M. Gorelick. Multiple-rate mass transfer for modeling diffusion and surface reactions in media with pore-scale heterogeneity. *Water Resources Research*, 31(10):2383–2400, 1995. doi: 10.1029/95WR10583. URL https://agupubs.onlinelibrary.wiley.com/doi/abs/10.1029/95WR10583.

Roy Haggerty, Sean A. McKenna, and Lucy C. Meigs. On the late-time behavior of tracer test breakthrough curves. *Water Resources Research*, 36(12):3467–3479, 2000. doi: 10.1029/2000WR900214. URL https://agupubs.onlinelibrary.wiley.com/doi/abs/10.1029/2000WR900214.

Keith Halford, C Amanda Garcia, Joe Fenelon, and Benjamin B Mirus. Advanced methods for modeling water-levels and estimating drawdowns with seriessee, an excel add-in. Technical report, US Geological Survey, 2012.

Keith J Halford. *Documentation of a spreadsheet for time-series analysis and drawdown estimation*. US Geological Survey, 2006.

Keith J Halford and Tracie R Jackson. Groundwater characterization and effects of pumping in the death valley regional groundwater flow system, nevada and california, with special reference to devils hole. Technical report, US Geological Survey, 2020.

Keith J Halford, Willis D Weight, and Robert P Schreiber. Interpretation of transmissivity estimates from single-well pumping aquifer tests. *Groundwater*, 44(3):467–471, 2006. doi: 10.1111/j.1745-6584.2005.00151.x.

Yonghong Hao, Tian-Chyi J. Yeh, Jianwei Xiang, Walter A. Illman, Kenichi Ando, Kuo-Chin Hsu, and Cheng-Haw Lee. Hydraulic tomography for detecting fracture zone connectivity. *Groundwater*, 46(2):183–192, 2008. doi: 10.1111/j.1745-6584.2007.00388.x. URL `https://ngwa.onlinelibrary.wiley.com/doi/abs/10.1111/j.1745-6584.2007.00388.x`.

Christopher V. Henri, Daniel Fernàndez-Garcia, and Felipe P. J. de Barros. Probabilistic human health risk assessment of degradation-related chemical mixtures in heterogeneous aquifers: Risk statistics, hot spots, and preferential channels. *Water Resources Research*, 51(6):4086–4108, 2015. doi: 10.1002/2014WR016717.

Mary Catherine Hill. *A computer program (MODFLOWP) for estimating parameters of a transient, three-dimensional, ground-water flow model using nonlinear regression*. US Geological Survey Denver, CO, USA, 1992. doi: https://doi.org/10.3133/ofr91484.

David L. Hochstetler, Warren Barrash, Carsten Leven, Michael Cardiff, Francesco Chidichimo, and Peter K. Kitanidis. Hydraulic tomography: Continuity and discontinuity of high-k and low-k zones. *Groundwater*, 54 (2):171–185, 2016. doi: https://doi.org/10.1111/gwat.12344. URL `https://ngwa.onlinelibrary.wiley.com/doi/abs/10.1111/gwat.12344`.

M. L. Hoefner and H. S. Fogler. Pore evolution and channel formation during flow and reaction in porous media. *AIChE Journal*, 34(1):45–54, 1988. doi: https://doi.org/10.1002/aic.690340107. URL `https://aiche.onlinelibrary.wiley.com/doi/abs/10.1002/aic.690340107`.

John Houston, Andrew Butcher, Peter Ehren, Keith Evans, and Linda Godfrey. The Evaluation of Brine Prospects and the Requirement for Modifications to

Filing Standards. *Economic Geology*, 106(7):1225–1239, 11 2011. ISSN 0361-0128. doi: 10.2113/econgeo.106.7.1225. URL https://doi.org/10.2113/econgeo.106.7.1225.

G. Huerta. Evaluation of Chemical Patterns in Brines in the Salar de Atacama, Northern Chile: A Chemical and Isotopic approach. Master's thesis, University of Waterloo, 2012.

Bjørn Jamtveit and Paul Meakin. Growth, dissolution and pattern formation in geosystems. In *Growth, Dissolution and Pattern Formation in Geosystems*, pages 1–19. Springer, 1999. doi: https://doi.org/10.1007/978-94-015-9179-9_1.

T.E. Jordan, N. Muñoz, M. Hein, T. Lowenstein, L. Godfrey, and J. Yu. Active faulting and folding without topographic expression in an evaporite basin, Chile. *GSA Bulletin*, 114(11):1406–1421, 11 2002. ISSN 0016-7606. doi: 10.1130/0016-7606(2002)114<1406:AFAFWT>2.0.CO;2. URL https://doi.org/10.1130/0016-7606(2002)114<1406:AFAFWT>2.0.CO;2.

T.E. Jordan, C. Mpodozis, N. Muñoz, N. Blanco, P. Pananont, and M. Gardeweg. Cenozoic subsurface stratigraphy and structure of the salar de atacama basin, northern chile. *Journal of South American Earth Sciences*, 23(2):122 – 146, 2007. ISSN 0895-9811. doi: https://doi.org/10.1016/j.jsames.2006.09.024. URL http://www.sciencedirect.com/science/article/pii/S0895981106001180.

Nitika Kalia and Vemuri Balakotaiah. Effect of medium heterogeneities on reactive dissolution of carbonates. *Chemical Engineering Science*, 64 (2):376 – 390, 2009. ISSN 0009-2509. doi: https://doi.org/10.1016/j.ces.2008.10.026. URL http://www.sciencedirect.com/science/article/pii/S0009250908005447.

Stephanie K. Kampf, Scott W. Tyler, Cristian A. Ortiz, Jose F. Muñoz, and Paula L. Adkins. Evaporation and land surface energy budget at the salar de atacama, northern chile. *Journal of Hydrology*, 310(1):236 – 252, 2005. ISSN

0022-1694. doi: https://doi.org/10.1016/j.jhydrol.2005.01.005. URL http://www.sciencedirect.com/science/article/pii/S0022169405000065.

Niko Kampman, Mike Bickle, Max Wigley, and Benoit Dubacq. Fluid flow and co2–fluid–mineral interactions during co2-storage in sedimentary basins. *Chemical Geology*, 369:22 – 50, 2014. ISSN 0009-2541. doi: https://doi.org/10.1016/j.chemgeo.2013.11.012. URL http://www.sciencedirect.com/science/article/pii/S0009254113005500.

Stephen E. Kesler, Paul W. Gruber, Pablo A. Medina, Gregory A. Keoleian, Mark P. Everson, and Timothy J. Wallington. Global lithium resources: Relative importance of pegmatite, brine and other deposits. *Ore Geology Reviews*, 48:55 – 69, 2012. ISSN 0169-1368. doi: https://doi.org/10.1016/j.oregeorev.2012.05.006.

Christen Knudby and Jesús Carrera. On the use of apparent hydraulic diffusivity as an indicator of connectivity. *Journal of Hydrology*, 329(3): 377–389, 2006. ISSN 0022-1694. doi: https://doi.org/10.1016/j.jhydrol.2006.02.026. URL https://www.sciencedirect.com/science/article/pii/S0022169406001107.

Christen Knudby and Jesus Carrera. On the relationship between indicators of geostatistical, flow and transport connectivity. *Advances in Water Resources*, 28(4):405 – 421, 2005. ISSN 0309-1708. doi: https://doi.org/10.1016/j.advwatres.2004.09.001. URL http://www.sciencedirect.com/science/article/pii/S0309170804001599.

GP Kruseman and NA de Ridder. Analysis and Evaluation of Pumping Test Data. Second Etition. *International Institute for Land Reclamation and Improvement, Publication*, 47, 1990.

Eric M LaBolle and Graham E Fogg. Role of molecular diffusion in contaminant migration and recovery in an alluvial aquifer system. In *Dispersion in Heterogeneous Geological Formations*, pages 155–179. Springer, 2001. doi: 10.1007/978-94-017-1278-1_8.

Antonio C Lasaga. *Kinetic theory in the earth sciences*. Princeton university press, 1998. doi: https://doi.org/10.1515/9781400864874.

Wei Li, Herbert H. Einstein, and John T. Germaine. An experimental study of matrix dissolution and wormhole formation using gypsum core flood tests: 1. permeability evolution and wormhole geometry analysis. *Journal of Geophysical Research: Solid Earth*, 124(11):11055–11073, 2019. doi: https://doi.org/10.1029/2018JB017238. URL https://agupubs.onlinelibrary.wiley.com/doi/abs/10.1029/2018JB017238.

Wenjuan Liu and Datu B. Agusdinata. Interdependencies of lithium mining and communities sustainability in salar de atacama, chile. *Journal of Cleaner Production*, 260:120838, 2020. ISSN 0959-6526. doi: https://doi.org/10.1016/j.jclepro.2020.120838. URL http://www.sciencedirect.com/science/article/pii/S0959652620308854.

X. Liu, W. A. Illman, A. J. Craig, J. Zhu, and T.-C. J. Yeh. Laboratory sandbox validation of transient hydraulic tomography. *Water Resources Research*, 43(5), 2007. doi: 10.1029/2006WR005144. URL https://agupubs.onlinelibrary.wiley.com/doi/abs/10.1029/2006WR005144.

Lombard, J.M., Azaroual, M., Pironon, J., Broseta, D., Egermann, P., Munier, G., and Mouronval, G. Co2 injectivity in geological storages: an overview of program and results of the geocarbone-injectivity project. *Oil Gas Sci. Technol. - Rev.IFP*, 65(4):533–539, 2010. doi: 10.2516/ogst/2010013. URL https://doi.org/10.2516/ogst/2010013.

Tim K. Lowenstein, Matthew C. Hein, Andrew L. Bobst, Teresa E. Jordan, Teh-Lung Ku, and Shangde Luo. An Assessment of Stratigraphic Completeness in Climate-Sensitive Closed-Basin Lake Sediments: Salar de Atacama, Chile. *Journal of Sedimentary Research*, 73(1):91–104, 01 2003. ISSN 1527-1404. doi: 10.1306/061002730091. URL https://doi.org/10.1306/061002730091.

Andrew J. Luhmann, Xiang-Zhao Kong, Benjamin M. Tutolo, Nagasree Garapati, Brian C. Bagley, Martin O. Saar, and William E. Seyfried. Experimental dissolution of dolomite by co2-charged brine at 100°c and 150bar: Evolution of porosity, permeability, and reactive surface area. *Chemical Geology*, 380:145 – 160, 2014. ISSN 0009-2541. doi: https://doi.org/10.1016/j.chemgeo.2014.05.001. URL http://www.sciencedirect.com/science/article/pii/S0009254114002241.

Linda Luquot, Olivier Rodriguez, and Philippe Gouze. Experimental characterization of porosity structure and transport property changes in limestone undergoing different dissolution regimes. *Transport in Porous Media*, 101(3): 507–532, 2014. doi: https://doi.org/10.1007/s11242-013-0257-4.

Robert G Maliva. *Aquifer characterization techniques*. Springer, 2016.

M.A. Marazuela, E. Vázquez-Suñé, E. Custodio, T. Palma, A. García-Gil, and C. Ayora. 3d mapping, hydrodynamics and modelling of the freshwater-brine mixing zone in salt flats similar to the salar de atacama (chile). *Journal of Hydrology*, 561:223 – 235, 2018. ISSN 0022-1694. doi: https://doi.org/10.1016/j.jhydrol.2018.04.010. URL http://www.sciencedirect.com/science/article/pii/S002216941830252X.

M.A. Marazuela, E. Vázquez-Suñé, C. Ayora, A. García-Gil, and T. Palma. Hydrodynamics of salt flat basins: The salar de atacama example. *Science of The Total Environment*, 651:668 – 683, 2019. ISSN 0048-9697. doi: https://doi.org/10.1016/j.scitotenv.2018.09.190. URL http://www.sciencedirect.com/science/article/pii/S0048969718336350.

Lurdes Martinez-Landa and Jesús Carrera. An analysis of hydraulic conductivity scale effects in granite (full-scale engineered barrier experiment (febex), grimsel, switzerland). *Water Resources Research*, 41(3), 2005. doi: 10.1029/2004WR003458. URL https://agupubs.onlinelibrary.wiley.com/doi/abs/10.1029/2004WR003458.

Lurdes Martinez-Landa and Jesus Carrera. A methodology to interpret cross-hole tests in a granite block. *Journal of Hydrology*, 325(1):222 – 240, 2006. ISSN

0022-1694. doi: https://doi.org/10.1016/j.jhydrol.2005.10.017. URL http://www.sciencedirect.com/science/article/pii/S0022169405005445.

A Medina and J Carrera. Transin IV. Fortran code for solving the coupled flow and transport inverse problem. *User's guide ETSI Caminos Canales y Puertos, Barcelona*, 248, 2005.

Agustín Medina and Jesús Carrera. Geostatistical inversion of coupled problems: dealing with computational burden and different types of data. *Journal of Hydrology*, 281(4):251 – 264, 2003. ISSN 0022-1694. doi: https://doi.org/10.1016/S0022-1694(03)00190-2. URL http://www.sciencedirect.com/science/article/pii/S0022169403001902. Stochastic Inversion in Hydrogeology.

Peter M. Meier, Jesús Carrera, and Xavier Sánchez-Vila. An evaluation of jacob's method for the interpretation of pumping tests in heterogeneous formations. *Water Resources Research*, 34(5):1011–1025, 1998. doi: 10.1029/98WR00008.

Peter M. Meier, Agustin Medina, and Jesús Carrera. Geostatistical inversion of cross-hole pumping tests for identifying preferential flow channels within a shear zone. *Groundwater*, 39(1):10–17, 2001. doi: 10.1111/j.1745-6584.2001.tb00346.x. URL https://ngwa.onlinelibrary.wiley.com/doi/abs/10.1111/j.1745-6584.2001.tb00346.x.

Phoolendra Kumar Mishra, Velimir Vessilinov, and Hoshin Gupta. On simulation and analysis of variable-rate pumping tests. *Groundwater*, 51(3):469–473, 2013. doi: doi:10.1111/j.1745-6584.2012.00961.x.

Lee Ann Munk, David F. Boutt, Scott A. Hynek, and Brendan J. Moran. Hydrogeochemical fluxes and processes contributing to the formation of lithium-enriched brines in a hyper-arid continental basin. *Chemical Geology*, 493:37 – 57, 2018. ISSN 0009-2541. doi: https://doi.org/10.1016/j.chemgeo.2018.05.013. URL http://www.sciencedirect.com/science/article/pii/S000925411830233X.

Shlomo P. Neuman and Vittorio Di Federico. Multifaceted nature of hydrogeologic scaling and its interpretation. *Reviews of Geophysics*, 41(3), 2003. doi: 10.1029/2003RG000130. URL https://agupubs.onlinelibrary.wiley.com/doi/abs/10.1029/2003RG000130.

Christopher J Neville and Garth van der Kamp. Using recovery data to extend the effective duration of pumping tests. *Groundwater*, 50(5):804–807, 2012. doi: doi:10.1111/j.1745-6584.2011.00906.x.

C Ortiz, R Aravena, E Briones, F Suárez, C Tore, and JF Muñoz. Sources of surface water for the soncor ecosystem, salar de atacama basin, northern chile. *Hydrological Sciences Journal*, 59(2):336–350, 2014. doi: https://doi.org/10.1080/02626667.2013.829231.

Peter Ortoleva, Enrique Merino, Craig Moore, and John Chadam. Geochemical self-organization i; reaction-transport feedbacks and modeling approach. *American Journal of science*, 287(10):979–1007, 1987.

J. C. Parker and M. Th. van Genuchten. Flux-averaged and volume-averaged concentrations in continuum approaches to solute transport. *Water Resources Research*, 20(7):866–872, 1984. doi: https://doi.org/10.1029/WR020i007p00866. URL https://agupubs.onlinelibrary.wiley.com/doi/abs/10.1029/WR020i007p00866.

David L Parkhurst, CAJ Appelo, et al. User's guide to phreeqc (version 2): A computer program for speciation, batch-reaction, one-dimensional transport, and inverse geochemical calculations. *Water-resources investigations report*, 99(4259):312, 1999.

D. Pedretti, D. Fernàndez-Garcia, X. Sanchez-Vila, D. Bolster, and D. A. Benson. Apparent directional mass-transfer capacity coefficients in three-dimensional anisotropic heterogeneous aquifers under radial convergent transport. *Water Resources Research*, 50(2):1205–1224, 2014. doi: 10.1002/2013WR014578. URL https://agupubs.onlinelibrary.wiley.com/doi/abs/10.1002/2013WR014578.

Karine Petrus and Piotr Szymczak. Influence of layering on the formation and growth of solution pipes. *Frontiers in Physics*, 3:92, 2016. doi: https://doi.org/10.3389/fphy.2015.00092.

M. Pool, J. Carrera, A. Alcolea, and E.M. Bocanegra. A comparison of deterministic and stochastic approaches for regional scale inverse modeling on the mar del plata aquifer. *Journal of Hydrology*, 531:214 – 229, 2015. ISSN 0022-1694. doi: https://doi.org/10.1016/j.jhydrol.2015.09.064. URL http://www.sciencedirect.com/science/article/pii/S0022169415007477. Groundwater flow and transport in aquifers: Insights from modeling and characterization at the field scale.

Vincent EA Post and Jos R von Asmuth. Hydraulic head measurements—new technologies, classic pitfalls. *Hydrogeology Journal*, 21(4):737–750, 2013. doi: 10.1007/s10040-013-0969-0.

Juan Jose Pueyo, Guillermo Chong, and Carlos Ayora. Lithium saltworks of the salar de atacama: A model for mgso4-free ancient potash deposits. *Chemical Geology*, 466:173 – 186, 2017. ISSN 0009-2541. doi: https://doi.org/10.1016/j.chemgeo.2017.06.005. URL http://www.sciencedirect.com/science/article/pii/S0009254117303637.

Banda S. RamaRao, A. Marsh LaVenue, Ghislain De Marsily, and Melvin G. Marietta. Pilot point methodology for automated calibration of an ensemble of conditionally simulated transmissivity fields: 1. theory and computational experiments. *Water Resources Research*, 31(3):475–493, 1995. doi: 10.1029/94WR02258. URL https://agupubs.onlinelibrary.wiley.com/doi/abs/10.1029/94WR02258.

HJ Ramey Jr et al. Short-time well test data interpretation in the presence of skin effect and wellbore storage. *Journal of Petroleum Technology*, 22(01):97–104, 1970.

Gustavo Ramos, Jesus Carrera, Susana Gómez, Carlos Minutti, and Rodolfo Camacho. A stable computation of log-derivatives from noisy drawdown data. *Water Resources Research*, 53(9):7904–7916, 2017.

G. C. Rau, V. E. A. Post, M. Shanafield, T. Krekeler, E. W. Banks, and P. Blum. Error in hydraulic head and gradient time-series measurements: a quantitative appraisal. *Hydrology and Earth System Sciences*, 23 (9):3603–3629, 2019. doi: 10.5194/hess-23-3603-2019. URL https://www.hydrol-earth-syst-sci.net/23/3603/2019/.

Nicolas Remy, Alexandre Boucher, and Jianbing Wu. *Applied geostatistics with SGeMS: A user's guide*. Cambridge University Press, 2009.

F. Renard, J.-P. Gratier, P. Ortoleva, E. Brosse, and B. Bazin. Self-organization during reactive fluid flow in a porous medium. *Geophysical Research Letters*, 25(3):385–388, 1998. doi: https://doi.org/10.1029/97GL03781. URL https://agupubs.onlinelibrary.wiley.com/doi/abs/10.1029/97GL03781.

Philippe Renard. *Hydraulics of Wells and Well Testing*, chapter 151. Encyclopedia of Hydrological Sciences, 2006. ISBN 9780470848944. doi: 10.1002/0470848944.hsa154a. URL https://onlinelibrary.wiley.com/doi/abs/10.1002/0470848944.hsa154a.

Philippe Renard and Denis Allard. Connectivity metrics for subsurface flow and transport. *Advances in Water Resources*, 51:168 – 196, 2013. ISSN 0309-1708. doi: https://doi.org/10.1016/j.advwatres.2011.12.001. URL http://www.sciencedirect.com/science/article/pii/S0309170811002223. 35th Year Anniversary Issue.

Philippe Renard, Damian Glenz, and Miguel Mejias. Understanding diagnostic plots for well-test interpretation. *Hydrogeology Journal*, 17(3):589–600, 2009. doi: https://doi.org/10.1007/s10040-008-0392-0.

Charles W. Rovey II. Digital simulation of the scale effect in hydraulic conductivity. *Hydrogeology Journal*, 6(2):216–225, Aug 1998. ISSN 1435-0157. doi: 10.1007/s100400050146. URL https://doi.org/10.1007/s100400050146.

John R Rumble, David R Lide, and Thomas J Bruno. *CRC handbook of chemistry and physics*. 2018.

J. Salas, J. Guimerà, O. Cornellà, R. Aravena, E. Guzmàn, and C. Tore. Hidrogeología del sistema lagunar del margen este del salar de atacama (chile). *Boletin Geologico Y Minero*, 4(121):357–372, 2010.

Xavier Sánchez-Vila and JesÚs Carrera. Directional effects on convergent flow tracer tests. *Mathematical geology*, 29(4):551–569, 1997. doi: https://doi.org/10.1007/BF02775086.

Xavier Sanchez-Vila, Jesus Carrera, and Jorge P. Girardi. Scale effects in transmissivity. *Journal of Hydrology*, 183(1):1 – 22, 1996. ISSN 0022-1694. doi: https://doi.org/10.1016/S0022-1694(96)80031-X. URL `http://www.sciencedirect.com/science/article/pii/S002216949680031X`.

Dirk Schulze-Makuch, Douglas A. Carlson, Douglas S. Cherkauer, and Peter Malik. Scale dependency of hydraulic conductivity in heterogeneous media. *Groundwater*, 37(6):904–919, 1999. doi: 10.1111/j.1745-6584.1999.tb01190.x. URL `https://ngwa.onlinelibrary.wiley.com/doi/abs/10.1111/j.1745-6584.1999.tb01190.x`.

Alimatou Seck, Claire Welty, and Reed M. Maxwell. Spin-up behavior and effects of initial conditions for an integrated hydrologic model. *Water Resources Research*, 51(4):2188–2210, 2015. doi: 10.1002/2014WR016371. URL `https://agupubs.onlinelibrary.wiley.com/doi/abs/10.1002/2014WR016371`.

APS Selvadurai, Cyrille-B Couture, and SM Rezaei Niya. Permeability of wormholes created by co2-acidized water flow through stressed carbonate rocks. *Physics of Fluids*, 29(9):096604, 2017. doi: https://doi.org/10.1063/1.5002129.

SE Silliman and G Mantz. The effect of measurement error on estimating the hydraulic gradient in three dimensions. *Groundwater*, 38(1):114–120, 2000. doi: 10.1111/j.1745-6584.2000.tb00208.x.

Luit J. Slooten, Jesus Carrera, Eduardo Castro, and Daniel Fernandez-Garcia. A sensitivity analysis of tide-induced head fluctuations in coastal aquifers.

Journal of Hydrology, 393(3):370–380, 2010. ISSN 0022-1694. doi: https://doi.org/10.1016/j.jhydrol.2010.08.032. URL https://www.sciencedirect.com/science/article/pii/S0022169410005494.

Xavier Sánchez-Vila, Peter M. Meier, and Jesús Carrera. Pumping tests in heterogeneous aquifers: An analytical study of what can be obtained from their interpretation using jacob's method. *Water Resources Research*, 35(4): 943–952, 1999. doi: 10.1029/1999WR900007.

Carl I Steefel and Antonio C Lasaga. A coupled model for transport of multiple chemical species and kinetic precipitation/dissolution reactions with application to reactive flow in single phase hydrothermal systems. *American Journal of science*, 294(5):529–592, 1994.

Hans F. Stroo, Andrea Leeson, Jeffrey A. Marqusee, Paul C. Johnson, C. Herb Ward, Michael C. Kavanaugh, Tom C. Sale, Charles J. Newell, Kurt D. Pennell, Carmen A. Lebrón, and Marvin Unger. Chlorinated ethene source remediation: Lessons learned. *Environmental Science & Technology*, 46(12): 6438–6447, 2012. doi: 10.1021/es204714w. URL https://doi.org/10.1021/es204714w. PMID: 22558915.

Basudev Swain. Recovery and recycling of lithium: A review. *Separation and Purification Technology*, 172:388 – 403, 2017. ISSN 1383-5866. doi: https://doi.org/10.1016/j.seppur.2016.08.031. URL http://www.sciencedirect.com/science/article/pii/S1383586616305652.

H Randy Sweet, Gerritt Rosenthal, and Dorothy F Atwood. Water level monitoring-achievable accuracy and precision. *Ground water and vadose zone monitoring: Philadelphia, American Society for Testing and Materials, Special Technical Publication*, 1053:178–192, 1990.

P. Szymczak and A. J. C. Ladd. A network model of channel competition in fracture dissolution. *Geophysical Research Letters*, 33(5), 2006. doi: https://doi.org/10.1029/2005GL025334. URL https://agupubs.onlinelibrary.wiley.com/doi/abs/10.1029/2005GL025334.

P. Szymczak and A. J. C. Ladd. Wormhole formation in dissolving fractures. *Journal of Geophysical Research: Solid Earth*, 114(B6), 2009. doi: https://doi.org/10.1029/2008JB006122. URL https://agupubs.onlinelibrary.wiley.com/doi/abs/10.1029/2008JB006122.

Charles V Theis. The relation between the lowering of the piezometric surface and the rate and duration of discharge of a well using ground-water storage. *Eos, Transactions American Geophysical Union*, 16(2):519–524, 1935.

Michela Trabucchi, Jesús Carrera, and Daniel Fernàndez-Garcia. Generalizing Agarwal's Method for the interpretation of Recovery Tests Under Non-Ideal Conditions. *Water Resources Research*, 54(9):6393–6407, 2018. doi: 10.1029/2018WR022684. URL https://agupubs.onlinelibrary.wiley.com/doi/abs/10.1029/2018WR022684.

Michela Trabucchi, Daniel Fernàndez-Garcia, and Jesús Carrera. Automatic calibration of groundwater models with bias correction and data filtering: Working with drawdown data. *Water Resources Research*, n/a(n/a):e2020WR028097, 2021. doi: https://doi.org/10.1029/2020WR028097. URL https://agupubs.onlinelibrary.wiley.com/doi/abs/10.1029/2020WR028097. e2020WR028097 2020WR028097.

Paolo Trinchero, Xavier Sánchez-Vila, and Daniel Fernàndez-Garcia. Point-to-point connectivity, an abstract concept or a key issue for risk assessment studies? *Advances in Water Resources*, 31(12):1742 – 1753, 2008. ISSN 0309-1708. doi: https://doi.org/10.1016/j.advwatres.2008.09.001.

Virat K. Upadhyay, Piotr Szymczak, and Anthony J. C. Ladd. Initial conditions or emergence: What determines dissolution patterns in rough fractures? *Journal of Geophysical Research: Solid Earth*, 120(9):6102–6121, 2015. doi: https://doi.org/10.1002/2015JB012233. URL https://agupubs.onlinelibrary.wiley.com/doi/abs/10.1002/2015JB012233.

G. van der Kamp. Calculation of constant-rate drawdowns from stepped-rate pumping tests. *Groundwater*, 27(2):175–183, 1989. doi: 10.1111/j.1745-6584.

1989.tb00438.x. URL https://ngwa.onlinelibrary.wiley.com/doi/abs/10.1111/j.1745-6584.1989.tb00438.x.

Hanna Vikström, Simon Davidsson, and Mikael Höök. Lithium availability and future production outlooks. *Applied Energy*, 110:252 – 266, 2013. ISSN 0306-2619. doi: https://doi.org/10.1016/j.apenergy.2013.04.005. URL http://www.sciencedirect.com/science/article/pii/S0306261913002997.

Thomas von Schroeter, Florian Hollaender, Alain C Gringarten, et al. Analysis of well test data from permanent downhole gauges by deconvolution. pages 1–13, 2002.

N. Weisbrod, C. Alon-Mordish, E. Konen, and Y. Yechieli. Dynamic dissolution of halite rock during flow of diluted saline solutions. *Geophysical Research Letters*, 39(9), 2012. doi: https://doi.org/10.1029/2012GL051306. URL https://agupubs.onlinelibrary.wiley.com/doi/abs/10.1029/2012GL051306.

Xian-Huan Wen and J.Jaime Gómez-Hernández. Numerical modeling of macrodispersion in heterogeneous media: a comparison of multi-gaussian and non-multi-gaussian models. *Journal of Contaminant Hydrology*, 30(1):129 – 156, 1998. ISSN 0169-7722. doi: https://doi.org/10.1016/S0169-7722(97)00035-1.

Andrew W. Western, Günter Blöschl, and Rodger B. Grayson. Toward capturing hydrologically significant connectivity in spatial patterns. *Water Resources Research*, 37(1):83–97, 2001. doi: 10.1029/2000WR900241. URL https://agupubs.onlinelibrary.wiley.com/doi/abs/10.1029/2000WR900241.

M Willmann, Jesus Carrera, Xavier Sánchez-Vila, and E Vázquez-Suñé. On the meaning of the transmissivity values obtained from recovery tests. *Hydrogeology Journal*, 15(5):833–842, 2007. doi: https://doi.org/10.1007/s10040-006-0147-8.

M. Willmann, J. Carrera, and X. Sánchez-Vila. Transport upscaling in heterogeneous aquifers: What physical parameters control memory functions? *Water Resources Research*, 44(12), 2008. doi: 10.1029/2007WR006531. URL https://agupubs.onlinelibrary.wiley.com/doi/abs/10.1029/2007WR006531.

T.-C. Jim Yeh and Shuyun Liu. Hydraulic tomography: Development of a new aquifer test method. *Water Resources Research*, 36(8):2095–2105, 2000. doi: 10.1029/2000WR900114. URL https://agupubs.onlinelibrary.wiley.com/doi/abs/10.1029/2000WR900114.

Pengfei Zhang, Stephanie L DeVries, Annette Dathe, and Amvrossios C Bagtzoglou. Enhanced mixing and plume containment in porous media under time-dependent oscillatory flow. *Environmental science & technology*, 43(16):6283–6288, 2009. doi: doi:10.1021/es900854r.

Qiang Zhang, Yu Zhou, and Vijay P. Singh. Detrending methods for fluctuation analysis in hydrology: amendments and comparisons of methodologies. *Hydrological Processes*, 28(3):753–763, 2014. doi: 10.1002/hyp.9637. URL https://onlinelibrary.wiley.com/doi/abs/10.1002/hyp.9637.

Chunmiao Zheng and Steven M. Gorelick. Analysis of solute transport in flow fields influenced by preferential flowpaths at the decimeter scale. *Groundwater*, 41(2):142–155, 2003. doi: 10.1111/j.1745-6584.2003.tb02578.x.

Li Zheng, Jian-Qing Guo, and Yuping Lei. An improved straight-line fitting method for analyzing pumping test recovery data. *Groundwater*, 43(6):939–942, 2005. doi: 10.1111/j.1745-6584.2005.00094.x. URL https://ngwa.onlinelibrary.wiley.com/doi/abs/10.1111/j.1745-6584.2005.00094.x.

Brendan Zinn and Charles F. Harvey. When good statistical models of aquifer heterogeneity go bad: A comparison of flow, dispersion, and mass transfer in connected and multivariate gaussian hydraulic conductivity fields. *Water Resources Research*, 39(3), 2003. doi: 10.1029/2001WR001146.